NASA/CR-2007-215092

Health Monitoring of Thermal Protection Systems - Preliminary Measurements and Design Specifications

D. A. Scott and D. C. Price
CSIRO Materials Science and Engineering, Lindfield, NSW, Australia

December 2007

Since its founding, NASA has been dedicated to the advancement of aeronautics and space science. The NASA Scientific and Technical Information (STI) Program Office plays a key part in helping NASA maintain this important role.

The NASA STI Program Office is operated by Langley Research Center, the lead center for NASA's scientific and technical information. The NASA STI Program Office provides access to the NASA STI Database, the largest collection of aeronautical and space science STI in the world. The Program Office is also NASA's institutional mechanism for disseminating the results of its research and development activities. These results are published by NASA in the NASA STI Report Series, which includes the following report types:

- TECHNICAL PUBLICATION. Reports of completed research or a major significant phase of research that present the results of NASA programs and include extensive data or theoretical analysis. Includes compilations of significant scientific and technical data and information deemed to be of continuing reference value. NASA counterpart of peer-reviewed formal professional papers, but having less stringent limitations on manuscript length and extent of graphic presentations.

- TECHNICAL MEMORANDUM. Scientific and technical findings that are preliminary or of specialized interest, e.g., quick release reports, working papers, and bibliographies that contain minimal annotation. Does not contain extensive analysis.

- CONTRACTOR REPORT. Scientific and technical findings by NASA-sponsored contractors and grantees.

- CONFERENCE PUBLICATION. Collected papers from scientific and technical conferences, symposia, seminars, or other meetings sponsored or co-sponsored by NASA.

- SPECIAL PUBLICATION. Scientific, technical, or historical information from NASA programs, projects, and missions, often concerned with subjects having substantial public interest.

- TECHNICAL TRANSLATION. English-language translations of foreign scientific and technical material pertinent to NASA's mission.

Specialized services that complement the STI Program Office's diverse offerings include creating custom thesauri, building customized databases, organizing and publishing research results ... even providing videos.

For more information about the NASA STI Program Office, see the following:

- Access the NASA STI Program Home Page at *http://www.sti.nasa.gov*

- E-mail your question via the Internet to help@sti.nasa.gov

- Fax your question to the NASA STI Help Desk at (301) 621-0134

- Phone the NASA STI Help Desk at (301) 621-0390

- Write to:
  NASA STI Help Desk
  NASA Center for AeroSpace Information
  7115 Standard Drive
  Hanover, MD 21076-1320

NASA/CR-2007-215092

Health Monitoring of Thermal Protection Systems - Preliminary Measurements and Design Specifications

D. A. Scott and D. C. Price
CSIRO Materials Science and Engineering, Lindfield, NSW, Australia

December 2007

Work carried out by the following staff at CSIRO Materials Science and Engineering:

Adam Batten
Graeme Edwards
Don Price
Andrew Scott

Table of Contents

Executive Summary

The work reported here is the first stage of a project that aims to develop a health monitoring system for the Thermal Protection Systems (TPS) that enable a vehicle to safely re-enter the Earth's atmosphere. The TPS health monitoring system is to be integrated into an existing acoustic emissions-based Concept Demonstrator, developed by CSIRO, which has been previously demonstrated for evaluating impact damage of aerospace systems.

This requirement is for the development of a prototype health monitoring system that can be used in a variety of Thermal Protection Systems (TPS) applications. Included within this effort is the development of algorithms to interrogate sensor outputs and techniques to integrate optical fibre sensors to support TPS health monitoring. The requirement involves integrating sensor systems and developing sensor integration techniques to evaluate overall system performance through ground testing at both room and elevated temperatures. This effort will also result in a general methodology for use in developing TPS health monitoring systems.

The principal objective of the present phase of the work was to characterise materials and specify methods to a stage that would culminate in the design of a test-piece for use with the CSIRO/NASA structural health monitoring concept demonstrator (CD) in succeeding phases of the project. While a considerable proportion of this work has been carried out, the ultimate aim of designing a test-piece has not been achieved, largely because the material measurements raised serious concerns about the use of those materials in a demonstration structure. Resolution of these concerns requires discussion and consultation with NASA, and it is recommended that a CSIRO/NASA face-to-face meeting/workshop be convened at an early opportunity to resolve them.

Extensive measurements were made of the acoustic properties of two commercial ceramic foam materials, Cotronics 310 and Zircar Ceramics ZAL-45 foam, but neither was found to be particularly satisfactory for use as a 'model' demonstrator material. Measurements of acoustic velocities and attenuations were made in the frequency range 0.2 to 1.0 MHz, above which the attenuations were generally too high to make sensible measurements. The Cotronics material was found to be effectively isotropic, but strongly inhomogeneous due to the presence of large (up to tens of millimetres) voids, and hard, glassy inclusions. The Zircar foam did not contain such coarse inhomogeneities, but its elastic properties were highly anisotropic. Such anisotropy would severely complicate the use of impact-generated acoustic signals for location of the impact site.

Development of acoustic models of the materials and structures of interest was begun, based on guided wave calculations in infinite plates and on the modal resonance method. Further development of these models, particularly in the capability to model transient disturbances is required, and is under way. Development of a dynamic finite element model is planned to begin in the near future.

Thermal measurements were made using thermocouples, both on free ceramic tiles and on tiles bonded to an aluminium substrate. Not surprisingly, it was shown that

temperature measurements on the metallic substrate lost all spatial information carried by the heat flow through the ceramic. Information about the spatial extent of the damage can be obtained if the thermal sensors are well-insulated from the substrate, and some suggestions for doing this have been made.

A thermal sensor system based on optical frequency domain reflectivity measurements in a fibre Bragg grating (FBG) array, supplied by NASA Dryden FRC, was set up and demonstrated. It is now ready for incorporation into a test article. A novel scheme has been presented for integration of a FBG thermal sensing network into the CSIRO/NASA CD architecture. This requires further evaluation, but it has the potential to provide a robust and efficient fibre sensing network.

1. Introduction

1.1 Overall objectives

The work reported here is the first stage of a project that aims to develop a health monitoring system for the Thermal Protection Systems (TPS) that enable a vehicle to safely re-enter the Earth's atmosphere. NASA has a requirement to develop a TPS health monitoring hardware system, corresponding damage detection/classification algorithms for applications such as the Crew Exploration Vehicle, and to integrate the components into a cohesive ground test system in preparation for future flight applications.

As part of this requirement, the TPS health monitoring system is to be integrated into an existing acoustic emissions-based Concept Demonstrator, previously demonstrated for evaluating impact damage of aerospace systems. The integrated impact characterization and thermal protection health monitoring system will enable monitoring and evaluation of vehicle structure for fitness-for-service (i.e. fitness for atmospheric re-entry).

This requirement is for the development of a prototype health monitoring system that can be used in a variety of Thermal Protection Systems (TPS) applications. Included within this effort is the development of algorithms to interrogate sensor outputs and techniques to integrate optical fibre sensors to support TPS health monitoring. The requirement involves integrating sensor systems and developing sensor integration techniques to evaluate overall system performance through ground testing at both room and elevated temperatures. This effort will also result in a general methodology for use in developing TPS health monitoring systems. It will also be a catalyst for the development of a flight-qualified system with applications to NASA, DoD, and DARPA programs. This report is an extension of work reported in Abbott *et al.* (2001), Abbott *et al.* (2002), Abbott *et al.* (2003a), Abbott *et al.* (2003b), Batten *et al.* (2004), and Batten *et al.* (2006). A complete list of publications arising from this work is given in Appendix B.

1.2 System principles

The thermal protection systems with which we will be initially concerned consist of thick ceramic foam tiles attached to an aluminium plate substrate, though there are active investigations into new and improved TPS materials (NASA, 2007). The ceramic foam tiles have very low density (~ 0.15 g cm^{-3}) and very low thermal conductivity. They are generally bonded to the aluminium substrate, but may be mounted on stand-offs. The ceramic is brittle, and may be damaged by impact by micrometeroids, by debris in space, or accidentally during launch or subsequent operations.

The health monitoring system should detect and evaluate impacts on the ceramic tiles using passive acoustic emission techniques. Other techniques may subsequently be used to provide further evaluation of the damage, but there are no current plans for carrying out such further damage evaluation. Fitness-for-service will be determined by monitoring the thermal conductivity of the TPS in the vicinity of the damage. This will be achieved by external heating of the damaged region (currently by application of a heat lamp, but possibly eventually by the sun) and monitoring of the temperature distribution underneath or within the damaged region. This does not require heating to the temperatures experienced during re-entry, but only to temperatures that enable any

damage-induced anomalies in the thermal conductivity to be detected by the embedded thermal sensors.

The ultimate aim is to use a distributed optical fibre Bragg grating (FBG) sensing system for temperature measurement, but this is supplemented in the development stages of the work by thermocouples. NASA has provided a prototype FBG system for use in this work. It has been set up, tested and evaluated during this work, but was not used for any of the measurements reported here, all of which were made with thermocouples.

1.3 System architecture

The architecture of the TPS health monitoring system will be that of an autonomous multi-agent system, in which autonomous sensing 'agents', each of which control a small group of sensors in a local region of the structure, obtain local information about the integrity of the TPS, and collectively provide a diagnosis of any detected damaging events or damage. The architecture of the existing CSIRO/NASA structural health monitoring Concept Demonstrator (CD) has been described in earlier reports and papers (e.g. Abbott *et al.*, 2001, Abbott *et al.*, 2002, Abbott *et al.*, 2003a, Abbott *et al.*, 2003b, Batten *et al.*, 2004, Prosser *et al.*, 2004, Batten *et al.*, 2006, and Hoschke *et al.*, 2007; see Appendix B for a full listing). The advantage of the multi-agent system architecture is its robustness to damage or component failure: it has no central processor or controller, no single point of failure, and it is highly scalable.

A challenge of the present work was to develop an approach for integrating a distributed FBG sensor network into the multi-agent architecture. This has been achieved, and will be outlined later in this report.

1.4 Structure of the report

The TPS materials studied, and the experimental methods used for determining their acoustic properties, are described in the next Section. The two methods used for generating impacts (a pendulum and a pulsed laser beam) are also described. The extensive measurements of acoustic properties and their results are described in some detail in Section 3, followed by our preliminary work on acoustic modelling in Section 4. Section 5 outlines the experimental set-up for and results of thermal measurements carried out. This work was not aimed at characterising the thermal properties of the TPS materials, but at testing the heating method and examining qualitatively the detectability of simulated damage from the thermal measurements. This Section also describes the setting up and evaluation of the optical fibre measurement system provided by the NASA Dryden Flight Research Center. Section 6 outlines an arrangement by which an optical fibre thermal measurement network can be integrated into the multi-agent architecture of the CSIRO/NASA structural health monitoring concept demonstrator. While this arrangement has not yet been fully analysed or tested, it has the potential to provide a highly efficient and robust network. Finally, Section 7 discusses our conclusions relating to the design of a test-piece for use in subsequent phases of the project, in the form of questions that require resolution in consultation with NASA. Section 8 summarizes the results of this work.

2. Materials and methods

2.1. Introduction

The present investigations seek to develop a method for monitoring TPS panels that may be integrated with the multi-agent system architecture of the CSIRO/NASA Concept Demonstrator. In order to design a layout of piezoelectric sensors that is capable of detecting the elastic waves generated by an impact on the surface of an insulating material, we have made measurements of the ultrasonic properties of two insulating materials supplied to us by NASA Dryden Flight Research Center, and of the propagation characteristics of a 'tile' consisting of one of these insulating materials bonded to a sheet of aluminium. We have measured the density, the longitudinal and shear wave velocities, and the attenuation coefficients of these waves over the frequency range 0.2 to 5 MHz. Values of these properties are required to develop a numerical model of the acoustic properties of thermal protection tiles.

2.2 Previous work and materials used

There have been acoustics measurements made on TPS tile material since the Shuttle's inception. Some of the earliest published work was that of Thompson and Alers (1974), and Alers and Zimmerman (1980), who found the sound velocity to vary (by up to a factor of two) with propagation direction in the tiles, and that, even in one direction, velocities varied by ±5% over the area of one tile of areal dimensions $6'' \times 6''$. Velocities in the range 450 m/s to 1400 m/s, depending on the propagation direction, were measured. The density of this material was 0.15 g cm^{-3}. More recently Kuhr *et al.* (2006) reported similar velocities (620 m/s to 1410 m/s) in TPS foam.

Researchers at NASA Dryden have undertaken measurements and modelling of the thermal properties of a ceramic foam that has similar thermal properties to those of the TPS tiles used on the Space Shuttle. The material used in their and our initial experiments is Cotronics 310 ceramic foam. This material does not, however, possess the mechanical properties of tiles used on the Space Shuttle. The nature of this material, in particular the large size distribution of its porosity and hard inclusions, has proved to be somewhat of a hurdle in making reliable measurements of its ultrasonic properties.

The density of the Cotronics material was measured to be about 0.8 g cm^{-3}, and it contains pores of sizes varying from tens of microns to tens of millimetres (see Figure 2.1). There are also small volumes within the material that are not porous at all on this scale, but rather appear as solid spheres of glassy-like material, hard and difficult to cut through. These types of inhomogeneities proved troublesome in accurately determining the velocity and attenuation of ultrasound through the material.

A second ceramic material supplied by NASA Dryden was also investigated. This insulating material is an alumina-silica mixture (85% Al_2O_3, 15% SiO_2) with a nominal density of 0.72 g cm^{-3} made by Zircar Ceramics (Type ZAL-45). This material is uniform in appearance, chalky, and easy to machine. The ultrasonic velocity and attenuation in this material have been measured in three orthogonal directions; no thermal measurements have yet been made.
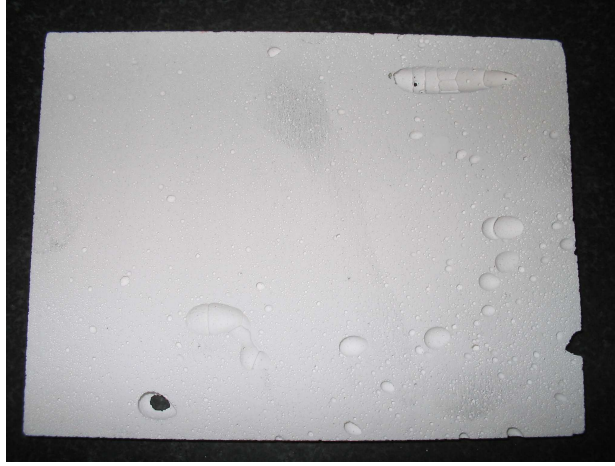
Figure 2.1. Photograph of sample of Cotronics material prepared for velocity and attenuation measurements, showing porosity. The sample is 154 mm × 115 mm × 5 mm.

2.3 Methods of measuring velocity

Several techniques for the measurement of ultrasonic velocity were considered and tried. The first method is based on the measurement of resonant frequencies of the sample. A sample of known thickness was carefully prepared and to it was attached a transducer operating in pulse-echo mode. The transducer drive frequency was swept to look for a sharp reduction in the received amplitude as the frequency sweeps though the standing wave resonance frequency of the sample. The condition for resonance is simply

$$n\lambda = 2d \quad \text{or} \quad f = n\frac{v}{2d},$$

where n is an integer, λ is the wavelength and f the frequency of the ultrasound, v is the velocity of sound in the material, and d is the thickness of the sample.

A second possible method is to vary the frequency and measure the small changes in phase of successive echoes from a sample of the material prepared as for the first method. Provided the frequency is changed in small steps (so that the phase changes between the echoes are much less than 2π), a phase-sensitive detector may be used to generate data that very accurately gives the time between the two echoes. This is a standard function on the RITEC (SNAP 5000) high-power generator and detector that was used for many of the measurements.

Unfortunately neither of these methods proved successful because of the high levels of scattering and attenuation in the material. The amplitude of the signal reflected from either a ceramic foam-to-air interface or a ceramic foam-to-aluminium interface was very low, and the attenuation of the ceramic foam is high.

The third method, which we used, was to measure the time of flight of an ultrasonic pulse through different, carefully prepared, thicknesses of ceramic foam. Longitudinal wave transducers in the frequency range 0.1 MHz to 5 MHz were tried on the foam, but high attenuation above 1 MHz and the difficulty of accurately measuring the time of arrival of pulses of frequency below 0.2 MHz limited the useful frequency range.

2.4 Sample preparation

In order to obtain an accurate measurement of velocity using this method, samples of accurate thickness needed to be prepared. While the Cotronics ceramic foam material supplied to us is easy to saw, it is weak in tension, so sawing the material required some care. The highly abrasive nature of the material blunted saw blades quickly, so the most feasible method of cutting was by manual hacksaw and a frequent change of blades. The hard pieces throughout the material made straight cutting difficult, and also introduced stress into the material sometimes resulting in breakage of the slice being taken. Generally speaking, samples of thickness down to about 10 mm could be cut, but these slices had faces that were neither parallel nor smooth, requiring further preparation as described below.

For the velocity measurements samples of larger thickness were prepared – four samples ranging in thickness from about 14 mm to 24 mm were prepared – ensuring a transit time though the material large enough to be measured with reasonable accuracy using ultrasonic pulses of centre frequency 1 MHz. As initial experiments on this ceramic foam showed the material to be fairly attenuative, samples of thickness considerably less than 14 mm were thought to be needed to give better signal-to-noise ratios. Seven samples ranging in thickness from 3 mm to 6 mm were also prepared. For all of these thicknesses the method described below was used to reduce the roughly cut slices to smooth, parallel-sided samples.

Samples were first sliced into rectangular prisms of dimensions about 150 mm × 115 mm × 10 mm, the thickness dimension being variable. These were then fitted into a purpose-made jig consisting of a plate of milled aluminium about 150 mm × 115 mm × 20 mm attached to the sides of which were two plates whose protrusion beyond the large face of the aluminium baseplate could be varied. Gauge blocks of the dimension corresponding to the desired thickness of ceramic foam were placed on a flat granite bed, the aluminium block placed on top of them, and the sides adjusted to touch the granite block. This set the sides of the jig parallel to the face of the aluminium block and accurately at the desired height (thickness) of the ceramic foam. This jig was removed from the granite plate, and the rough ceramic foam slice was the placed in the holder thus formed. Small strips of neoprene along the sidewalls were sometimes used to hold the ceramic foam in the jig. So held, the ceramic foam was then rubbed gently on a piece of emery paper laid over a glass plate. Once the first side was flat and smooth (the sample still of arbitrary thickness) the foam was flipped and then abraded slowly down to the desired thickness – one could clearly feel and hear when the sides of the jig started to rub on the emery paper, at which point the sample was the correct thickness. A light blow with dried, oil-free compressed air removed any dust left in the pores of the material. Photographs of some of the samples made in this way are shown in Figure 2.2.

The thicker samples used for velocity measurements were smaller in the areal dimensions, due to the availability at the time of only a small sample of the Cotronics material, but were prepared in a similar fashion to ensure an accurate thickness dimension.
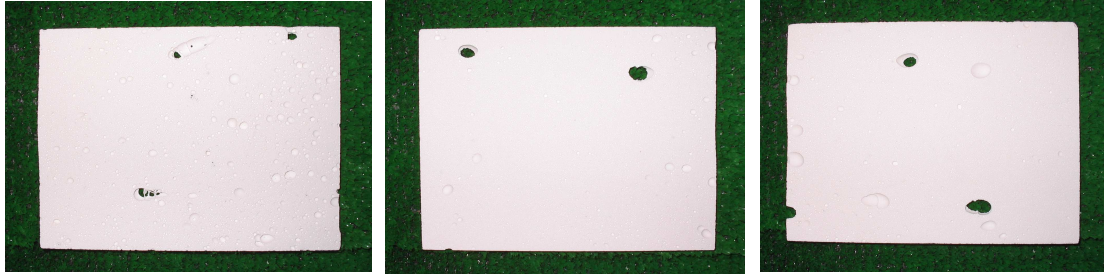
Figure 2.2. Samples prepared for attenuation and velocity measurements. All samples are approximately 150 mm × 115 mm.

2.5 Coupling ultrasound into ceramic foam

The use of standard ultrasonic couplants to improve transmission between the samples and the transducers was possible but certainly not desirable with this material. The Cotronics ceramic foam was too openly porous, so the couplant tended to soak into the foam, and therefore affect the velocity measurements: a contribution to the velocity would be made from the couplant-infused foam. A simple experiment of soaking the foam in coloured water for three hours showed the foam allowed water to penetrate 3 - 5 mm into the surface. In thin samples seeping of standard, coloured ultrasonic couplant into and across the surface was also clearly visible.

No couplant was used between the transducers and the sample. Initially samples were held between two transducers (see Figure 2.3), with considerable pressure applied using simple bar cramps. A small jig was made to hold the transducers parallel while squeezing the sample between their faces.

Measurements of shear wave velocities required the use of a buffer block (described below) that converted longitudinal waves into shear waves, so measurements of the longitudinal wave speed were also made with rectangular buffer blocks made of aluminium. Clamping the transducers, blocks, and ceramic foam sample together as above was not satisfactory as not enough pressure could be brought to bear on the interfaces to give a good signal-to-noise ratio. Consequently the ceramic foam was
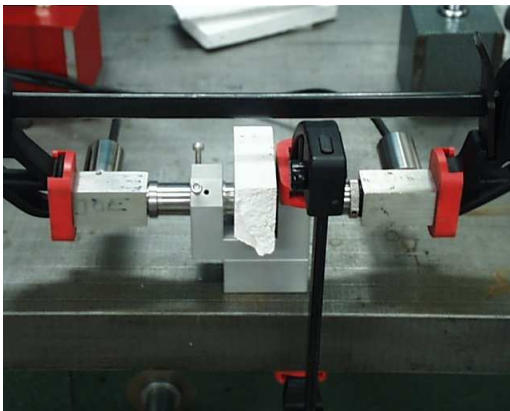

Figure 2.3. Ceramic foam sample squeezed between the parallel faces of two longitudinal wave transducers, for measurements of ultrasonic velocity.
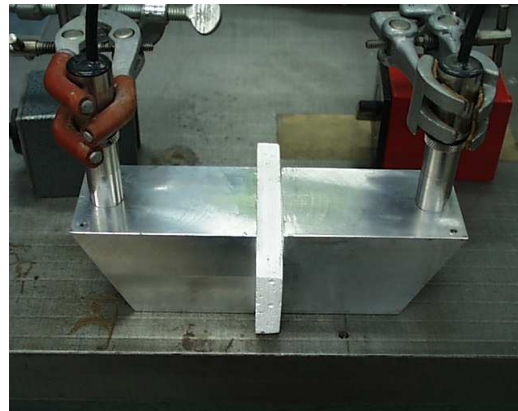

Figure 2.4. Shear-wave buffer blocks bonded to ceramic foam for velocity measurements.

bonded to the aluminium blocks using a cyano-acrylate adhesive (Loctite 401), shown in Figure 2.4. As this adhesive cures very quickly, absorption into the ceramic foam was minimal, and the bond layer was thin and hard. Subsequent removal of the foam from the block indicated the bondline was less than 0.5 mm thick, which would contribute little to the error in the measurement of velocity.

2.6 Buffer blocks

Two blocks of aluminium were cut from 50 mm × 50 mm square bar and the ends machined flat and parallel, to give an overall length of about 93 mm. These were used as buffer blocks in the measurement of longitudinal velocity of ultrasound in the ceramic foam.

As we did not at the beginning of these experiments have shear-wave transducers of the appropriate frequency for measuring the shear wave velocity in the range 0.2 to 2.0 MHz, it was necessary to use the longitudinal wave transducers to make such measurements. This was achieved by making two aluminium buffer blocks of the shape shown in Figure 2.5, which make use of the fact that when a longitudinal wave
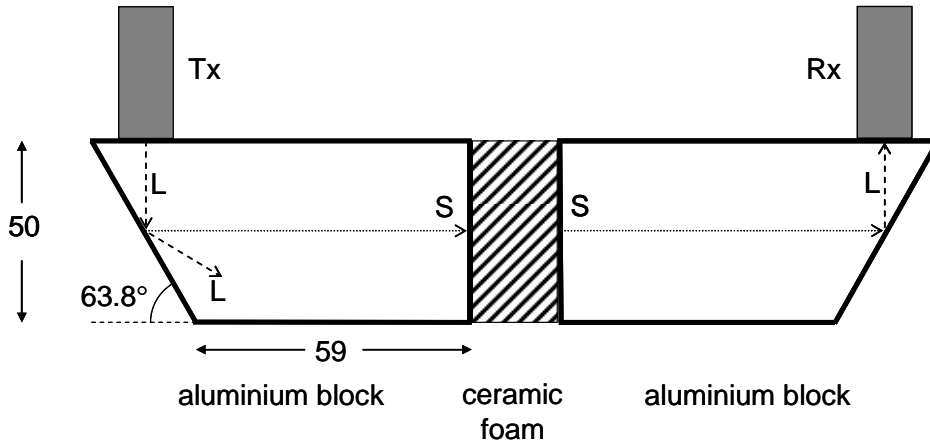
Figure 2.5. Set-up for measuring shear wave velocities using aluminium buffer blocks incorporating shear wave conversion. Tx: transmitting transducer. Rx: receiving transducer. L and S denote longitudinal and shear wave paths.

is incident on a plane reflecting surface the reflection consists of not only a longitudinal wave but also a reflected shear wave. If the angle of incidence of the longitudinal wave is α, and the angle of reflection of the shear wave is β then

$$\frac{\sin\alpha}{\lambda_L} = \frac{\sin\beta}{\lambda_S} \quad \text{or} \quad \frac{\sin\alpha}{\sin\beta} = \frac{\lambda_L}{\lambda_S} = \frac{v_L}{v_S},$$

where, in our case, λ_L and λ_S are the longitudinal and shear wavelengths of sound in aluminium at a particular frequency, and v_L and v_S are the longitudinal and shear velocities in aluminium respectively. The angle at which the aluminium block is cut is chosen so that $\alpha + \beta = 90°$ to ensure the reflected shear waves travel along the axis of the

13

block. The velocities v_L and v_S in these aluminium blocks were taken to be 6.34 mm/μs and 3.12 mm/μs, which gave $\alpha = 63.8°$. Standard calculations (see Arenberg, 1948, or Mason, 1958) show that the ratio of the reflected shear wave amplitude to that of the incident longitudinal wave amplitude under these conditions is about 0.93. One of the earliest examples of the exploitation of this phenomenon as a conversion mechanism for shear wave generation for measurements was by Papadakis and Bernstein (1963) and more recently by Jen et al. (2006).

The purchase of a pair of shear-wave transducers (Panametrics, type V153) with a centre frequency of 1 MHz were later used to verify the results obtained using the shear-wave conversion buffer blocks. They were used both in direct contact with the samples (no couplant), and also with the 'longitudinal wave', i.e. the rectangular prism, buffer blocks.

2.7 Measurement of attenuation

2.7.1 Introduction

As is the case in measuring velocity, there are a number of experimental techniques that are used to measure attenuation in materials. One possible technique would be to measure the through-thickness resonance alluded to in Section 2.3. By measuring the shape of the resonance curve as a function of the applied frequency, the quality factor of the curve, defined as

$$Q = \frac{\omega_0}{\omega_2 - \omega_1},$$

may be measured; ω_0 is the resonant frequency, and ω_2 and ω_1 are the two frequencies above and below (respectively) the resonance at which the average power has dropped to one half its value at resonance. Standard theory (see Levy, 2001) gives the energy attenuation coefficient α_E to be

$$\alpha_E = \frac{\omega_0}{Q\,v},$$

where v is the velocity of sound in the medium. While we attempted to measure such resonance curves no clear-cut resonances were found largely because of mode interference, and high scattering and absorption.

The attenuation coefficient may also be measured directly by observing the decay of oscillations in the medium after the removal of the driving force, or the decay of reverberating pulses in a parallel-sided sample. The latter technique has formed the basis of the most accurate determinations of absolute attenuation since the 1960s (see Papadakis, 1990), but great care needs to be taken with experimental set-up to properly account for impedance matching, electromechanical coupling, corrections for diffraction, and so on. Again, the absence of measurable reverberations in these foam samples precluded this technique.

The method used here was aimed at obtaining an approximate measure of the attenuation coefficient α as defined in the equation

$$A = A_0 e^{-\alpha x},$$

14

where A_0 is the initial amplitude of the wave, and A is the amplitude of the wave after it has travelled through a distance x of a medium whose attenuation coefficient is α. The units of α are Nepers per milliimetre (Np/mm) or decibels per millimetre (dB/mm). One Neper is defined as a change in amplitude by a factor of e^{-1}. Decibels are defined by the equation

$$dB = 10\log_{10}\left(\frac{I_0}{I}\right),$$

where I and I_0 are the intensities of the waves (proportional to the square of the amplitude) of amplitudes A and A_0 respectively. Simple algebra then gives the absorptive loss expressed in decibels to be 8.7 times the loss expressed in Nepers.

2.7.2 Present technique

We have tried to measure the amplitude of an ultrasonic wave as a function of distance travelled in ceramic foam by preparing a series of samples with parallel sides and of precise thickness (Figures 2.1 and 2.2 showed photographs of these samples), applying a fixed amplitude ultrasonic pulse to one side and measuring the amplitude of the pulse received on the other side. The primary difficulty is to apply the excitation in a repeatable way to one side of the different samples and to similarly repeatably measure the amplitude on the other side of the sample using contact transducers without couplant.

Initially we tried squeezing the samples, without buffer blocks, between the faces of two transducers. A tone-burst of excitation (80 cycles at 1 MHz) was applied to the transmitting transducer, and the amplitude of the received tone-burst, measured near the end of the tone-burst to simulate the amplitude of a continuous wave source, was measured. As with the velocity measurements, a bar cramp was used to apply pressure, and the pressure was increased until little or no change in the received amplitude could be discerned. This tone-burst technique did not, however, yield consistent results. We presume this is because the received amplitude (measured about 10 μs into the tone-burst) consists of contributions from many reverberations and modes in the sample.

A series of experiments was then undertaken to determine the optimal number of cycles in the exciting tone-burst, whether or not such a burst should be Hanning-modulated, and where in the received burst should the amplitude be measured. The most repeatable measure of the received amplitude was found by measuring the peak-to-peak voltage of the first significant part of the signal, as shown in Figure 2.6. This measure of the waveform remained independent of the number of cycles in the excitation tone-burst provided there were three or more cycles: the difference in this amplitude between using a one-cycle tone-burst and a two-cycle tone burst was small, typically less than 10%, and between using two and three cycles, less than a couple of percent, and between three and larger numbers there was no discernable difference. The waveform later than this oscillation showed marked changes for different numbers of cycles. A Hanning-windowed excitation pulse tended to smooth out the received waveform, making it more difficult to distinguish the arrival of the wave, and so was not used. This method was used in all experiments. The use of transducers near their centre frequencies was necessary to ensure that the 'frequency' of the half-cycle measured was at the desired frequency. If transducers are used far from their centre frequency the transient cycles near the beginning of pulses or tone-bursts may be at a slightly different frequency to that of the drive voltage.
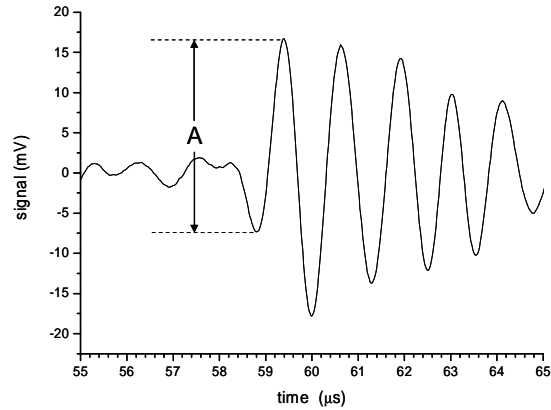
Figure 2.6. Measurement of amplitude of received waveform.

The other significant problem to address was coupling the transducers to the samples. Liquid couplant was ruled out because it seeped into the foam, changing its properties. Dry elastomeric couplants were tested but proved to have too high an attenuation, and showed marked changes in coupling with applied pressure. We opted for no couplant, and constructed a rig that could apply even and repeatable pressure across a sample.

2.7.3 Rig for attenuation measurements

The rig used for these measurements had two thick aluminium plates mounted between four rods; one plate was levelled and fixed in position, the other was mounted on four bearings which allowed it to be any distance from the fixed plate, but parallel to it. Onto each of these plates various jigs were affixed to hold the transducers and buffer blocks. Figure 2.7 shows a photograph of the rig. Care was
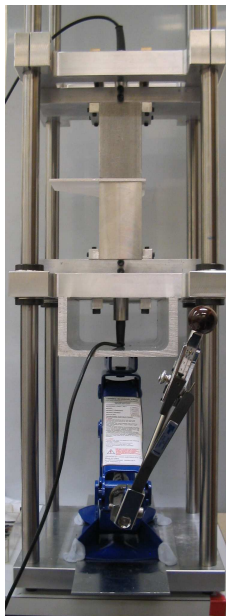
Figure 2.7. Photograph of experimental rig used to measure attenuation. A sample of 3-mm ceramic foam is held between the end faces of two longitudinal-wave buffer blocks, and pressure is applied to the blocks and sample by a screw jack, tightened using a torque-wrench.

16

taken mounting and aligning the buffer blocks to ensure they were parallel and that any forces applied had no components off the long axis of the blocks. The transducers were pressed against the buffer blocks using high-viscosity couplant and held in position with grub screws. Axial pressure was applied to the blocks using a screw jack onto which a torque wrench was attached. Pressure was increased until the torque wrench reached its predetermined setting. This setting was found from trials which monitored the received signal, watching at what pressure (torque) little further change in the received signals could be measured. This torque setting was used for all subsequent experiments. Figure 2.8 shows a close-up of the buffer blocks and samples being tested using longitudinal and shear wave configurations.

As was the case in the velocity measurements, our preliminary work did not use this rig or buffer blocks − estimates of the longitudinal wave attenuation were first made by squeezing transducers directly onto the surfaces of the prepared samples (see Figure 2.3) using bar cramps, and each time applying enough pressure to see that the received signal amplitude was not changing with further application of pressure. The experimental set-up of the RITEC was as outlined earlier. The transducers used were
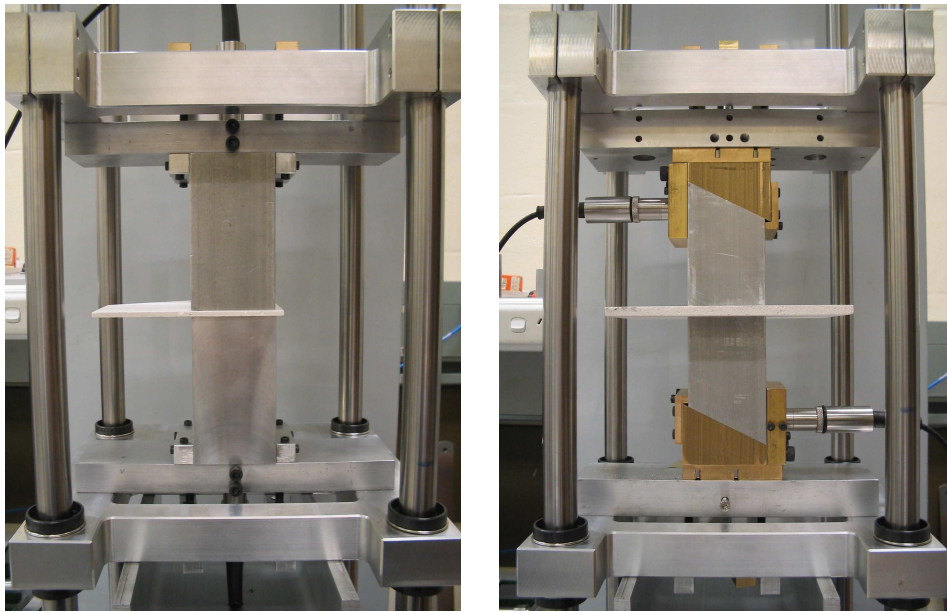
Figure 2.8. Close-ups of rig showing the set-up for longitudinal wave attenuation measurements (left), and shear wave attenuation measurements (right).

all highly-damped, immersible, with stainless steel cases, and selected to operate near their central frequency. They were (a) 1 MHz, 2.25 MHz, and 5.00 MHz, 0.5″-diameter transducers from Krautkramer, (b) 0.5 MHz, 1.0″-diameter transducers from Panametrics, and (c) 0.2 MHz and 0.1 MHz, 1.0″-diameter transducers from Ultran.

It was realised that the techniques used here will only give an estimate of the attenuation in these ceramic foam samples. By making relative measures of the signals from different thicknesses of foam we avoid the need for careful analysis of impedances,

diffraction and so forth, but for the purposes of providing experimentally measured data as a starting point for input into a model of acoustic propagation in these types of materials, it was seen as adequate.

A few experiments were carried out using the buffer blocks to estimate the attenuation in a material with similar magnitude of acoustic impedance as the ceramic foam, polyvinyl chloride (PVC) and polymethyl methacrylate (PMMA or Perspex or Plexiglass) whose attenuation coefficients have been measured by others. Our measurements were consistent with the work of others, although direct comparison is difficult. The attenuation coefficients for plastics vary widely depending on the method of manufacture and the particular type of PVC or Plexiglass. Cheeke (2002) quotes values of 6.4 to 12.4 dB/cm for PMMA at 5 MHz, and Pouet and Rasolofosaon (1993) give a value of just under 5 dB/cm at 5 MHz. Similarly for PVC figures range from 8 to just over 11 dB/cm from these two sources. Our measurements of PMMA and PVC attenuation were between 0.5 and 1.3 times those of Pouet and Rasolofosaon, but were complicated by relaxation effects. (When these plastics were squeezed the signal was observed to rise approximately exponentially with a 'half-life' of the order of five minutes increasing by about 50% over 20 minutes, which we presume was due to plastic flow of the sample slowly increasing the contact area and hence signal received. Such relaxation in the ceramic foam was also observed, but it was much less and could be ignored. In all cases measurements on the foam were taken immediately after applying pressure.)

2.8 Elastic wave propagation in TPS-like tiles

2.8.1 Fabrication of TPS-like tile

Researchers at NASA Dryden FRC prepared a sample 'tile' consisting of 3.175-mm (1/8″) thick, 230 mm × 155 mm (9″ × 6″) aluminium sheet to which was bonded a piece of Cotronics ceramic foam, 100 mm ×100 mm × 27 mm, (about 4″ × 4″ × 1″). The bonding layer was an RTV adhesive applied to a thickness of 0.008″ (200 μm). To this sheet we bonded (using both conductive epoxy adhesive and Loctite 401 cyano-acrylate adhesive) eight piezoelectric transducers in various locations in order to determine the signals produced by these transducers at different places on the 'back' side of the sheet as a result of impacts on the ceramic foam surface ('front' side). The layout of these transducers is reproduced approximately to scale in Figure 2.9. Two different sizes of PVDF transducers were used, both 52 μm thick, one 10 mm in diameter, the other 2.5 mm in diamter. Three different sizes of PZT transducer were tested, 2.5 mm (dia.) and 0.5 mm thick, 5.0 mm (dia.) and 0.5 mm thick, and 5.0 mm (dia.) and 2.0 mm thick. All transducers were uniformly poled. In the experiments described below only the transducers bonded to the aluminium sheet behind the ceramic foam were used: neither of the two outlying transducers were used.

2.8.2 Impact generation: experimental set-ups

The TPS tiles were subjected to two types of impact, a low-velocity impact using a simple pendulum, and a simulated high-velocity impact using a high-power pulse from a laser (see our previous report, Abbott *et al.*, 2003a). The experimental arrangements for these two are shown in Figure 2.10. In both cases the TPS tile is mounted in a frame upon an x-y table to allow accurate movement of the sample with respect to the impactor. Also mounted on the table is a small brass holder, with spring-loaded pins that made

Aluminium sheet, 3.175 mm thick

PVDF, 2.5 mm o.d., 0.05 mm thick

PVDF, 10 mm o.d., 0.05 mm thick

PVDF, 2.5 mm o.d., 0.05 mm thick

PZT, 2.5 mm o.d., 0.5 mm thick

PVDF, 2.5 mm o.d., 0.05 mm thick

PZT, 2.5 mm o.d., 0.5 mm thick

PZT, 5 mm o.d., 0.5 mm thick

PZT, 5 mm o.d., 2 mm thick

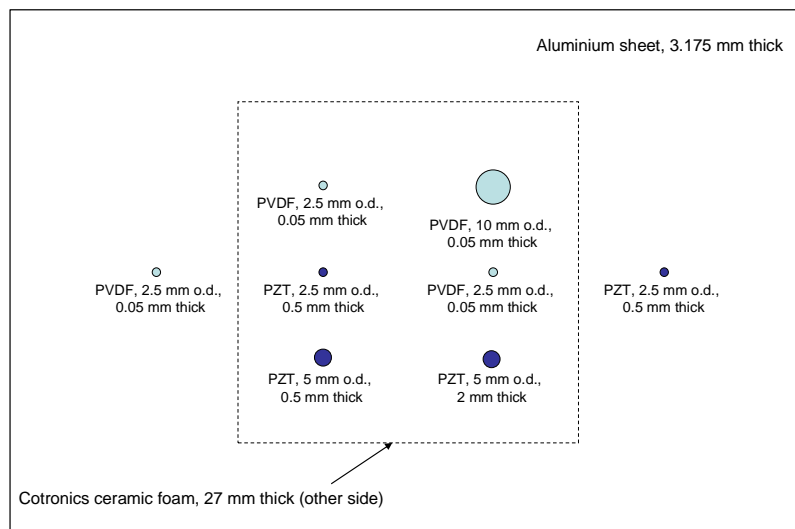Cotronics ceramic foam, 27 mm thick (other side)

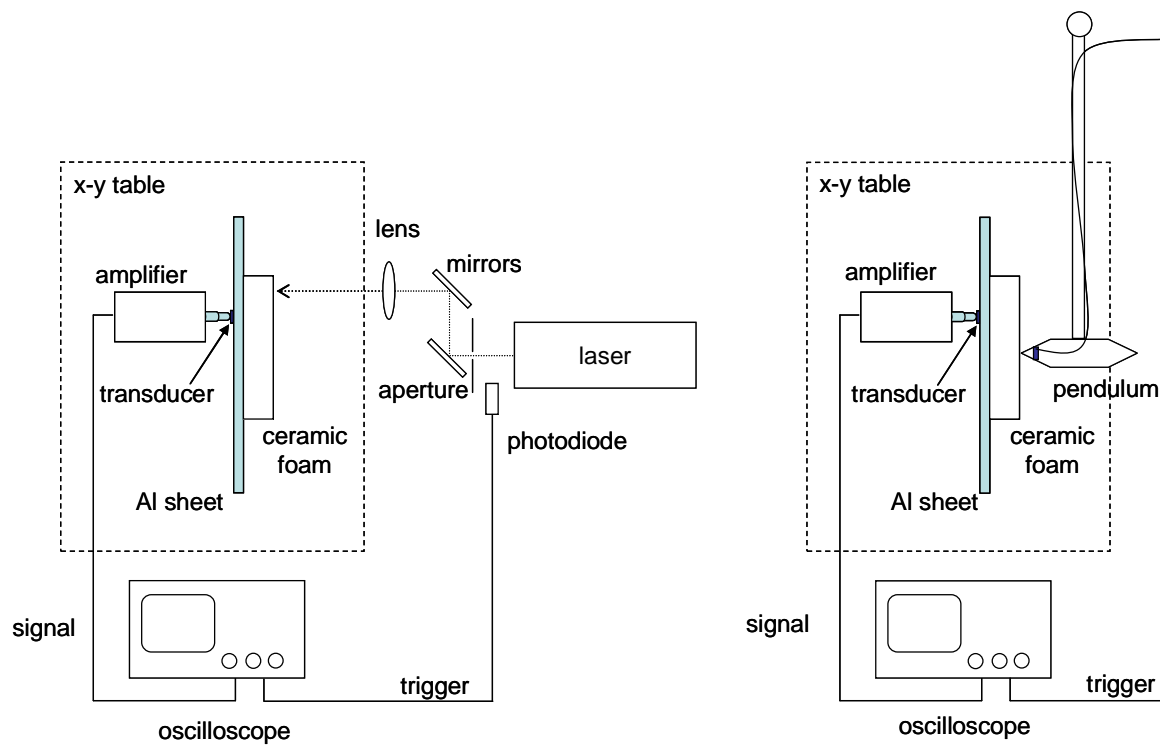Figure 2.9. Layout of TPS-like panel with different transducers bonded to the aluminium sheet.

Figure 2.10. Left: set-up for measuring elastic waves as a result of 'impacts' on the ceramic foam by a focused laser beam. Right: set-up for measuring elastic waves as a result of impacts on the ceramic foam by a pendulum.

contact with the back of the transducer whose output was to be monitored, and which contained a small voltage amplifier of gain about 6. The output of this amplifier was monitored by an oscilloscope sampling at 50 Msamples/s.

In one case (see Figure 2.10 (left)) the output of a pulsed Nd:YAG laser, about 250 mJ with a full width at half maximum of 6.3 ns, was focused onto the surface of the ceramic to a spot of diameter about 1.0 mm. The stray light from an aperture was detected by a fast photodiode, the signal from which was used to trigger the oscilloscope. This gave an accurate time of impact.

For the low-velocity impacts (see Figure 2.10 (right)) a pendulum was drawn back to a repeatable height and released, thereby ensuring a repeatable impact energy. The velocity of the head of the pendulum was measured by simply allowing the shaft near the head of the pendulum to pass through a laser beam, and the time the beam was obscured was measured. The velocity at impact was 0.7 m/s. (In one case this speed of impact caused overloading of one of the transducers bonded to the aluminium. For measurements using this transducer the speed of the pendulum at impact was reduced to 0.31 m/s.) The resultant energy of impact was calculated to be 41 mJ (8 mJ in the case of the lower velocity).

Into the impactor of the pendulum was incorporated a small (0.5 mm thick, 2.5 mm dia.) PZT transducer – in fact the transducer, protected by a dome of indium solder, formed the impacting tip. The output of this transducer was used to trigger the oscilloscope. Due to the relatively slow impact speed, while this trigger worked well, small differences between each impact meant that this trigger was not accurate to the sub-microsecond level required for accurate measurement of elastic pulse propagation speeds. (These differences may be caused by the deformation of the ceramic foam by successive impacts which may in turn affect the amplitude and frequency of the waves impinging on the transducer, and hence its output.) Nevertheless it provided triggering to an accuracy of a few microseconds, adequate for studying the waveforms generated by the various transducers monitoring the panel's vibration.

3. Acoustic properties of thermally insulating materials

3.1 Velocity measurements – Cotronics ceramic foam

A RITEC (SNAP 5000) instrument was used to generate a high-power drive signal for the transmitting transducer Tx, and to detect the signal from the receiving transducer Rx. The basic set-up is shown in Figure 3.1. This set-up was used to measure the longitudinal velocity in the ceramic foam either with or without the buffer blocks, and was also used for the measurement of shear wave velocities using the shear-wave conversion buffer blocks.

To measure the longitudinal velocity at different frequencies, the RITEC was set to generate a single cycle at 0.5 MHz, 1.0 MHz or 2.0 MHz. For each sample the through-transmission signal at each of these frequencies was recorded and used
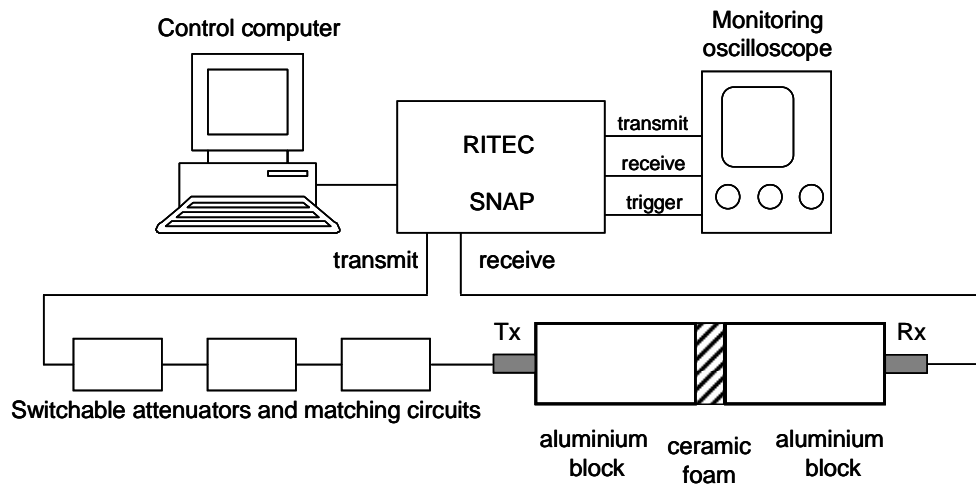
Figure 3.1. Experimental set-up for measuring longitudinal velocities in ceramic foam using buffer blocks and the RITEC system for transmission and reception of signals.

to determine the transit time through the two buffer blocks and the ceramic foam sample. Then pulse-echo signals were recorded using Tx and Rx, and these were used to measure the transit time through each of the aluminium buffer blocks. These blocks were not exactly the same length and so the transit times in each had to be measured individually. Typical signals measured using this technique are shown in Figure 3.2.

Some care needs to be taken when making measurements of transmission and echo times, as the transit times of ultrasound through these thicknesses of ceramic foam are generally less than 10 μs and there are systematic errors than need to be recognised. There is a delay between the trigger pulse of the RITEC signal generator and the time at which the voltage pulse appears at the output socket. There will also be a delay between the application of the voltage and the response of the transducer face. These delays may be slightly different depending on the frequency of the applied voltage and the response of a given transducer to that drive voltage at that particular

Figure 3.2. Received signals from (a) through transmission, (b) pulse echo in the 'transmitting' buffer block, and (c) pulse echo in the 'receiving' buffer block, using longitudinal waves, with a central excitation frequency of 1 MHz.

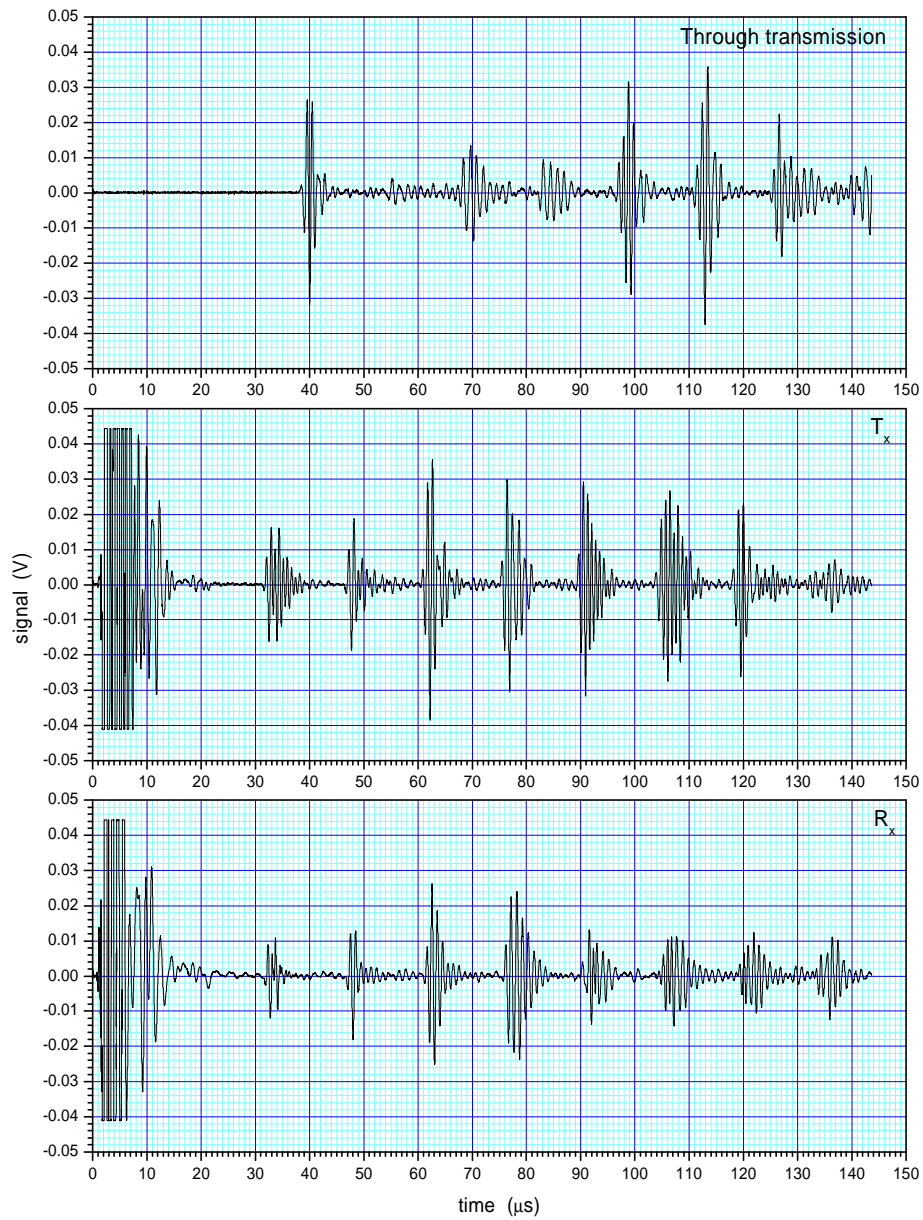frequency. While these can be measured and account taken, the method employed here, to a large extent, negates the effects of such delays. If t_1 is the time at which the pulse transmitted through both buffer blocks and the ceramic sample arrives, t_2 is the time at which the first echo signal in the transmitting buffer block arrives, and t_3 is the time at which the first echo signal in the receiving buffer block arrives, and they are all subject to a delay Δt, then

$$t_1 = t_1' + \Delta t$$
$$t_2 = t_2' + \Delta t$$
$$t_3 = t_3' + \Delta t$$

where the superscript denotes the true time, without the delay. The true transit time through the ceramic foam, t_c, is given by

$$t_c = t_1' - \frac{1}{2}\left(t_2' + t_3'\right)$$
$$= \left(t_1' + \Delta t\right) - \frac{1}{2}\left(\left(t_2' + \Delta t\right) + \left(t_2' + \Delta t\right)\right)$$
$$= t_1 - \frac{1}{2}\left(t_2 + t_3\right).$$

The thickness d of each sample of Cotronics ceramic foam was measured prior to gluing between the buffer blocks. The speed of sound in the ceramic foam, v_c, was therefore

$$v_c = \frac{d}{t_c}.$$

Another possibility to measure the transit time through each buffer block would be to measure the time between successive echoes in each block. However, inspection of the pulse echo signal soon reveals that the second echo is superposed on another signal (and subsequent echoes are similarly difficult to distinguish). These other echoes arise from longitudinal waves reflected off the sides of the buffer block, and the transmission of shear waves through the block that occur from the effects of diffraction from the transducer face and mode conversion on reflection from the walls. The most accurately determined time of arrival is that of the fastest and therefore first pulse. (It must also be remembered that the pulse echo signals are π out of phase with the through-transmission signals.)

A certain amount of care must be taken in the case of the shear wave signals. Figure 3.3 shows the shear wave signals from the through transmission, and the pulse echoes from each block at 1 MHz. In some cases one can see signals that arrive before the expected first shear wave arrival. These signals probably arise from longitudinal waves (that have almost twice the speed of shear waves) that remain unconverted to shear waves and have taken different paths through the buffer block. The shear wave arrival time, though, is fairly clear.

It should be remembered that these were 'destructive' tests in the sense that the ceramic foam samples were bonded to the ends of the aluminium blocks for each test and needed to be broken off for subsequent use of the blocks. (Sometimes the blocks remained unaffected, with solvent being able to remove any remnants of adhesive and/or ceramic foam, but occasionally they needed a light skimming on a mill to clear
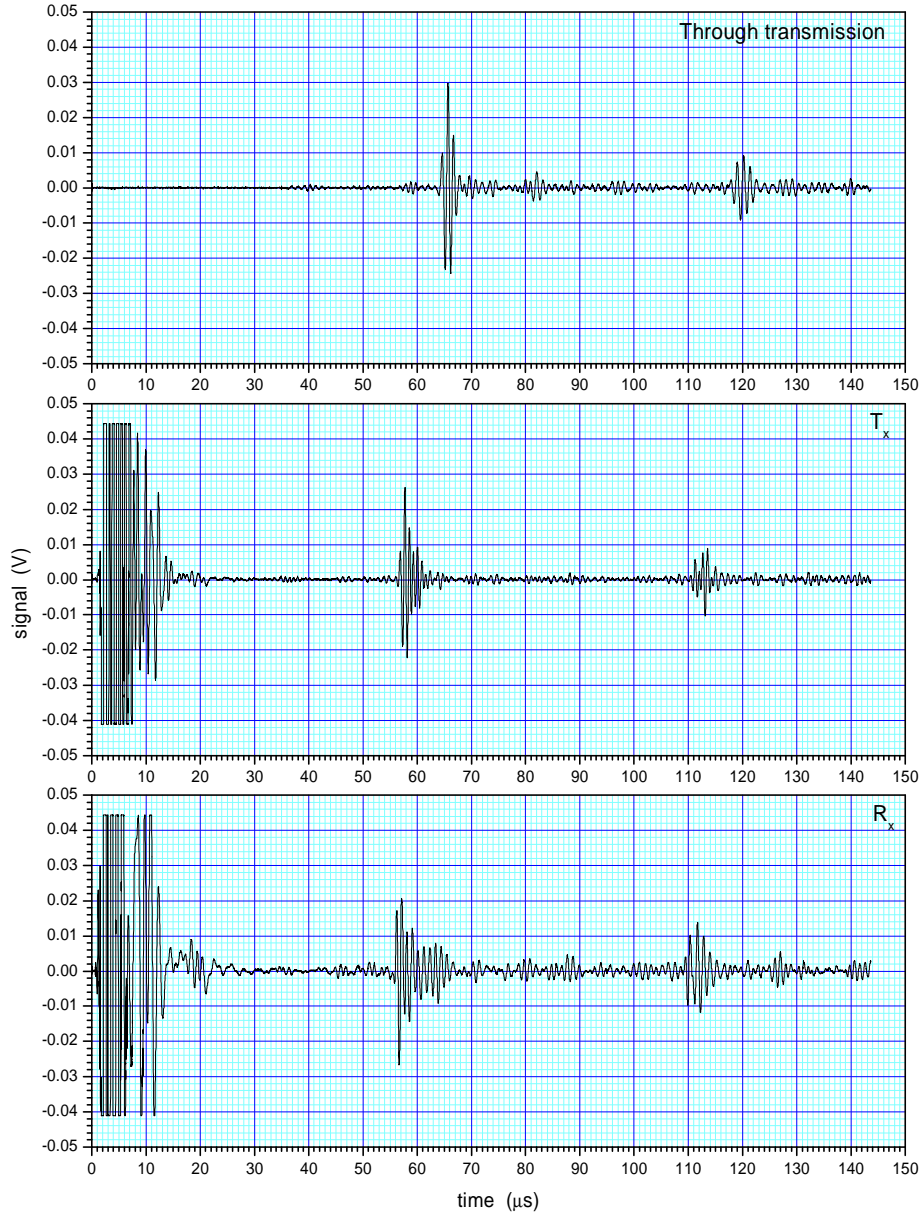
Figure 3.3. Received signals from (a) through transmission, (b) pulse echo in the 'transmitting' buffer conversion block, and (c) pulse echo in the 'receiving' buffer conversion block, using shear waves, with a central excitation frequency of 1 MHz.

the surface completely. The absolute length of the buffer blocks was immaterial, as the pulse echo times were always taken anew with each sample set-up.) This meant that longitudinal and shear wave measurements could not be taken on the same sample.

Table 1 shows the results of the measurements taken on samples that were cut in three orthogonal directions (arbitrarily labelled x, y, and z) from the original single piece of Cotronics foam available at the time. The uncertainty in each of the measurements is ±0.05 mm/µs. No dependence on frequency (from 0.5 MHz to 2.0 MHz) was found. The measurements of shear wave velocity in the nominal z-direction were also verified by use of the shear-wave transducers. These too yielded a value of shear wave velocity of 1.79 m s^{-1}.

Velocity in mm/µs	Direction through ceramic foam		
	x	y	z
Longitudinal wave	3.12	2.91	2.89
Shear wave	1.82	1.75	1.79

Table 1. Velocities measured in ceramic foam in three orthogonal directions.

From this data it would be tempting to suggest that there may be some anisotropy in the foam for longitudinal wave propagation. Apart from the fact that the shear wave results show no significant anisotropy, it was later found that there are large voids and glassy inclusions in the samples which have properties distinctly different from that of the foam in general. These flaws were not apparent in the thick samples used in these measurements, and only came to light when thin samples (3 - 6 mm) were prepared for attenuation measurements. Subsequent measurements indicated that the measurement of 3.12 mm/µs was anomalously high (probably due to the presence of a glassy inclusion), and so we concluded that this ceramic foam shows no anisotropy and that the longitudinal wave velocity is 2.90±0.05 mm/µs, and the shear wave velocity is 1.80±0.05 mm/µs.

3.2 Further measurements

Measurements were also made using a Panametrics Ultrasonic Analyzer (5052UA) as the transmitter/receiver, which delivered a single broadband voltage spike to the transmitter. Measurements were made on the 'z-direction' sample using shear waves. The times of arrival of the signals, obviously significantly filtered by the transducers, were measured and analysed in the same way as done when the RITEC was used, and the calculated velocity (1.82±0.05 mm/µs) was in agreement with that obtained using the RITEC on the same sample (1.79±0.05 mm/µs).

It was mentioned in Section 2.5 that we made some preliminary measurements of transit times in ceramic foam without the use of buffer blocks. The use of buffer blocks in the measurement of longitudinal wave velocities was not only to duplicate as nearly as possible the conditions under which each of the velocities were measured (given that buffer blocks were necessary to generate shear waves), but also because some odd results were found when buffer blocks were not used in measuring longitudinal wave velocities. At 1 MHz (measurements at lower frequencies were fraught with difficulties in separating received from transmitted pulses), the apparent

Thickness of ceramic foam (mm)	Apparent longitudinal velocity (mm/µs)
3	2.05
6	2.39
12	2.70
18	2.78
24	2.74

Table 2. Apparent longitudinal wave velocities in ceramic foam, measured without buffer blocks.

Thickness of ceramic foam (mm)	Apparent longitudinal velocity (mm/µs)
3	2.34
6	2.53
12	2.40
> 12	Low S/N

Table 3. Apparent longitudinal wave velocities in ceramic foam, measured with a short aluminium buffer block.

longitudinal velocities measured are shown in Table 2. The use of a short aluminium buffer block, 63 mm long, gave the results shown in Table 3.

It is concluded that there may be two sources of error in these measurements. Firstly, there is the obvious difficulty of precisely determining the time of arrival of a pulse that is close in time to the excitation pulse, the measurement of which is affected by the ringing of the transmitting transducer. The second source may have something to do with making measurements of velocity in the near field of the transducers. The near field to far field transition point for an ultrasonic transducer of radius a, operating at frequency f into a medium in which the speed of sound is v is approximately given by fa^2/v, which, for ceramic foam is about 14 mm, and for aluminium is about 5.5 mm at 1 MHz. This latter reason may explain why the velocities shown in Table 2 for foam thicknesses above 12 mm are fairly consistent, but it cannot fully explain the results in Table 3, which may be just a signal-to-noise problem, the arrival of competing signals, the presence of inhomogeneities in the samples, and so on. Further discussion of this appears in Section 3.4.2.

The use of large buffer blocks did not present such problems, and provided consistent results.

3.3 Attenuation results – Cotronics ceramic foam

3.3.1 Measurements without buffer blocks

In the first set of measurements of longitudinal wave attenuation no buffer blocks were used, using the set-up appearing in Figure 2.3, and the measurement system in Figure 3.1. At a number of frequencies between 0.1 MHz and 2.0 MHz the amplitudes of the received waves were measured in three different positions (giving an average amplitude A) using samples of thicknesses ranging from 3 mm to 20 mm. A linear least squares fit was made to the data plotted as ln(A) vs thickness, the absolute value of the slope of which gave the attenuation coefficient in Nepers/mm. This data is plotted in Figure 3.4, with estimated error bars generated from the error in the line slope as given by the fitting routine (approximately 25%). The real uncertainty is probably greater at lower frequencies as ringing of the transmitting transducer obfuscates the first arrival waveform at low frequencies and in thin samples.

Measurements were made at applied frequencies up to 3.5 MHz, but all the attenuation figures for 2 MHz to 3.5 MHz were the same. It was clear from the signals as a function of time that only frequencies below about 1.2 MHz were being transmitted through
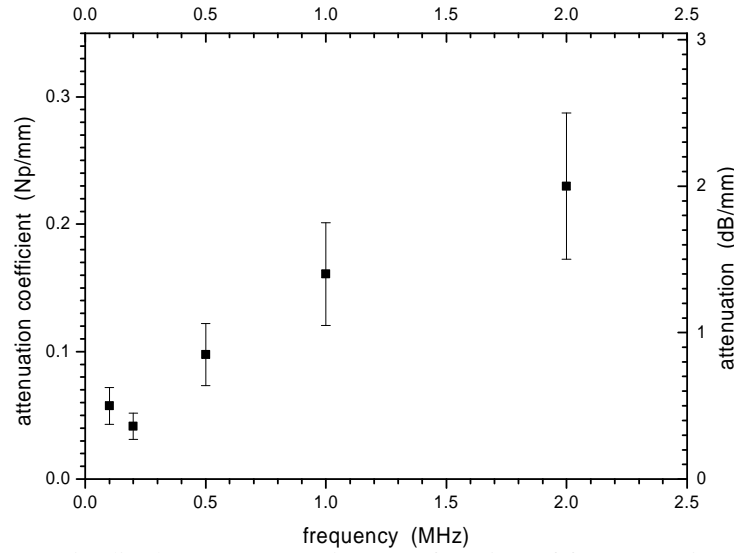
Figure 3.4. Longitudinal wave attenuation as a function of frequency in ceramic foam, measured without the use of buffer blocks.

the ceramic foam, so large was the attenuation. The data point in Figure 3.4 for the frequency 2.0 MHz is very much an underestimation of the true attenuation, as only a small component at 2 MHz was present in the received signal.

3.3.2 *Longitudinal wave attenuation measured with buffer blocks*

For this set-up only frequencies in the range 0.2 to 1.25 MHz were used. Measurements at 0.75 MHz were made with both 0.5″-diameter 1 MHz central-frequency transducers and 1.0″-diameter 0.5 MHz central-frequency transducers. Measurements of the early-arriving amplitudes were made as described above. Measurements were made four times on each sample at different positions, and averaged. The average amplitudes measured for the sample at each frequency were plotted as a function of ceramic foam thickness. A first-order exponential curve was fitted to this data to generate the attenuation coefficient. Examples of the received signals are shown in Figure 3.5, and the corresponding resultant data are shown in Figure 3.6.

Both displays of this data show considerable spread in the amplitudes. These variations are primarily due to the inhomogeneity of the samples rather than any inconsistency in measurement techniques. As mentioned earlier, the presence of large voids and inclusions (often of the order of 10 mm in diameter) strongly affect the transmitted amplitudes. The buffer block area in contact with the samples is 50 mm × 50 mm, and for each of the measurements shown in Figure 3.5 four different areas of the sample were clamped between the blocks; it was not uncommon for several inclusions or voids to be present in the cross-sectional area that was probed.

Difficulties in determining an accurate amplitude of the earliest arrival increase at lower frequencies. The beam spread of a 0.5 MHz, 1″-diameter transducer into aluminium is about 30° half-angle (Kinsler *et al.*, 2000, Chapter 7), and significantly more at 0.2 MHz. So, at low frequencies we expect the contributions to the received signals from reflections from the side walls of the buffer blocks to begin to have an effect: the arrival

27

time and amplitude of the desired signal will become camouflaged by these other signals. Moreover, the amount of energy travelling directly from the transmitting transducer to the opposite end of the buffer block (and hence through the sample and through the other buffer block) to the receiver at 0.2 MHz is low, as evidenced by the data in Figure 3.6. Different methods of measuring attenuation at these low frequencies may need to be considered.
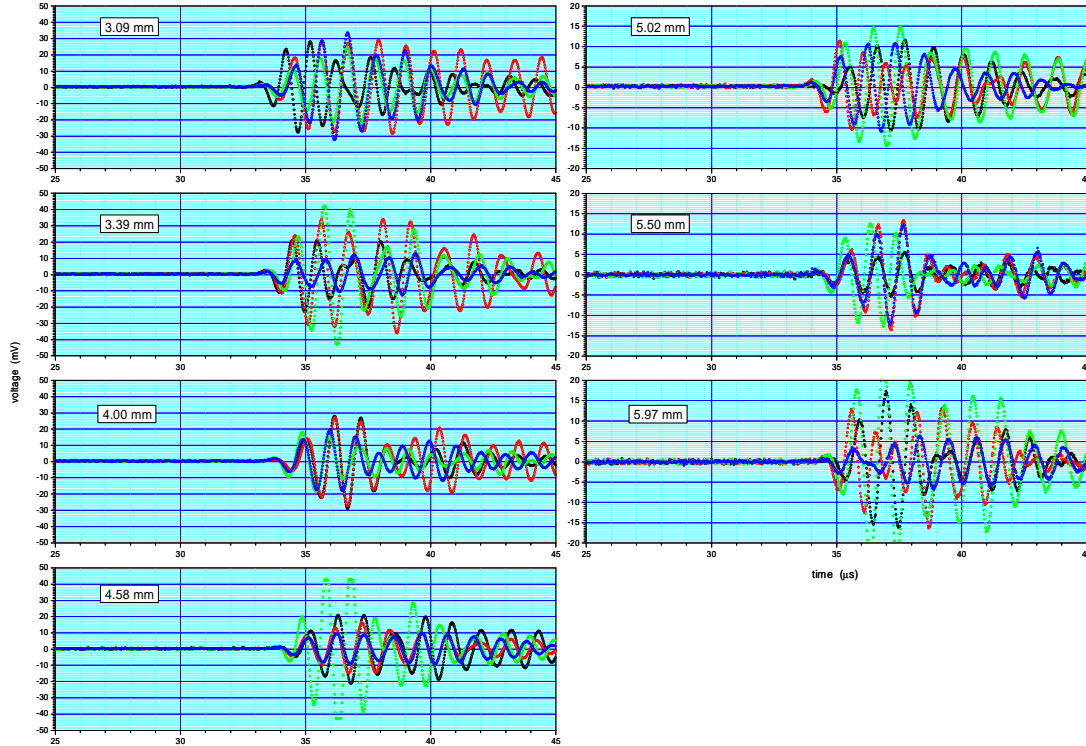

Figure 3.5. Raw data: received longitudinal wave signals measured at four different locations for seven different samples of varying thickness, using the buffer blocks, and three cycles at 1 MHz as the drive waveform.

Figure 3.7 shows the attenuation coefficient of longitudinal waves in the Cotronics ceramic foam as a function of frequency. The results from two experimental runs are displayed. The results from each of these runs are in good agreement. In the run denoted by open squares in the Figure an extra measurement of the attenuation at 0.75 MHz was made using the 1″-diameter 0.5 MHz transducer rather than the 0.5″, 1 MHz transducers normally used for the 0.75, 1.00 and 1.25 MHz measurements. The measurement for this particular case can be seen to be equal to the measurement made by the smaller transducer. In other words, no difference in the measurements was observed at this frequency when two different transducers were used.

Compared with the data taken without buffer blocks (as shown in Figure 3.4) it may be seen that while the attenuation coefficients for all of the frequencies are slightly lower when buffer blocks are not used, they still agree, within the estimated experimental error, with the measurements using buffer blocks. The exception is at the lowest frequency used, 0.2 MHz, where larger uncertainties exist due to diffraction effects and the ringing of the transducer interfering with the measurement when no buffer blocks are used.

Figure 3.6. Longitudinal wave measurements: the average amplitude (as described in the text) of the received signals as a function of ceramic foam thickness for the five different frequencies used, with the first-order exponential fits to each frequency set.
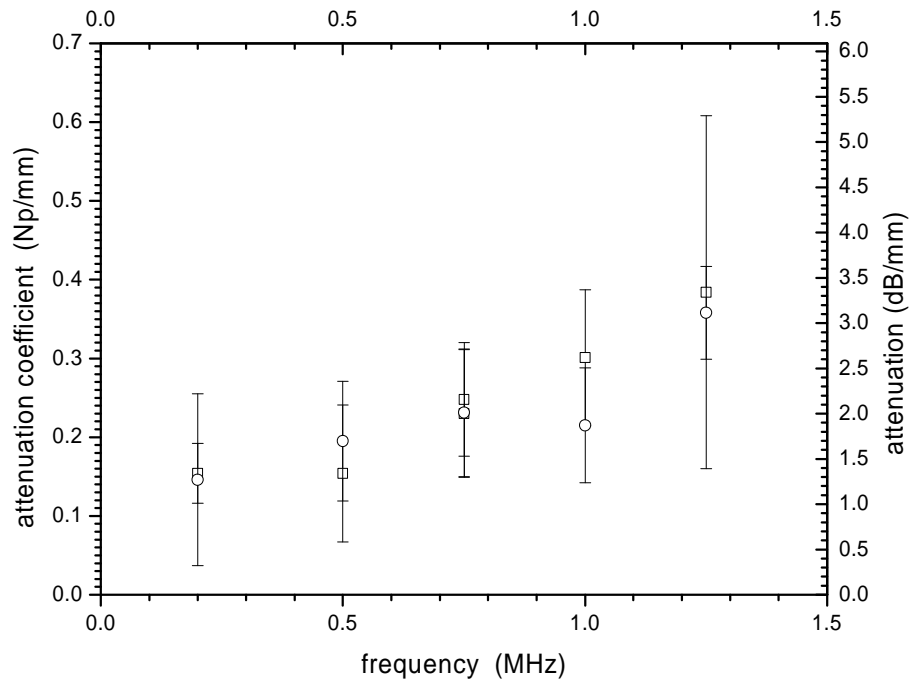
Figure 3.7. Attenuation coefficient of longitudinal waves in Cotronics ceramic foam as a function of frequency, as measured in two separate runs denoted by open squares for one and open circles for the other.

3.3.3 Shear wave attenuation measured with buffer blocks

As mentioned previously, the use of buffer blocks, doubling as longitudinal to shear wave converters, was necessary for the present experiment. The use of shear-wave transducers for these measurements will be reported later.

As was the case for the longitudinal wave measurements, measurements at 0.75 MHz were made with both 0.5″-diameter 1 MHz central-frequency transducers and 1.0″-diameter 0.5 MHz central-frequency transducers. Measurements of the early-arriving amplitudes were made as described above, and these amplitudes were plotted as a function of ceramic foam thickness. A first-order exponential curve was fitted to this data to generate the attenuation coefficient. Examples of the received signals are shown in Figure 3.8, and the corresponding resultant data are shown in Figure 3.9.

The problems discussed in the previous section regarding accurate measurements of attenuation were also true in these shear wave measurements. Additional problems arise when measuring shear waves using these 'conversion' buffer blocks. It can be seen from the example data (for 0.5 MHz) in Figure 3.8 that there exist waves that arrive earlier than the shear waves whose amplitude we are trying to measure. This is due to both the incomplete conversion of all the longitudinal wave energy incident on the angled face of the buffer block, and the effects of diffraction: it is to be expected that some longitudinal waves will arrive earlier at the receiver, by various paths, than the significantly slower shear waves, remembering that most of the time taken for the journey is spent in travelling through the aluminium buffer blocks in which the shear wave speed is less than half the longitudinal wave speed.
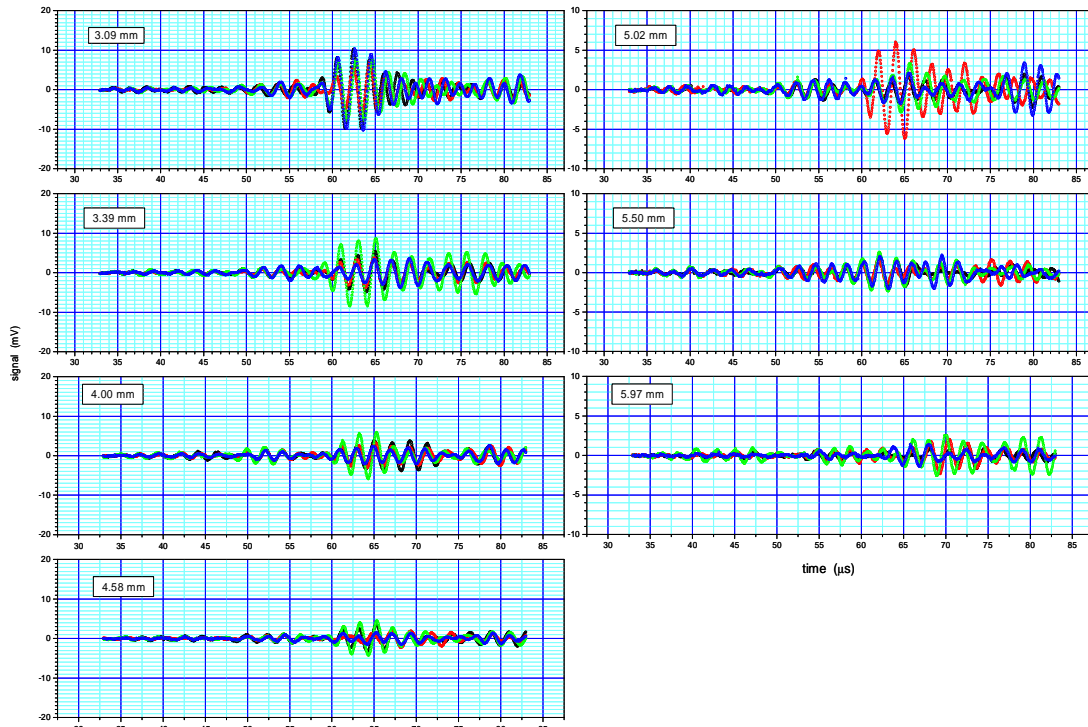
Figure 3.8. Raw data: received shear wave signals measured at four different locations for seven different samples of varying thickness, using the buffer blocks, and three cycles at 0.5 MHz as the drive waveform.
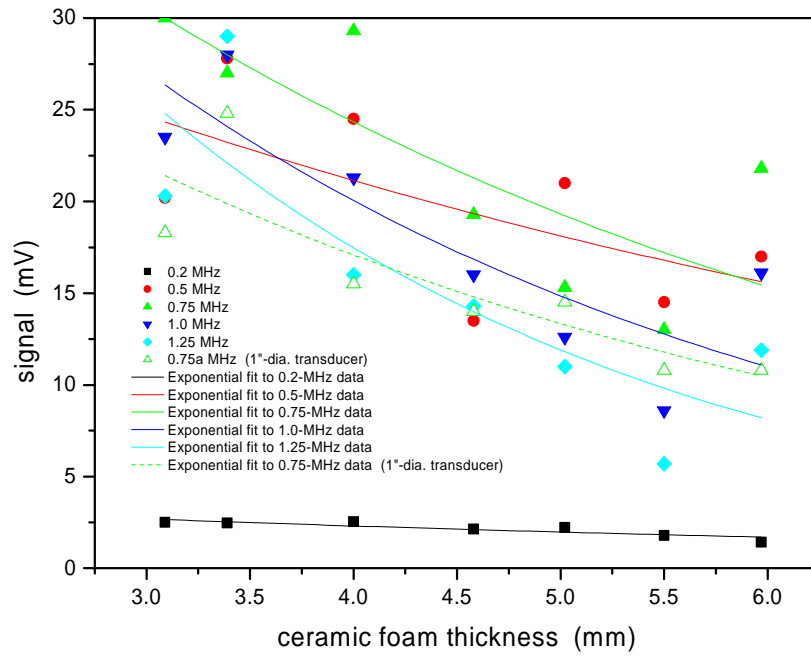
30
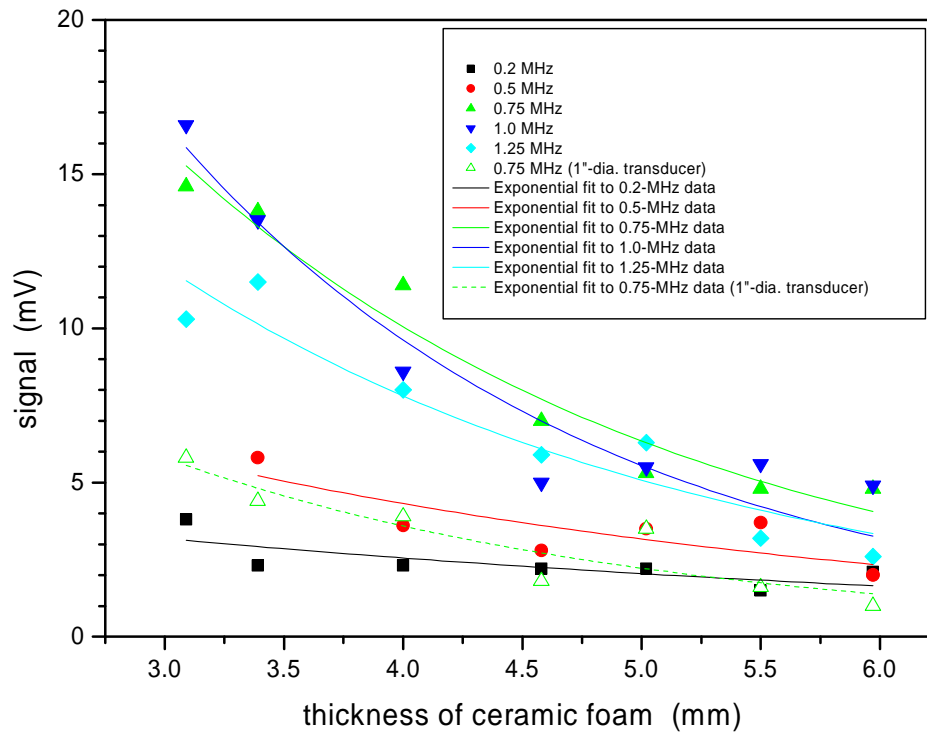
Figure 3.9. Shear wave measurements: the average amplitude (as described in the text) of the received signals as a function of ceramic foam thickness for the five different frequencies used, with the first-order exponential fits to each frequency set.

Figure 3.10 shows the attenuation coefficient of shear waves in the Cotronics ceramic foam as a function of frequency. Two measurements at 0.75 MHz were made, one with the 1″-diameter 0.5 MHz transducer, and the other with the 0.5″, 1 MHz transducer. As was the case in the longitudinal wave measurements, the attenuation is roughly linear with frequency. The data point at 1.25 MHz may be an anomaly, although further investigation of this will be undertaken shortly.

Figure 3.11 combines the results for longitudinal and shear measurements. It can be seen that the shear wave attenuation is higher than the longitudinal wave attenuation across the frequency band investigated. Putting aside for one moment the difficulties in these measurements at low frequencies, and the data for shear waves at higher frequencies, the attenuation of shear waves appears to be roughly double that of longitudinal waves.

Figure 3.10. Attenuation coefficient of shear waves in Cotronics ceramic foam as a function of frequency (two measurements at 0.75 MHz made with different transducers).

Figure 3.11. A combination of Figures 3.7 and 3.10, showing the measured attenuation of both the longitudinal and shear waves in Cotronics ceramic foam as a function of frequency.

3.4 Measurements on Zircar ceramic foam

3.4.1 Introduction

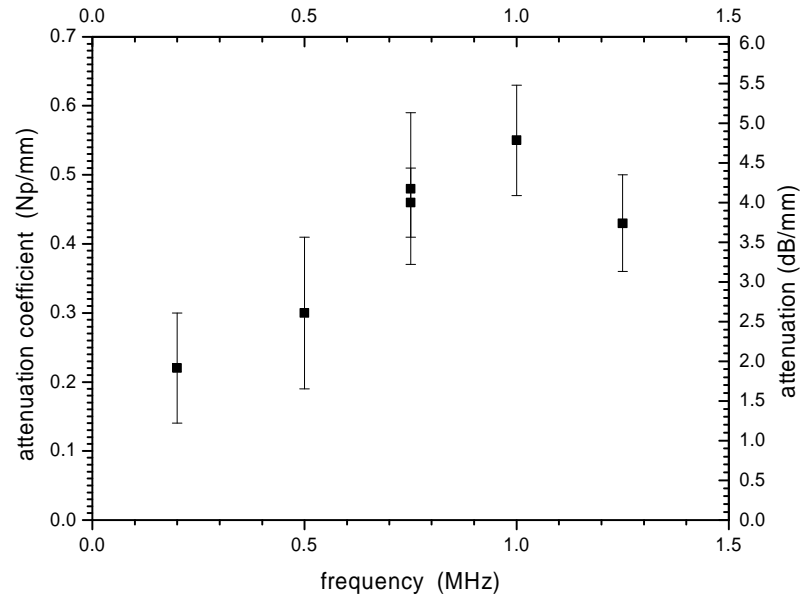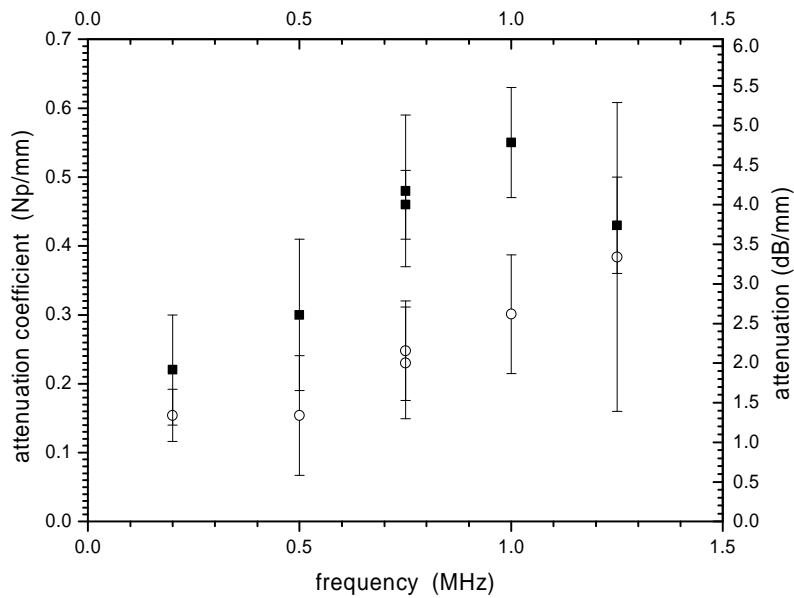The techniques described above were also employed to measure the properties of elastic waves propagating in the Zircar ceramic foam, described briefly in Section 2.2. It was immediately apparent from initial measurements that while this material appeared much more homogeneous than the visibly porous Cotronics material, it was highly anisotropic in its elastic properties. Investigation of this anisotropy was made at a single frequency, 1 MHz, so as not to complicate measurements. If appropriate, properties at other frequencies will be made in the near future.

Another constraint on the measurements was the geometry of the sample material. This material was supplied as a plate, just under 26 mm in thickness; its nominal measurements were 24 in. $\times$ 18 in. $\times$ 1 in. We arbitrarily named the direction normal to the plate's surface as 'z', and the two in-plane, orthogonal directions 'x' and 'y'. As a consequence, the samples that were prepared to investigate propagation in the x and y directions had one of their dimensions restricted to 25 mm. This meant that these 'x' and 'y' samples could not fill the full area of the buffer blocks used in these experiments (which were 50 mm $\times$ 50 mm). This was not a problem *per se*, as all of the measurements, particularly of amplitudes for the calculation of attenuation, are relative, but did require careful experimental technique to ensure the exact placement of samples between the buffer blocks so as to expose the samples to the same ultrasonic field for each measurement. Large-area samples (about 110 mm square, similar to the Cotronics samples) were prepared for the z-direction measurements. Table 4 shows the prepared sample sizes for each propagation direction. In addition to these samples, two cubes of material (25 mm $\times$ 25 mm $\times$ 25 mm)were prepared to allow velocity measurements in each orthogonal direction to be made without difference in geometry in each direction.

x-direction (y = 80 mm, z = 25 mm)	y-direction (x = 80 mm, z = 25 mm)	z-direction (x = 110 mm, y = 112 mm)
2.99	3.04	2.00
3.50	3.81	2.5
3.95	5.00	3.03
5.05	5.98	3.54
5.99	6.83	4.08
6.94	25.00	4.52
25.00		5.02
		5.55
		6.03
		7.05
		8.10
		14.48

Table 4 Sizes of samples of Zircar foam prepared for attenuation and velocity measurements.

3.4.2 Velocity measurements

3.4.2.1 Thick samples

The primary method of determining velocities was that outlined in Section 3.1, where the transit time of elastic waves through the samples was determined by measuring the time of arrival of a pulse transmitted through the sample and buffer blocks, and subtracting the average transit time of the echo signals in each buffer block. The thickness of the sample was measured carefully and the velocity then calculated. This method was used on the thicker samples (the 25-mm cubes, the 25-mm thick x and y samples, and the 14.48-mm z sample). Longitudinal and shear velocities in each orthogonal direction were thus measured.

It was found that the shear wave velocities in the lateral dimensions (x and y) depended not only on the propagation direction but also the polarization direction. No such polarization effects were found for propagation in the z direction. Results of the measurements are shown in Table 5.

Wave type	Propagation direction	Polarization direction	Velocity (km/s)
Longitudinal	x	all	3.24 ± 0.03
Longitudinal	y	all	3.27 ± 0.03
Longitudinal	z	all	0.88 ± 0.05
Shear	x	y	1.97 ± 0.04
Shear	x	z	1.06 ± 0.03
Shear	y	x	1.96 ± 0.03
Shear	y	z	1.06 ± 0.06
Shear	z	all	0.88 ± 0.08

Table 5 Velocities of ultrasonic waves at 1 MHz through Zircar ceramic.

The measured velocities do raise some interesting points. The uncertainties in the values of velocities are generally due to uncertainties in the measurements of dimensions of the samples and in determining the arrival times of wave packets. The z-direction shear wave velocity, however, did show some variation from sample to sample. Some samples taken from near the edge of the Zircar sheet showed velocities as low as 0.8 km/s, but other samples had this figure to be closer to 0.96 km/s.

Further, it appears that the longitudinal velocities in the x and y directions are approximately equal, as are the in-plane and out-of-plane shear wave velocities in these two directions. Finally, the z-direction longitudinal and shear velocities appear to be approximately equal. In a homogeneous, isotropic solid this would be difficult to imagine, implying a Poisson's ratio in this direction of infinity[1]. However, this is clearly not an isotropic solid. Even in composite materials in which velocities vary with propagation direction, the shear wave speed is usually significantly less than the longitudinal wave speed.

---

[1] Poisson's ratio in an isotropic, homogeneous solid with longitudinal wave velocity v_L and shear wave velocity v_S is given by $\sigma = \left(1 - 2(v_S/v_L)^2\right)/2\left(1 - (v_S/v_L)^2\right)$

3.4.2.2 Thin samples

The variation in velocity on each direction was an interesting feature of this material, and further measurements were undertaken to verify these figures. Instead of measuring the sample thickness and dividing it by the transit time through the material, we tried instead measuring the arrival time of the pulses through the thinner sections, which were intended and used for attenuation measurements. The sample thickness versus arrival time was then plotted and a linear least-squares fit made to the data. This method usually yielded slightly lower velocities. However, of concern with this method is that if the linear fit to this data is extrapolated back to a zero-thickness sample, the transit time is greater than that measured. In the method described in Section 3.1. the time taken for sound to travel through the buffer blocks was taken to be the average of the pulse-echo times for each block. This time agrees with that measured if the buffer blocks are brought together with no sample between them, but with a very thin layer of couplant; the agreement is within 0.05 µs. However the linear fit to the thin sample data of thickness vs arrival time consistently gave a time-axis intercept of 0.1-1.0 µs larger than the measured time. Data from both longitudinal and shear wave measurements on both Zircar and Cotronics materials of various dimensions was revisited, but there seemed to be no correlation between this difference and material or wave properties. While we are confident of our measured velocities using thick samples, the method of fitting a line to the transit time data may indicate a source of error in our measurements, one that is only significant when measuring short transit times. The 'extra time' of 0.1-1.0 µs may indicate a problem with the coupling between the buffer block and the sample causing a small, variable phase change: perhaps the block's faces are not quite parallel, perhaps the porosity of the samples contributes to the apparent delay in transit time.

3.4.3 Attenuation measurements

The technique described in Section 2.7 was used again to estimate the attenuation in Zircar ceramic. To date, measurements have only been made at 1 MHz. Results of the longitudinal wave measurements are shown in Figure 3.12, and of the shear wave measurements in Figure 3.13. It can be seen that the attenuation in the x and y directions is significantly lower than in the z direction. Further, the exponential fits to estimate the attenuation in the x and y directions rely heavily on the 25-mm data. As has been pointed out, no 25-mm thick z-direction samples were made, so no data at this thickness appears in the graphs. However, measurements made on the 25-mm 25-mm 80-mm samples indicated that the amplitude though such a thickness would be less than 1 mV, a value that would not significantly affect the fitted attenuation coefficient.

Table 6 gives the attenuations (in Nepers/mm) for the three directions and two wave types at 1 MHz. The attenuations are the absolute values of the exponential coefficient of the fitted curve ae^{bx}, where x represents distance into the sample; of course, b is negative.
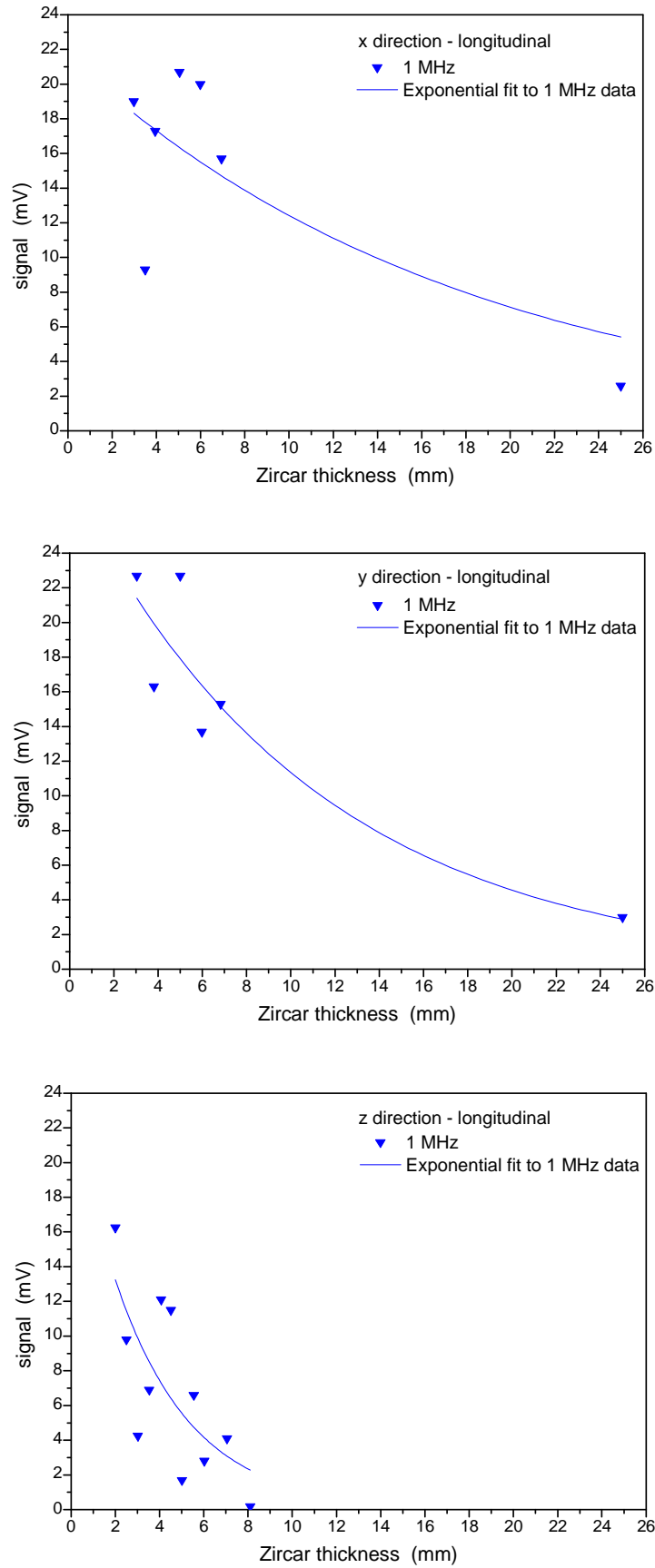
Figure 3.12. Amplitudes of received longitudinal wave signals at 1 MHz through various thicknesses of Zircar ceramic, and fitted exponential of the form ae^{-bx}.
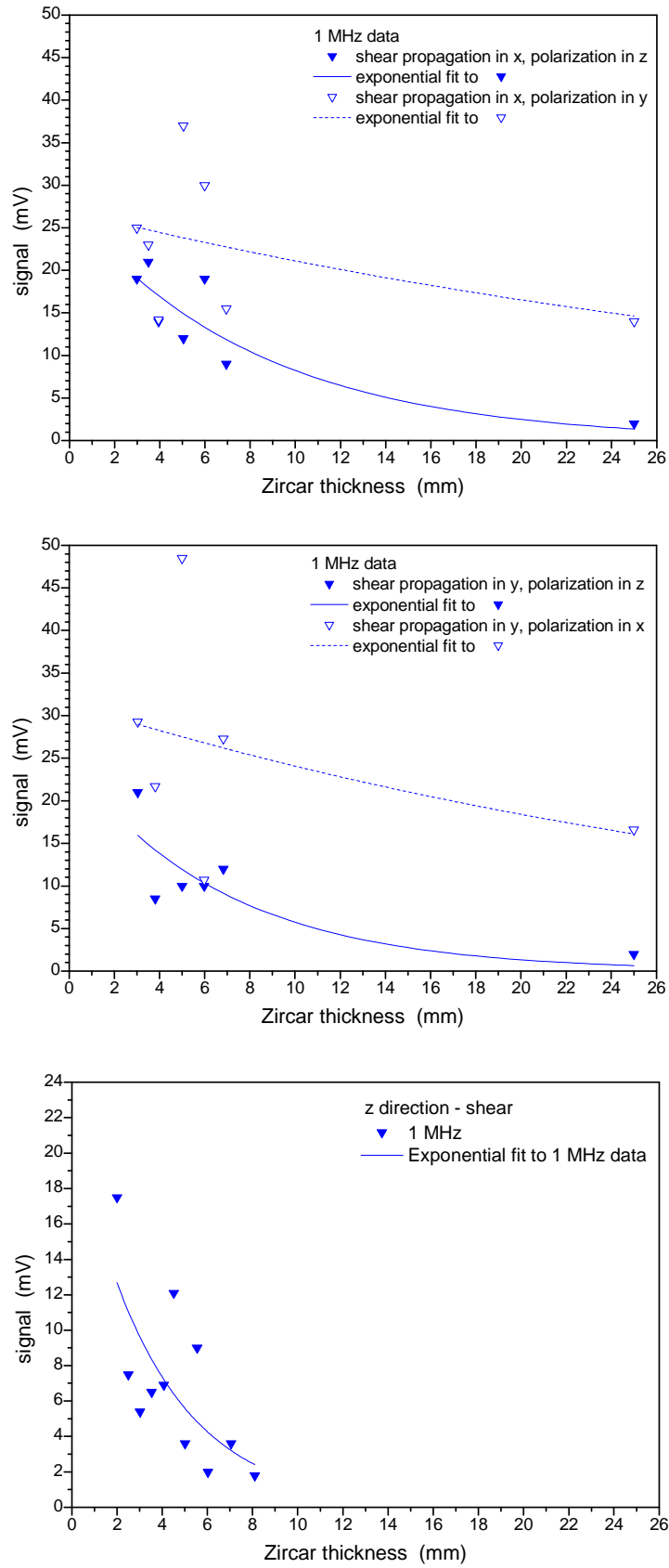
Figure 3.13. Amplitudes of received shear wave signals at 1 MHz through various thicknesses of Zircar ceramic, and fitted exponential of the form ae^{-bx}.

Wave type	Propagation direction	Polarization direction	Attenuation (Np/mm)
Longitudinal	x	all	0.055 ± 0.040
Longitudinal	y	all	0.091 ± 0.042
Longitudinal	z	all	0.29 ± 0.11
Shear	x	y	0.025 ± 0.029
Shear	x	z	0.12 ± 0.06
Shear	y	x	0.027 ± 0.042
Shear	y	z	0.15 ± 0.11
Shear	z	all	0.27 ± 0.11

Table 6 Attenuation values of ultrasonic waves at 1 MHz through Zircar ceramic.

The uncertainties on the values of attenuation are those given by the fitting program to two significant figures. The attenuation of longitudinal waves in the x and y directions is small but measurable, and may well be essentially equal. The in-plane shear wave attenuations in the x and y directions are too small to be measured by this technique. The out-of-plane shear wave attenuations in the x and y directions are marginally higher, and are barely measurable by this technique. These measurements are hampered by the generation of the faster in-plane components which arrive earlier and obfuscate the arrival of the slower out-of-plane components. The attenuations of both longitudinal and shear waves in the z-direction seem to be about equal, and significantly larger than the attenuation in the lateral dimensions.

3.4.4 Measurements with shear-wave transducers

During the course of these experiments two shear-wave transducers were acquired (with centre frequencies of 1 MHz). These were used in two set-ups: with buffer blocks, directly substituting them for the longitudinal-wave transducers in the buffer rod rig (Figure 2.7 and Figure 2.8 (left)); and without buffer blocks, and pressed directly onto the surfaces of the ceramic samples. Both of these arrangements yielded results (attenuation and velocity) in agreement with measurements made with the shear-wave conversion buffer blocks (Figure 2.8 (right)).

3.4.5 Broadband measurements

We have not as yet made measurements of the dependence of attenuation on frequency for the Zircar ceramic material. As we have seen, the attenuation in many directions is low, and so making such measurements at lower frequencies, where the attenuation is expected to be lower, may be problematic. For the Cotronics material transducers with different centre frequencies were used to measure attenuation at different frequencies. However, an often-used technique of pulsed excitation followed by a frequency analysis was attempted here using the 1-MHz shear-wave transducers and a pair of 1-MHz longitudinal-wave transducers. The Panametrics Ultrasonic Analyzer described in Section 3.2 was used to generate a spike excitation pulse, and the resulting transmitted signal was captured and Fourier transformed. This technique yielded attenuation figures not inconsistent with the measurements given above: for longitudinal waves in the z direction the measured attenuation was 0.18 Np/mm, and for shear waves 0.30 Np/mm.

However, in both cases the uncertainty in the measurements was the same as the value. Without improvement in the signal-to-noise ratio of this technique, it is of limited value here.

3.5 Measurements of wave propagation in impacted TPS-like tiles

3.5.1 Preliminary experiments

Prior to studying the effects of different impacts on the ceramic foam, a preliminary investigation of the propagation of guided waves in the aluminium sheet was undertaken. Firstly, using longitudinal-wave transducers coupled to the sheet via a Perspex (polymethyl methacrylate, or Plexiglass) wedge to generate guided waves of fixed phase velocity (approximately 8430 m/s), the guided wave spectrum of the aluminium sheet at this phase velocity was measured and also of the sheet with the ceramic foam bonded to it. These measurements were similar to those carried out in previous work (Scott and Price, 2002). The spectra taken in these two cases differed only in amplitude, the presence of the ceramic foam reducing the received signals by a factor of about three. An example of one of these spectra is given in Figure 3.14. There was no easily recognisable difference between the propagation characteristics of an aluminium sheet with or without foam bonded to it, apart from an overall amplitude change.
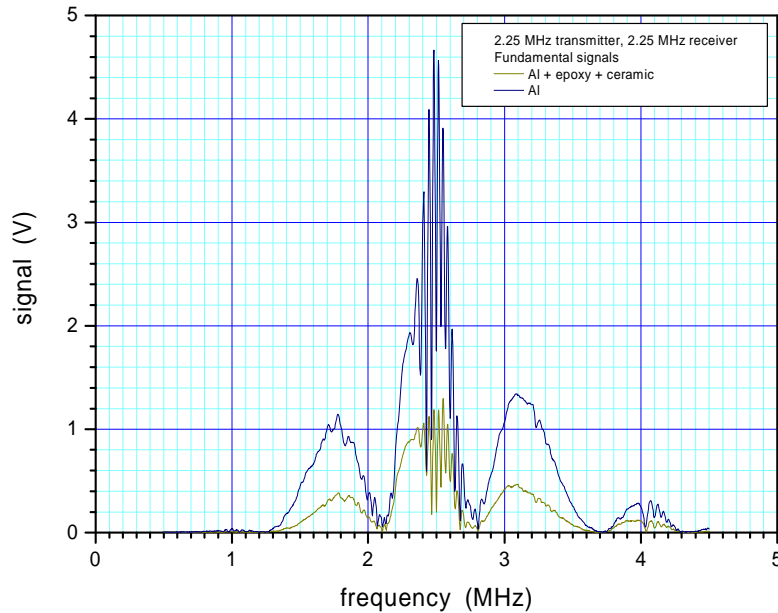
Figure 3.14. Guided wave spectra of a 3.175-mm thick aluminium sheet, and a similar aluminium sheet with ceramic foam bonded to it, measured at a phase velocity of 8430 m/s.

The second experiment used the set-up described in Section 2.8.2, and simply consisted of focusing the pulsed laser beam onto the surface of the aluminium sheet directly, not onto the foam, and monitoring the output of the transducers. The effect of the fast laser pulse was a broadband excitation of the aluminium sheet at a point, generating a broad spectrum of elastic waves which then propagated through the aluminium sheet as guided waves. The signal as measured by one of the small PVDF transducers, situated 57 mm from the impact point, is shown in Figure 3.15. In this Figure we have also plotted the predicted waveform as calculated for an infinite sheet by the program Disperse[®] (see

Pavlakovic *et al.*, 1997). The 'excitation pulse' for the simulated waveform was one cycle of 1 MHz. It can be seen that these two waveforms agree well in their basic constituents, and Disperse® may be used to identify the individual modal components that make up the waveform, which all travel with different group velocities at different frequencies.
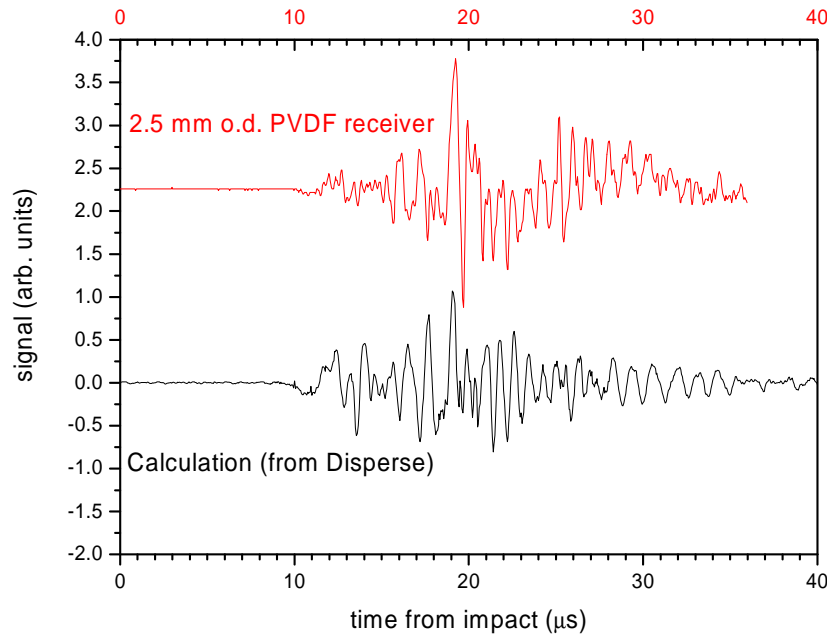

Figure 3.15. Experimentally measured waveform generated by a laser pulse on a sheet of 3.175-mm aluminium and measured 57 mm away by a PVDF transducer (upper trace), and the waveform as predicted by the Disperse® program.

3.5.2 Laser impacts on foam

In this and in the following section it will be seen that, smaller features aside, the signals from all of the transducers for a particular type of impact, are very similar: oscillations at megahertz frequencies and below for laser impacts, and oscillations at a few kilohertz and below for the low-velocity pendulum impacts. Signals arising from impacts directly onto the aluminium plate are also easily distinguishable from those caused by impacts on the foam.

Measurements of the signals generated by laser impacts were made at different distances from the impact site. The laser was first focused onto the firebrick at a position directly opposite the position of the measuring transducer, effectively distant from the impact by the thickness of the ceramic foam, adhesive bond layer and the aluminium sheet. The sample was then moved 10 mm in a lateral direction so the laser beam (effectively) was moved towards the centre-line of the ceramic foam, and another measurement was made. Measurements continued to be made after moving the sample laterally in increments of 10 mm. (The direction of movement was such that all six measurements were taken with the laser always impacting on the ceramic foam.)

These measurements were made for all five different transducers, the two sizes of PVDF, and the three sizes of PZT. The results are shown in Figures 3.16 and 3.17.

Figure 3.16. Signals from three different PZT transducers resulting from laser impacts 0, 10, 20, 30, 40, and 50 mm away from directly opposite the transducers. Left: PZT 2.5 mm dia. and 0.5 mm thick. Centre: PZT 5.0 mm dia. and 0.5 mm thick. Right: PZT 5.0 mm dia. and 2.0 mm thick.
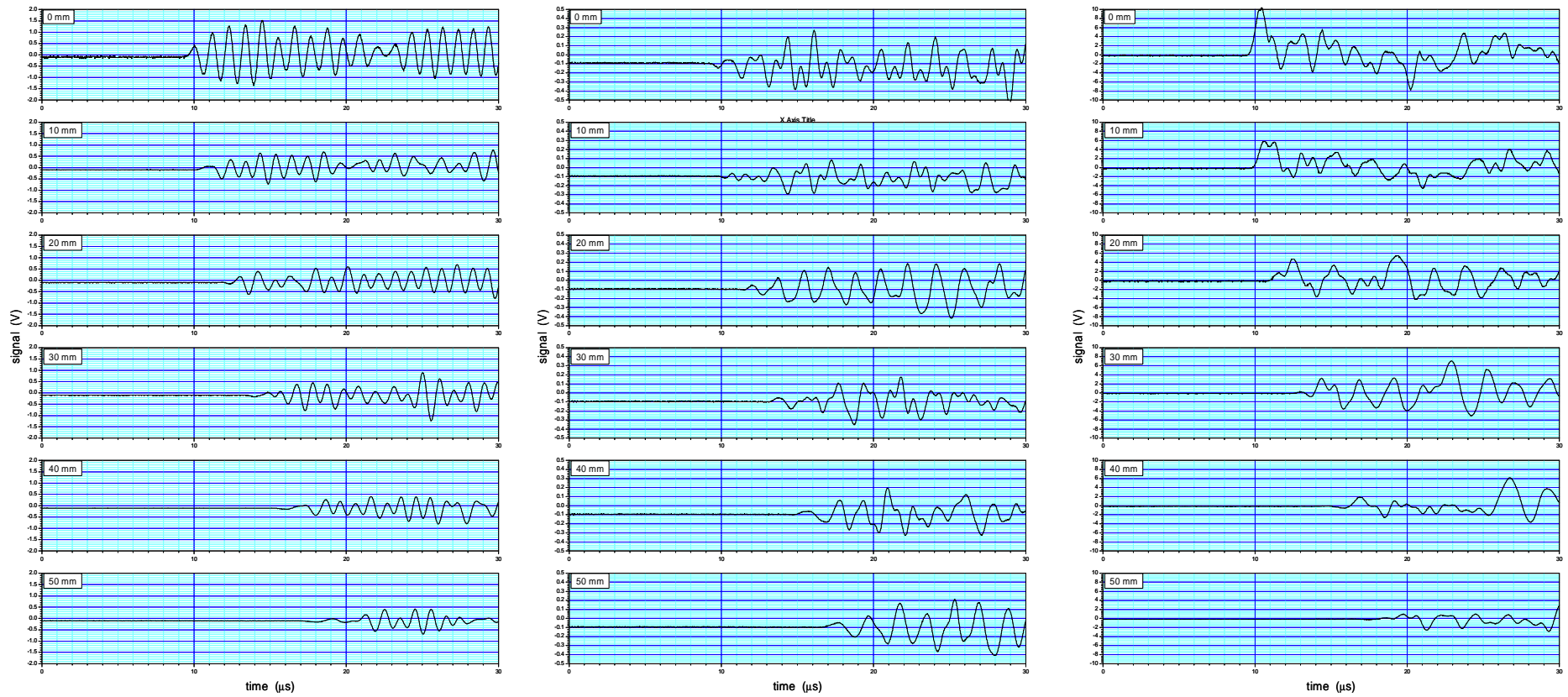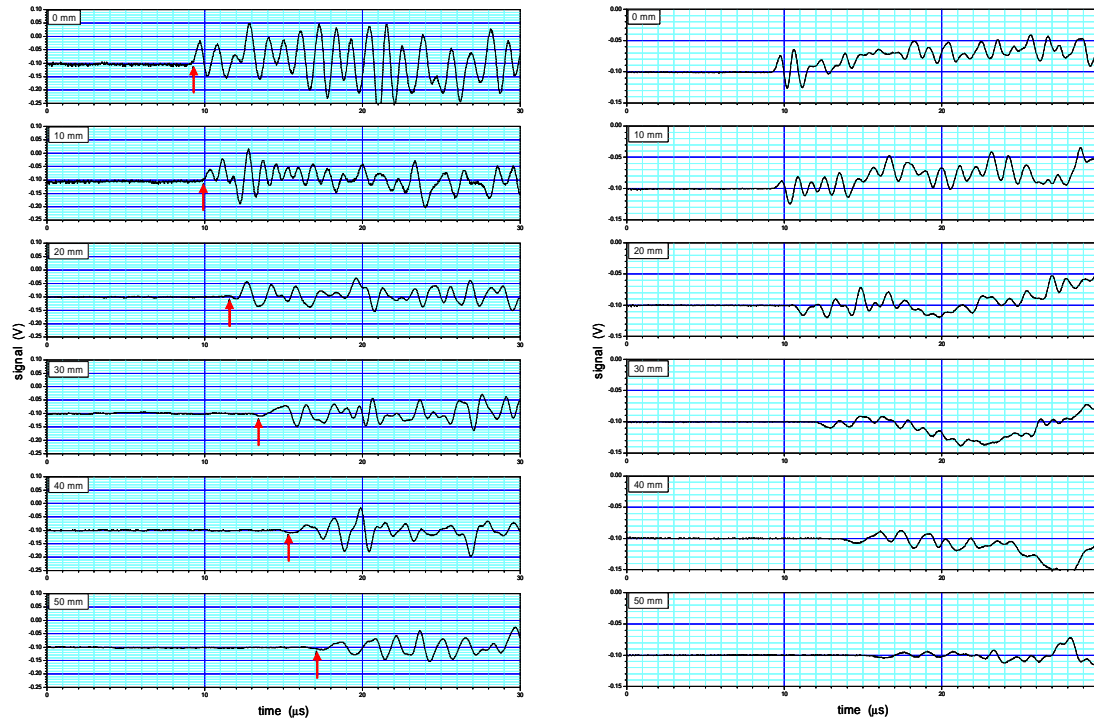
Figure 3.17. Signals from two different PVDF transducers resulting from laser impacts 0, 10, 20, 30, 40, and 50 mm away from directly opposite the transducers. Left: PVDF 2.5 mm dia. and 0.05 mm thick; red arrows indicating expected arrival times are explained in the text. Right: PVDF 10.0 mm dia. and 0.05 mm thick.

All of the signals show the attenuative nature of the ceramic foam, with frequencies above about 1 MHz attenuated strongly. It is worth noting the very different nature of the signals generated when the laser pulse strikes the ceramic foam and when it strikes the aluminium sheet directly (compare the signals in Figure 3.17 (left) with Figure 3.15 (upper)).

The through-thickness fundamental resonance frequency of the 0.5-mm thick PZT transducers is about 4 MHz, but it is not in evidence in these signals. The first radial mode of the 2.5 mm diameter PZT transducer is at about 1 MHz , which may well be enhancing this frequency component in these signals. At 1 MHz the wavelengths of the elastic waves travelling in the foam are 2 - 3 mm, and the guided waves in the aluminium will have wavelengths up to about 5 mm. These longer wavelengths may well cause some phase cancellation in the larger diameter transducers, thereby reducing the relative size of the 1 MHz component, shown in Figure 3.16 (centre and right). We might also expect less distinct radial and through-thickness modes in the thick PZT transducer as the radius and length of the transducer are comparable and mode mixing is expected. There are also low-frequency components (of the order of 50 kHz or so) that appear in the signals, and are more noticeable in the signals from the larger diameter transducers.

Another interesting feature of the signals is the early arrival of low-frequency components. This is especially noticeable in the outputs of the smaller transducers (see Figure 3.16 (left) and Figure 3.17 (left)). We have made some simplifying assumptions to calculate the fastest path taken by elastic waves from the impact site to the detecting transducer: that the fastest speed in the ceramic foam is that of longitudinal waves, at 2.9 mm/μs, that there is no adhesive bond layer, and that the fastest waves in the aluminium sheet are of the S_0 fundamental extensional wave, at a speed (group velocity) of 5.4 mm/μs, and that the longitudinal waves in the foam when they impinge on the aluminium sheet are converted into the S_0 plate waves. With these assumptions we have calculated the path taken by the fastest waves to be that of travelling from the impact site to the aluminium sheet so as to impinge on the sheet at an angle dependent only on the relative velocities in the ceramic foam and the aluminium (see Appendix A). This angle between the wave vector of the longitudinal waves emanating from the impact site and the aluminium plate on which it impinges, θ, is found to be $\cos^{-1}(v_f /v_a)$ where v_f is the longitudinal wave velocity in ceramic foam, and v_a is the fastest group wave velocity (for the S_0 mode at low frequencies) in the aluminium sheet; $\theta = 58.8°$ in this case. The calculated arrival times for lateral displacements greater than 20 mm or more are shown in Figure 3.17 (left) by the arrows. For lateral displacements of 0 mm and 10 mm the longitudinal waves in the foam impinge on the aluminium sheet at an angle greater than $\cos^{-1}(v_f /v_a)$, so the transit times through the foam via the direct line between the impact site and the transducer are shown in the upper two frames of Figure 3.17 (left). These calculations are in good agreement with the measured arrival times.

3.5.3 Pendulum impacts on foam
Measurements of the signals generated by pendulum impacts were also made at different distances from the impact site. As with the laser impacts, the pendulum was first positioned so as to hit the firebrick at a position directly opposite the position of the measuring transducer. The sample was then moved laterally in 10-mm increments, with measurements made at each position, again with all six measurements taken with the pendulum always hitting the ceramic foam. (The polarity of these signals is not

important, and just depended on which side the positive output of the poled transducers was bonded to the aluminium.)

These measurements were made for all five different transducers. The results are shown in Figures 3.18 and 3.19. In Figure 3.18 (left) and Figure 3.19 (centre) the red trace is the output of the transducer that formed part of the impacting head of the pendulum, and provided the trigger signal for the acquiring oscilloscope. This signal indicates the force applied by the impactor as a function of time. The slow nature of the deceleration of this impact is displayed by this signal, and the resulting elastic waves take on the fundamental frequency of this impact, i.e. about 2.5 kHz. The smallest PZT transducer signal also displayed the arrival early in the transient of a small component of signal at a frequency of about 20 kHz. The largest PZT transducer suffered saturation of its output at the 'standard' pendulum impact energy of 41 mJ, and so this energy was reduced to 8 mJ to obtain an undistorted signal (shown in red in the right-hand panel of Figure 3.19).

The output of the smaller PVDF transducer also showed some anomalies. The 2.5-mm diameter PVDF transducer signal (Figure 3.19 (left)) showed a strong component at a frequency of 25 kHz, which was not evident on the output of the larger diameter PVDF sensor (Figure 3.19 (right)). The measurements were retaken using the smaller PVDF transducer, but without the amplifier – instead its output was monitored directly by the oscilloscope, and the resultant signals are shown in Figure 3.20 (centre). While some 25 kHz component remained in these signals, it appears that the combination of this size PVDF transducer and the amplifier we used gave rise to an oscillation at 25 kHz. We examined the transducer bonded to the aluminium sheet with and without the amplifier using a gain-phase analyser, but found no evidence of a resonance at this frequency. Further investigation of this phenomenon is underway.

Another feature of these signals, common to both the 2.5-mm diameter PZT and PVDF transducers, was a high-frequency component present from about 50 μs after the impact to about 500 μs. This was measured to be at about 1 MHz. The larger diameter transducers did not display this signal (apart from the saturated output from the large, thick PZT transducer). Given this signal is seen in the output of two different transducers, it is unlikely to be a resonance phenomenon of the transducer. One possible explanation is that the aluminium sheet is indeed reverberating at frequencies at and below about 1 MHz as a result of the impact (higher frequencies are attenuated too much by the ceramic foam and do not reach the aluminium plate), the reverberation lasting for hundreds of microseconds. We found in earlier work on 1-mm aluminium panels used on the Concept Demonstrator that reverberations from impacts last a few milliseconds, but with the TPS-like tile the ceramic foam glued to the panel will help damp these reverberations. This too will be clarified with further work.

These smaller features aside, the signals from all of the transducers for a particular type of impact, are very similar: oscillations at megahertz frequencies and below for laser impacts, and oscillations at a few kilohertz and below for the low-velocity

Figure 3.18. Signals from three different PZT transducers resulting from pendulum impacts 0, 10, 20, 30, 40, and 50 mm away from directly opposite the transducers. Left: PZT 2.5 mm dia. and 0.5 mm thick. The red trace in the upper frame is the signal from the transducer in the impactor. Centre: PZT 5.0 mm dia. and 0.5 mm thick. Right: PZT 5.0 mm dia. and 2.0 mm thick. The black signals are from the same energy impact as the other impacts, but was found to saturate the output of this transducer. The impact energy was lowered by a factor of about five, generating the red signals.

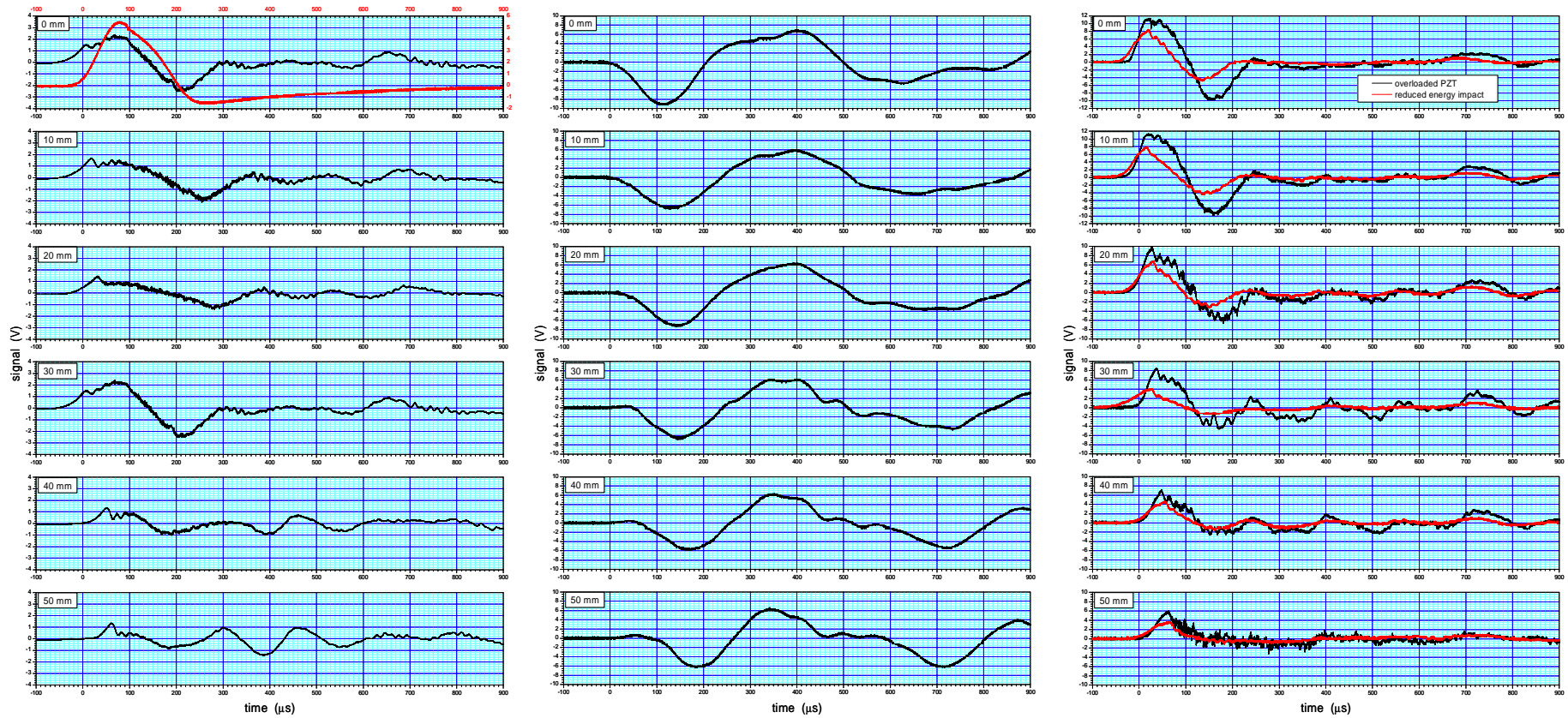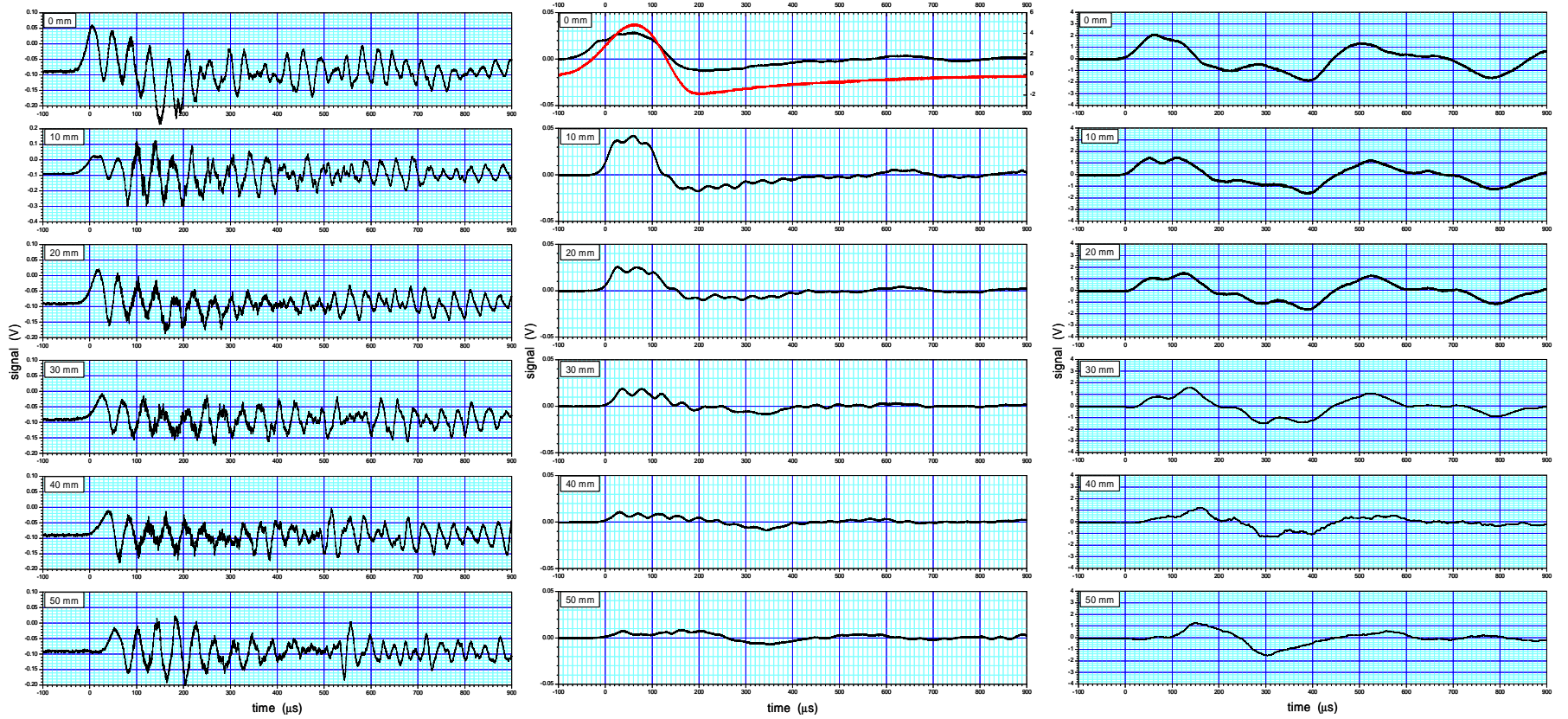Figure 3.19. Signals from two different PVDF transducers resulting from pendulum impacts 0, 10, 20, 30, 40, and 50 mm away from directly opposite the transducers. Left: PVDF 2.5 mm dia. and 0.05 mm thick. Centre: same transducer as at left, but without using the amplifier. The red trace in the upper panel shows the output of the transducer in the impactor. Right: PVDF 10.0 mm dia. and 0.05 mm thick.

pendulum impacts. Signals arising from impacts directly onto the aluminium plate are also easily distinguishable from those caused by impacts on the foam.

These results, the frequency content of the signals, transit times, and attenuation with distance from the impact site, will be used in conjunction with our modelling to determine the locations and numbers of sensors needed to detect impacts of a given energy. Two quite different types of impact have been investigated here, at only one energy level for each of them, so further discussions on suitable impact simulations, and their dependence on energy, are necessary.

3.5.4 Measurements on fully insulated tile

In order to more closely approximate the transmission and detection of acoustic waves through an insulated tile, a piece of 20-mm thick Cotronics ceramic foam was bonded to a 3-mm thick piece of aluminium; both materials were 220 mm x 200 mm, the size of the 'standard' aluminium panels used on the Concept Demonstrator. The adhesive used was RTV106, as used by NASA in their fabrication of thermal test pieces, and was applied to a thickness of about 0.25 mm. Onto the back of the aluminium sheet were bonded sixteen piezoelectric sensors, in the pattern used on the Concept Demonstrator (see Figure 3.20).
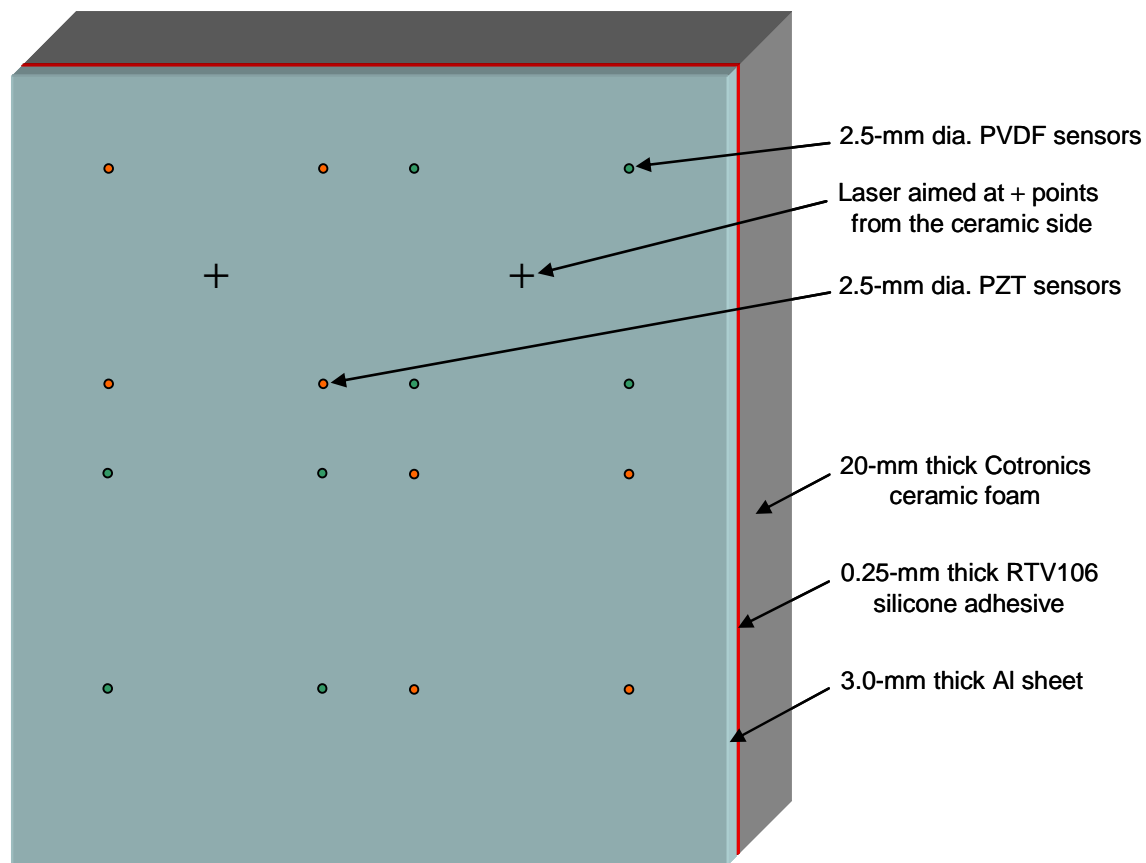

Figure 3.20. Insulated tile prepared to study acoustic propagation, showing two sets of four PZT sensors and two sets of four PVDF sensors. Laser 'impacts' were on the ceramic foam, aimed at the centre of the top two sets of sensors, as indicated by the crosses.

The outputs of all four PZT (or PVDF) sensors were monitored simultaneously; the laser was focused onto the Cotronics foam, with the line-of-sight aimed at the centre of the set of four transducers. Four sets of data were acquired: one monitoring the output of the PZT transducers with the laser centred on the PZT transducers, one with the laser centred on the other set of transducers (i.e. 85 mm in a horizontal direction from the first impact point), and the other two sets monitoring the outputs from the PVDF transducers with the laser similarly aimed at the centre of the sensor array, and at the centre of the neighbouring array. The results of these measurements are shown in Figure 3.21.

These measurements show the following. Firstly, while the signals arrive simultaneously at the four sensors when the impact is equidistant from each sensor (the aiming point is 42 mm from each sensor), the amplitudes of the received signals vary by about a factor of two for the PZT sensors, and a larger factor for the PVDF sensors. Our experience of bonding such sensors indicates that this variation is larger than the variability one might expect from slightly different bonding conditions of each sensor (they are all bonded by hand). We have tentatively ascribed this to the porosity of the Cotronics foam: pores and inclusions along the path travelled by the elastic waves may well influence the received amplitudes.

Secondly, the signal amplitudes measured by the PVDF sensors are significantly smaller that those of the PZT sensors.

Thirdly, the signals measured when the adjacent cell is impacted (when two sensors will be 62 mm from the aiming point, and the other two 119 mm distant) clearly show the two arrival times. The graph at the lower left of Figure 3.21, showing the signals with increased gain, shows these two arrival times. This demonstrates the feasibility of triangulation of the impact point from such signals. Higher gain and filtering may be needed to clearly distinguish the much smaller PVDF signals for impact location. The arrival times of all these signals are consistent with the analysis presented in Section 3.5.2 and Appendix A.

These experiments indicate that for the 20 mm of Cotronics foam, bonded with 0.25 mm of RTV106 to 3-mm aluminium plate, a sensor density of 2.5-mm PZT discs close to that of the present arrangement (i.e. evenly distributed, 60 mm to 80 mm apart) will be necessary to locate impacts, notwithstanding better signal processing.

3.6 Conclusions

The velocities of sound in Cotronics ceramic foam have been found to be for longitudinal waves 2.90 ± 0.05 mm/μs, and for shear waves 1.80 ± 0.05 mm/μs. The attenuation of these waves was found to be approximately linear with frequency: values at 1 MHz are 0.3 Np/mm (2.6 dB/mm) for longitudinal waves, and 0.55 Np/mm (4.8 dB/mm) for shear waves. Measurement of all these properties has been
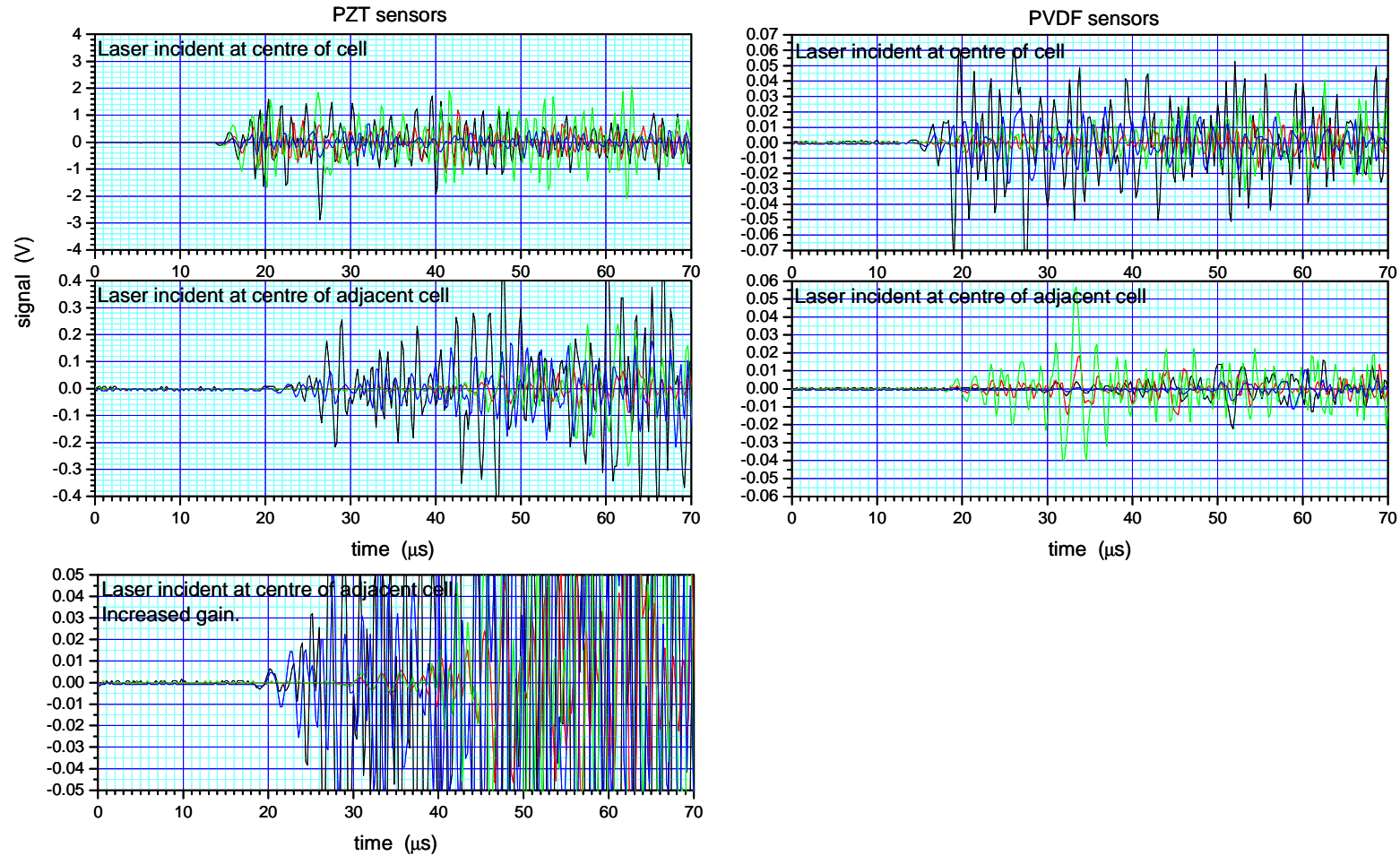
Figure 3.21. Signals measured using PZT sensors (left) and PVDF sensors (right) for laser impacts at the centre of each sensor array (upper), and at the centre of the neighbouring array (lower), using the tile illustrated in Figure 3.20. The lowest trace on the left shows the signals from the PZT sensors when the neighbouring cell is hit, but with increased gain on the sensors electronics to clearly show the arrival of waves at the two nearer (black and blue traces) and two farther (green and red) sensor pairs.

49

hampered by the inhomogeneous nature of the ceramic foam which is riddled with both porosity, with sizes ranging from tens of micrometers to tens of millimetres, and with hard inclusions up to about 10 mm in diameter. When only used as a thermally insulating material these flaws may not be important, but when investigating the propagation of ultrasound though such a material, these flaws cause large variations in measured signals.

The propagation of elastic waves in Cotronics ceramic foam in the kHz to MHz range has also been investigated, with high- and low-energy impacts, using a pulsed laser beam and a pendulum, giving rise to easily distinguishable signals from piezoelectric transducers bonded to one side of an aluminium sheet, the other side of which has the ceramic foam bonded to it. These measurements were consistent with the measured velocities and attenuations.

Measurements on the Zircar insulating material have indicated a high degree of anisotropy. The longitudinal wave velocities in the plane of the sheet (x and y directions) are significantly higher than in the direction normal to the sheet (z). Correspondingly different attenuations are also measured in these directions: low in the plane of the sheet and high normal to it. The propagation of shear waves shows that their velocity and attenuation are affected not only by their direction of propagation but also their direction of polarization. Such anisotropy complicates modelling of elastic waves, and possibly thermal flow, in the tiles; and consequently location of impacts and the effects of damaged thermal integrity may also be complicated.

4. Acoustic modelling

4.1 Introduction

Modelling of acoustic propagation in the materials and structures of interest in this work is difficult due to the high attenuation in the ceramic foam, the anisotropic and inhomogeneous nature of the foam materials used here, and the large differences in the acoustic properties of the different materials that make up the structures (e.g. aluminium and ceramic foam). Because of this, a three-pronged approach is being taken to the modelling. It is likely that none of the individual approaches will satisfactorily provide a complete acoustic model, but that the results of more than one approach will enable optimised designs to be developed and evaluated.

Acoustic models of the materials and structures involved in this work are being developed for two purposes. The first is to aid the interpretation of measurements of the acoustic properties of the materials and structures, when either transient or pseudo-continuous elastic waves are used for the measurements. The second is to inform the design of sensor layouts, and to aid the interpretation of received signals when the structure is impacted. Central to the achievement of this second objective is the modelling of transient waves (elastic pulses produced by transient loads) within the structure. Satisfactory modelling of transient propagation in the materials and structures of interest has not yet been achieved: this will be discussed further below.

The three approaches to be developed are as follows.
a)   The first approach is a model that calculates the elastic guided wave propagation in a multi-layered plate of infinite extent in the x-y plane. The materials of the layers may be isotropic or anisotropic, and the propagating waves may be generated by an incident plane wave of infinite extent, by a spatially bounded ultrasonic beam incident through a coupling fluid, or by a surface load. Such a model has been developed and used by us in earlier work (Price *et al.*, 1999, Ogilvy, 1995). This semi-analytic model is capable of calculating guided wave propagation at all frequencies, but it cannot readily account for the effects of edges and discontinuities in the structure.

This model is supplemented by the commercially-available program Disperse®, developed at Imperial College, London (Pavlakovic *et al.*, 1997). This program calculates the dispersion curves for multi-layered, planar structures, but does not calculate the response to a specific excitation.

b)   The second approach is to calculate numerically the normal modes (or acoustic resonances) of a tile structure, using the method outlined by Visscher *et al.* (1991). This method, at least in principle, allows the exact shape of the tile structure to be taken into account. However, for computational reasons it is limited to the relatively low frequency resonances of the structure (e.g. the lowest ~200 modes), and it has difficulty when the structure contains materials with very different acoustic properties (e.g. aluminium and ceramic foam), at least for the simple basis functions used in this work. This technique allows for the application of transient loads.

c)   The third approach is a finite element model. In principle such a model can calculate acoustic propagation in any complex 3D structure, but in practice the number of elements that can be incorporated into the model is limited. Thus, as with b), there is a limitation to relatively low frequency propagation since elements should be significantly smaller than the propagating wavelength. Advantages of this approach compared with b), however, are that it is possible to get much higher spatial resolution using a 2D approximation, and it is quite straightforward to model a structure containing very different materials.

None of these models is yet complete, and in fact, due to financial constraints we have yet to acquire the commercial finite element package needed to develop model c), so no work has yet been done using the finite element approach. However, preliminary calculations have been carried out using approaches a) and b), and a finite element package will be purchased within the next month.

4.2 The guided wave model

The guided wave models are not well suited to the case of a point impact on a plate of finite lateral extent. They assume plates (which may be multi-layered and composed of isotropic or anisotropic materials) of infinite extent, and continuous wave (narrow band) excitation. They can be very useful for obtaining a qualitative or semi-quantitative understanding of pseudo-continuous (long pulse) wave propagation in finite plates, but are limited in their application to transient wave propagation.

The core of the model is a calculation of the propagation within and external to the plate, generated by an infinite plane wave of frequency f, incident on the surface of the plate at angle θ, from a fluid coupling medium. Thus, the wave propagation is infinite in both spatial and temporal domains. Fourier techniques can be used to reduce both the spatial extent of the incident beam using, for example, the angular spectrum method to approximate a bounded beam, and also, in the time domain, to model a short pulse. However, this approach becomes highly inefficient for calculating the impulse response to a point impact.

Some exploratory calculations were carried out for the Cotronics foam/aluminium bonded plate, particularly to examine the feasibility of the transit time model outlined in Section 3.5.2 and Appendix A. However, while it was established that there are modes that capture significant energy propagating along the aluminium component of the plate, as required, it could not be confirmed that the group velocity of a pulse propagating in these modes would be close to the longitudinal velocity in aluminium.

There are a number of approaches to the modelling of transient wave propagation in plates, including generalised ray methods (see, e.g., Pao and Gajewski, 1977) and the normal mode expansion method (e.g. Cheng and Berthelot, 1996) in which the transient displacement field is expressed as a summation of the Rayleigh-Lamb modes of the plate. These techniques will be investigated and a more appropriate model developed during the next phase of this work.

4.3 The normal mode model

The normal mode approach has the potential to allow accurate modelling of transient wave propagation in multi-layered tiles, particularly if the set of basis functions chosen provide a compact representation of the normal modes: in this case the matrix to be diagonalised contains relatively few and small off-diagonal elements, and the calculated eigenfunctions are likely to be accurate approximations to the normal modes of the structure. However, such a set of basis functions may be difficult to identify, even for a simple shape such as a rectangular tile, if the acoustic properties of the materials of the layers are significantly different, as is the case for the Cotronics foam/aluminium tiles of interest here.

Initial implementation of this model has been based on the approach of Visscher *et al.* (1991), who used a simple set of polynomial basis functions of the form $x^l y^m z^n$, chosen to provide a simple set of functions suitable for a wide variety of solid shapes. However, it is certainly not an optimal set for the present case, and results in modes that are inaccurate at all but the lowest frequencies.

A further difficulty with the normal mode model is that of including effects of acoustic attenuation/damping in the calculations, and this is an important issue for the ceramic foam, which is highly attenuative at the frequencies of interest here (see Section 3).

Damping is accounted for by adding a retarding force, proportional to the particle velocity, to the wave equation. There are two ways of doing this. Firstly, by incorporating the damping term in the calculation of the normal modes, i.e. by including the damping term in the homogeneous differential equation that is to be solved. In this case, the formal approach adopted by Visscher and others, based on Hamilton's variational principle, breaks down because the damping forces are non-conservative (dissipative). While a more general approach based on d'Alembert's principle is possible (e.g. Goldstein, 1950), this has not yet been explored in this work.

The second approach is to calculate the normal modes in the absence of damping, and to include the damping terms into the solution of the forced vibration problem. This approach is outlined by Meirovitch (1967), and has been followed here even though it is more appropriate for weak damping. The damping couples the (undamped) normal modes, so instead of solving a simple uncoupled set of differential equations to solve the forced vibration problem, a more complicated set of coupled equations results. The mode coupling induced by damping tends to exacerbate the problem of inaccuracy in higher frequency modes.

It is suggested that this approach will only be useful if a more appropriate set of basis functions can be identified, or if the ceramic tile was less directly coupled to the aluminium back plate.

4.4 Transient propagation in the ceramic foam/aluminium plate

None of the models developed so far can satisfactorily describe the transient propagation observed in the Cotronics foam/aluminium bonded plate described in Section 2 (see experimental results in Section 3.5). These results clearly indicate that the propagation time for laser-generated pulses from their source to sensors at a range of distances from

the source cannot be accounted for in terms of a single propagation velocity: it appears likely that the fastest energy packets that arrive at the sensors do not follow a direct path, and part of the path follows the plane of the aluminium plate.

Such a pulse propagation path would have significant implications for an optimal sensor layout, and particularly for estimation of the source location. However, the models developed so far are not capable of confirming the correctness of such a propagation path. This should not be taken to indicate that the problem is not tractable: we are confident that other approaches will be successful. A finite element model (e.g. Prosser *et al.*, 1999, Banerjee *et al.*, 2004, Gao *et al.*, 2006) and/or an approximate plate theory approach will be investigated in the near future.

5. Thermal measurements

5.1 Introduction

In order to characterise the ability of thermal sensors to detect damage to (or changes in) ceramic foam layers with or without aluminium backing, and to allow an estimation of the number and density of thermal sensors that may be suitable for a prototype tile that is to be integrated with the Concept Demonstrator, both the test tile described in Section 3.5.4 and a bare sheet of ceramic foam were used. A number of other pieces of ceramic foam were cut to lie on top of backed or un-backed tiles to vary the thickness of the insulating layer. This composite system was then exposed to a heat source, and temperatures on the aluminium surface were monitored. It is envisaged that the measurement of temperature in the future may be performed by an optical fibre system, but to simplify the gathering of initial thermal data, the use of thermocouples was thought to be more straightforward and easily implemented. The operation of the optical fibre system sent to CSIRO by staff at NASA Dryden will be described later.

5.2 Aluminium-backed test piece and experimental set-up

The geometry of the Al-backed test piece is shown in Figure 5.1, and the experimental arrangement for the measurement of temperature is shown in Figure 5.2. As noted above, the panel consisting of an aluminium sheet bonded to a plate of Cotronics foam used for acoustic measurements was used here, and supplemented with carefully cut pieces of ceramic foam to provide different thicknesses of insulating material between the heat source and the back of the aluminium sheet. One of the plates of foam had a through-hole cut in it, and a cylinder of foam was made to act as a closely fitting plug.
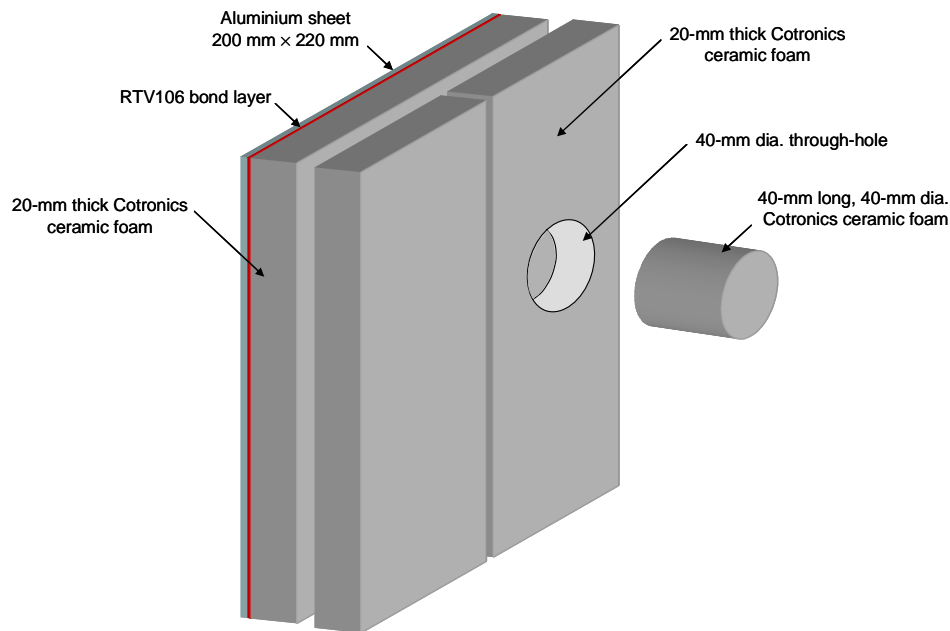

Figure 5.1. Ceramic foam bonded to aluminium sheet, and other fitted pieces of foam used to study thermal characteristics of insulated tiles.
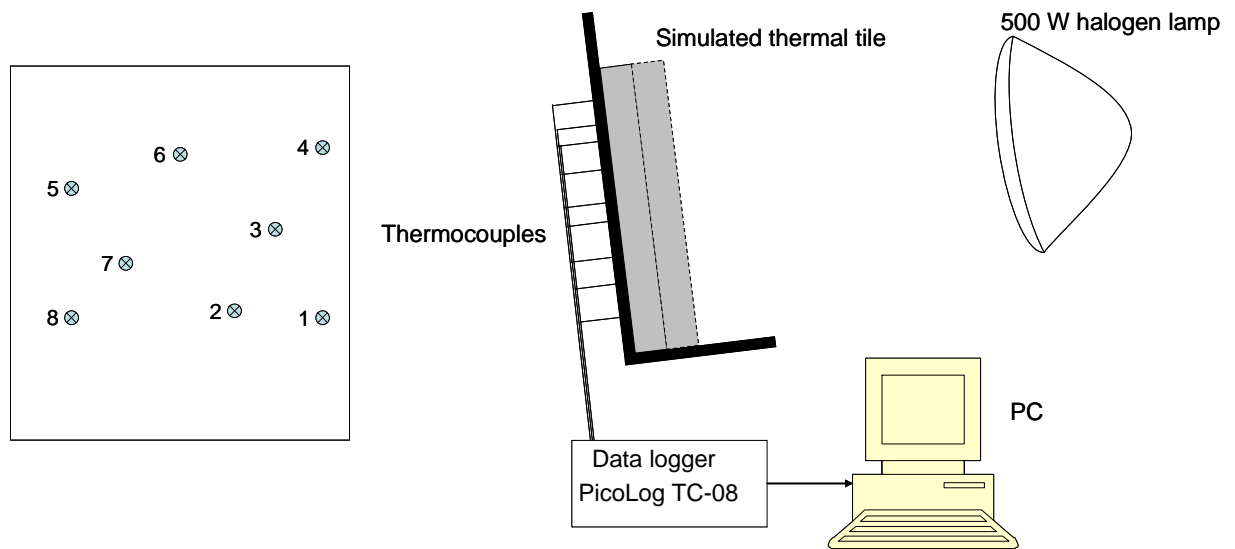
Figure 5.2. Experimental set-up for measuring temperatures. Left: arrangement of thermocouples on back of aluminium panel. Right: schematic of heating and data collection.

5.3 Results

Eight chromel-alumel thermocouples were attached (using thermal adhesive tape) to the back of the aluminium sheet to measure temperatures. They were positioned approximately equidistant from each other and distributed so as to monitor most of the area of the aluminium sheet (see Figure 5.2, left). These were connected to a data logger (PicoLab USB TC-08) and a personal computer to log temperatures as a function of time. The tile was held at a slight angle so that additional sheets could be rested against the bonded plate which rested on a thermally insulated holder to minimize heat transfer from the tile by conduction. A 500-W quartz halogen lamp was placed approximately 140 mm away from the front of the insulating plates (see Figure 5.2, right). This caused the measured temperatures to rise from 20 °C to about 45 °C.

It was found that regardless of the distribution of the additional pieces of ceramic foam, the thermocouples attached to the aluminium sheet all recorded the same temperature, regardless of the placement of any additional pieces of ceramic foam on the heated surface of the plate bonded to the aluminium. Figure 5.3 shows the results of two such experiments. The left hand graph shows the time-evolution of temperatures of the back of the aluminium when it was insulated from the irradiating lamp by the 20-mm thick sheet of ceramic bonded to it, and one half was further covered with the half-sized piece of foam with a hole in it (as seen in Figure 5.1). One of the thermocouples (number 7 in Figure 5.2, left) was directly in line with this hole, three others (numbers 5, 6 and 8) monitored the doubly-insulated half of the aluminium, the other four the singly-insulated half. The lamp was turned on at t = 100 s, and turned off at t = 3700 s. As can be seen, there is no significant difference between the recorded temperatures of any of the thermocouples.

On the right hand side of Figure 5.3 are the results of two experiments which simply tracked the temperatures when the aluminium was insulated with the one bonded layer of ceramic foam, and secondly when an additional 20-mm layer was added. The times at which the lamp was turned off and on are shown in the Figure. The rate of rise of temperature and the maximum temperature attained are, expectedly, lower when the aluminium is more insulated.

These results are consistent with the known thermal conductivities of the materials involved. Aluminium has a thermal conductivity of 180 W m^{-1} K^{-1}, the Cotronics foam 0.35 W m^{-1} K^{-1}, and the RTV106 silicone adhesive 0.21 W m^{-1} K^{-1}. As the thermal conductivity of aluminium is so much greater than that of the insulation, it maintains a uniform temperature independent of the spatial distribution of the low heat flux that propagates through the insulation.
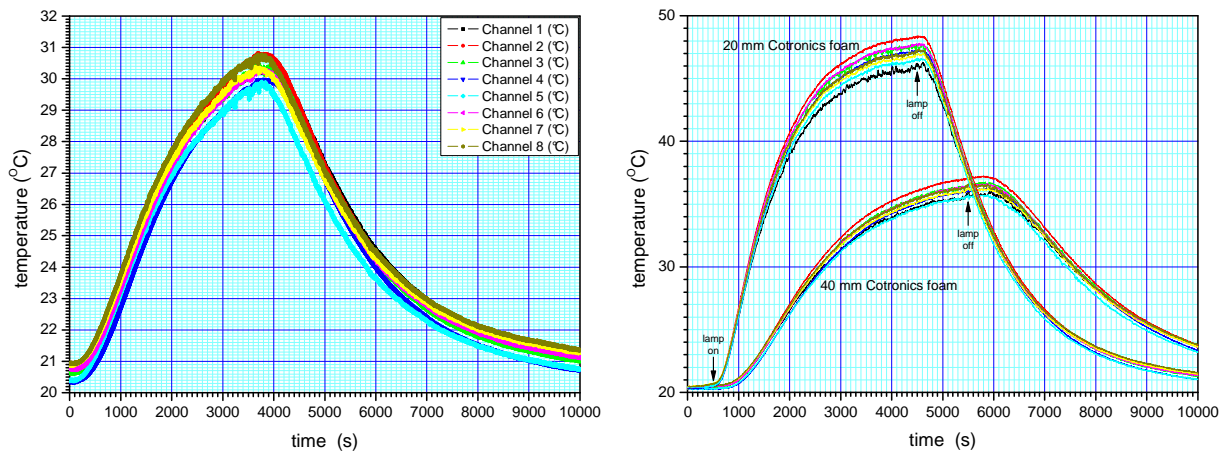

Figure 5.3. Left: Temperatures at different positions on the back of the aluminium sheet with varying thicknesses of insulation (see text). Right: Temperatures at different positions on the back of the aluminium sheet with either 20 mm of insulating material, or 40 mm.

Based on these results, a new piece of Cotronics ceramic foam was prepared, again 20 mm thick. This allowed the examination of temperature distributions without the presence of the aluminium sheet. Eight small (1.3 mm in diameter) holes were drilled 5 mm into the back face of the ceramic, and the eight thermocouples were inserted into these holes, held in place by the squeezed plastic coating of the thermocouples' wires. The positions of these thermocouples in relation to the added insulating pieces are shown in Figure 5.4. Superimposed on this Figure is a contour plot of the relative radiative output of the quartz halogen lamp used, the central region corresponding to a relative output of over 1.6 and contours are spaced at 0.4. This output was measured using a 2-mm diameter photometer to scan the top left quadrant of the source out to 120 mm from the centre vertically and horizontally at 10-mm intervals. The normalisation point (relative radiative output equal to 1) was set at 60 mm from the centre of this scan vertically and horizontally. It was assumed that the source was symmetric, so the scan was then reflected in the vertical and horizontal axes to the other quadrants.
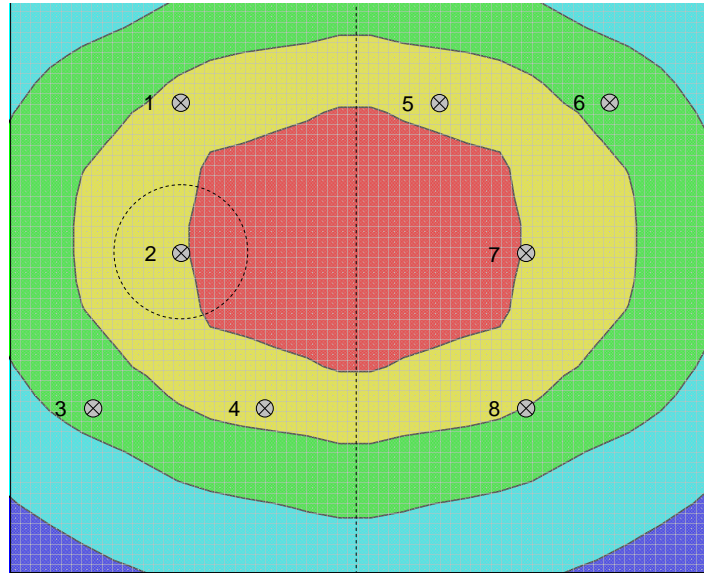
Figure 5.4. Arrangement of thermocouples embedded into ceramic foam, showing, with dashed lines, the outline of the 40mm dia. plug and the two halves of the additional ceramic foam pieces (see Figure 5.1). The radiative output of the illumination source is also shown (see text).
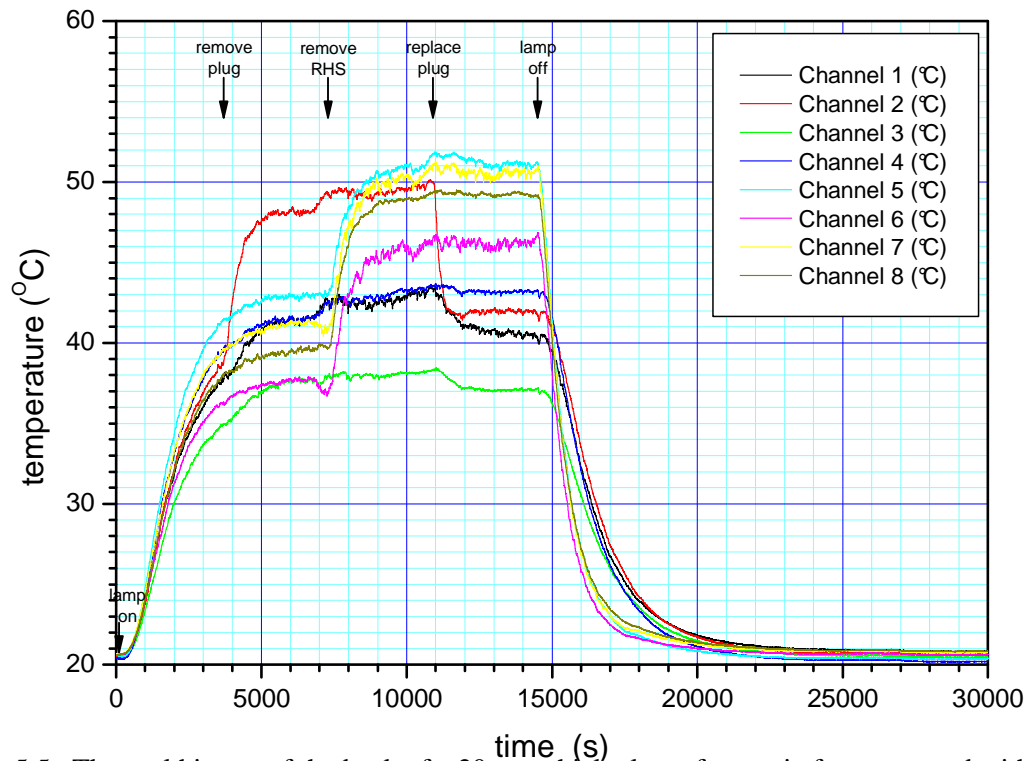
Figure 5.5. Thermal history of the back of a 20-mm thick plate of ceramic foam covered with additional pieces of foam (see Figure 5.1) exposed to a 500-W halogen lamp, showing the effect on the temperature distribution (see positions of thermocouples in Figure 5.4) after turning on the lamp, removal of the 40-mm plug, removal of the right-hand-side of extra insulation (exposing the side with thermocouples 5-8), replacing the plug, and finally turning off the lamp.

58

Although we have not yet verified these measurements with a computational model, the general features of the temperature history are consistent with the distribution of the heat source, the placement of the temperature sensors and the changes in the insulation described in the Figures.

Close examination of the recorded temperatures in Figure 5.5 indicated that the variation in measured temperatures between thermocouples that should have very similar outputs, given their position, were perhaps larger than expected. Compare, for example the outputs from thermocouples 5, 6, 7 and 8. While some variation might be expected from the non-uniform nature of the illumination, it was thought prudent to check the variations in output as a function of temperature as the 20-mm block alone was heated. These outputs were compared with the outputs of the same thermocouples immersed in a bath of water and heated gently. The latter set-up showed only a slight linear increase in the range of temperatures recorded by the thermocouples (about 0.3 Celsius degrees over a 30 degree range), while the former indicated a much larger range, fully 1 Celsius degree over a range of 15 degrees. This wider range is thought to be due to variations in the thermal contact of the small tips of the thermocouples with the ceramic foam when pressed into the small holes drilled to hold them.

5.4 Conclusions from thermocouple measurements

These results have clear implications for the placement of thermal sensors – whether they be thermocouples or optical fibres – on thermally insulated metallic tiles. In any structure that has insulation bonded directly onto a metal, or otherwise highly thermally conductive sheet, only one thermal sensor per panel (i.e. an entity that is thermally insulated from its neighbours) may be necessary, depending on the size of the sheet and the relative thermal conductivities of the insulator and metal. The rate of rise and final temperature of the metal substrate may be used to estimate the minimum thickness of insulation (with appropriate modelling), but no indication of the location of the thinnest area would be gained. If the insulation is less directly connected to the substrate, were stand-offs to be used for instance, the thermal conductivities of each member of the structure would need to be considered.

If only the temperature of the underlying structural metal is important, temperature sensors on the metal only would need to be used. In the present incarnation of the thermal tile, however, it is clear that to have any ability to locate damaged insulation through measuring temperature, thermal sensors would need to be placed in contact with the insulating material. Embedding sensors in the bond line may not ensure accurate measurements of the temperature of either the ceramic foam or the aluminium substrate: the adhesive used here had a nominal thermal conductivity lower than that of the ceramic foam. One possibility, if optical fibres were to be used as the temperature sensor, would be to sandwich the fibre between layers of the insulator, and use an adhesive which had a thermal conductivity very close to that of the insulator to bond both fibre and insulator. Alternatively, the thermal sensors may be bonded with thermally conducting adhesive to the back of the ceramic foam, and then an RTV bond layer could be applied over this for bonding to the metal substrate.

We have demonstrated that with the present materials changes in the thickness of the insulator of 50% are easily detectable with thermocouples embedded in the ceramic

foam. The removal of small amounts of insulation can be detected not only by sensors immediately behind the 'divot', but also by sensors that are several centimetres away. Clearly the number of thermal sensors per unit area required to determine damage severity and location depends on the minimum size of the damage one wishes to detect, the material properties and structures used, and whether or not thermal measurements are the primary or secondary (to acoustic detection of an impact for example) method to determine damage location. If the materials and basic design of an aluminium substrate with a bonded insulating layer employed in the present work were used for a future 'sensored' tile, and damage of the order of cubic centimetres were to be detectable, the maximum distance between thermal sensors should be about 70 mm. From the work described in Section 3.5 a similar spacing of acoustic sensors would be appropriate for locating the impact site.

5.5 Optical fibre system from NASA Dryden

The equipment developed by staff at NASA Dryden to operate a fibre-optic detection system was delivered to CSIRO in mid-July. This system uses optical frequency domain reflectometry to interrogate a length of optical fibre along which Bragg gratings have been written. Changes in the spacing of the gratings (either by mechanical strain or by temperature increases causing thermal expansion) are measured by measuring the change in the wavelength at which each grating has its maximum reflectance. All the gratings are written at the same central wavelength, and their positions along the fibre are detected by measuring the beat frequency of any individual grating's reflection with the reflection from a reference reflector – the laser wavelength (and therefore frequency) is scanned, and so the time taken for light to travel from the reference reflector and the grating is small, but finite, and in this time the wavelength of the probe radiation changes slightly causing an interferogram, the frequency components of which will be linearly related to the distance along the fibre of the grating reflector.

This technique has been described elsewhere (NASA Dryden, 2006), and its principle of operation was first proposed in 1981 (Eickhoff and Ulrich, 1981) and developed further, notably by Brinkmeyer's group (Barfuss and Brinkmeyer, 1989, Glombitza and Brinkmeyer, 1993) and at NASA Langley Research Center (Froggatt, 1996, Froggatt and Moore, 1998a and 1998b, Childers *et al.*, 2001). The advantage of the developments made at NASA Dryden is that the fibre may be interrogated at tens of Hertz, whereas conventional and present commercial OFDR systems are restricted to operation at about 0.2 Hertz, interrogating the fibre only once every five seconds. The high interrogation rate of the Dryden method, two orders of magnitude faster, allows the rapid tracking of thermal and strain changes.

At CSIRO a test fibre has been fabricated from the unwritten 125-μm single-mode fibre and a two-metre length of draw-tower-written Bragg grating fibre (called the distributed strain sensing (DSS) fibre) containing 206 gratings. The gratings are 5 mm in length, and are spaced at 10-mm intervals. This test fibre has been taped to a flat carbon-fibre test piece in order to study both how the system is operated, its principle of measurement, and how temperature and strain manifest themselves in the measured signals. With the help of staff at NASA Dryden, in particular Allen Parker, we have come to understand the system, and operate it effectively, and hope now to be able to discuss how it may be incorporated into a thermal tile for the measurement of temperature.

In this report our aim is not to describe in any detail the operation or application of this fibre-optic technology; staff at NASA have much more experience of these systems. Here we present just a few pictures demonstrating the operation of NASA's system in both modes, using the 'Langley' and 'Dryden' methods of processing data from the fibre as it was subjected to localized strain and localised heating.

Figure 5.6 shows a photograph of the layout of the DSS fibre used to familiarize ourselves with the operation of the OFDR system. A short length of optical fibre, with an FC angle-polished connector on one end, was fusion-spliced onto a 4-metre length of fibre supplied by NASA which contained a broadband reflector (5%) half way along its length. This was then fusion-spliced onto a 2-m length of DSS fibre. The fibre was then laid out in a serpentine pattern with all the radii of curvature kept above about 50 mm to minimize bend-radius losses. The white spots marked on

Figure 5.6. Layout of the optical fibres used in the test set-up to learn the operation of the OFDR system.

the backing (see Figure 5.6) denoted 100-mm intervals along the length of the fibre, allowing easy estimation of position along the fibre.

Figures 5.7 to 5.10 show screen dumps of the system in operation. Figure 5.7 shows the system operating in the 'Langley' mode, showing the interferogram or 'raw data' in the top trace (reflected signal as a function of wavelength), and the Fourier transform of this data in the lower trace. In this and subsequent results the laser was scanned, nominally from 1542 nm to 1543 nm, but due to firmware in the system the wavelength range

displayed in the top traces is from 1542 nm to 1550 nm. The DSS fibre gratings are nominally written at the wavelength of 1546 nm. The lower frame in the right-hand part of the Figure is an expanded view of the spectrum showing the beginning of the DSS.

Figure 5.8 shows the system working in the 'Dryden' mode, where the strain as a function of position along the length of the DSS fibre is displayed in the top half of the screen, the left screen showing an 'unstrained' condition, the right showing the result of applying pressure near the beginning of the fibre. Figure 5.9 shows strain versus position along the fibre (left-hand panels), and the strain as measured at all positions as a function of time (right-hand panels). The left screen of the Figure shows a single fibre reacting to an applied pressure. The right screen shows several gratings reacting to applied pressure. Note the rapid reversion to the zero strain state on release of the applied pressure.

In Figure 5.10 the left hand screen image shows the operation of the system in the 'Dryden' mode when a section of the DSS fibre is heated with a hot-air gun. In contrast to the rapid application and release of local pressure on the fibre, the temperature shows a slow rise, and a similarly slow fall after the heat source is removed. The right-hand side shows a similar application and removal of heat, but this time measured using the 'Langley' mode. Note that in this mode the horizontal axis in the strain versus position plot is now specific grating number rather than just position along the fibre, as is the case using the 'Dryden' method. This is because in the Dryden method the interferogram is analysed in sequential 2k segments of data (time intervals); each segment of data may contain information about one or two gratings, giving information about a specific section of the fibre rather than a specific grating.

The problem of distinguishing strain from temperature effects on the fibre Bragg gratings' output is one question that must be addressed. Conventional methods of eliminating the temperature sensitivity by holding those lengths of fibre that contain a grating in a pre-tensioned rig seem unlikely to be easily implemented. However, a modification of this idea where the fibre is laid in tension and held in place using a bonding agent that has the appropriate thermal expansion properties to exactly compensate for temperature changes is possible. The use of two fibres, one temperature-compensated and one not, running side-by-side may be a way of separating these two effects.

It seems unlikely that the fibre-optic system can be used for impact detection as it runs at only a few tens of Hertz, and high speed impacts on tiles of this size and type cause vibrations up to a few megahertz, and reverberations last for milliseconds.
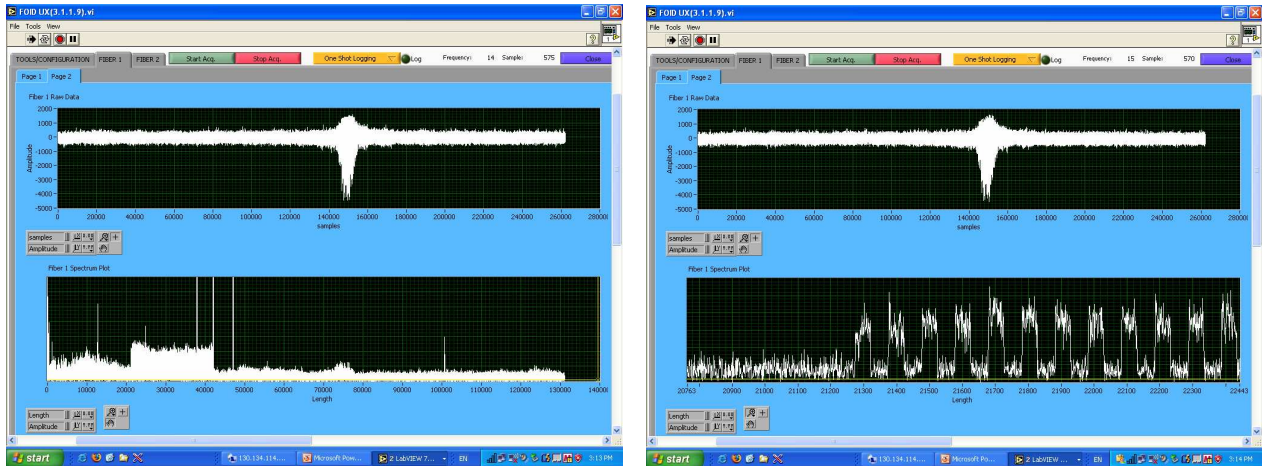
Figure 5.7. Screen dumps of operation of the optical fibre operating in the 'Langley' mode, showing the interferogram or 'raw data' in the top trace (reflected signal as a function of wavelength), and the Fourier transform of this data in the lower trace. The right-hand frame is an expanded view of the spectrum near the beginning of the DSS.
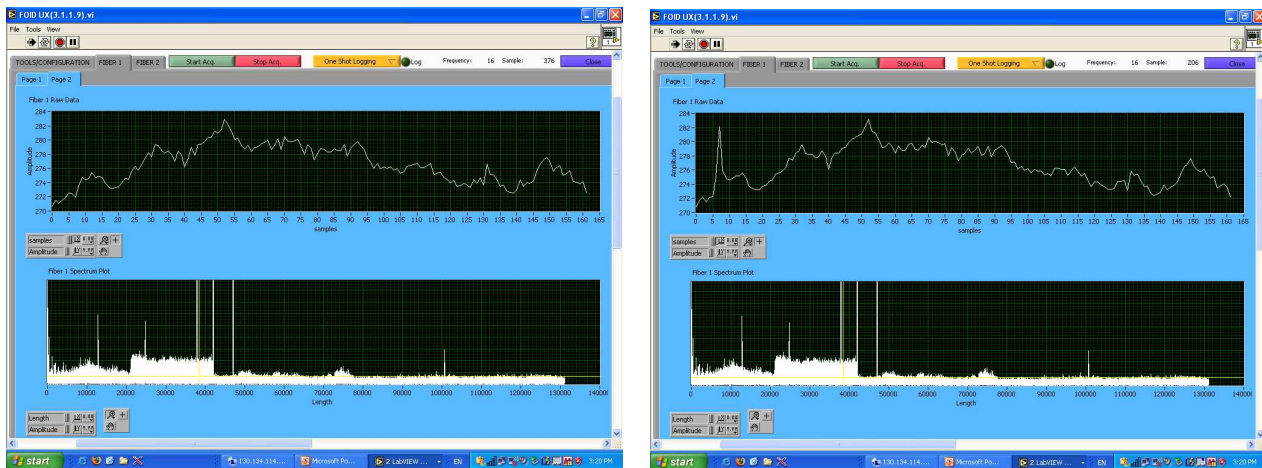

Figure 5.8. Screen dumps showing operation of the system in the 'Dryden' mode, showing the strain as a function of position along the length of the DSS fibre, the left screen showing an 'unstrained' condition, the right showing the result of applying pressure near the beginning of the fibre.
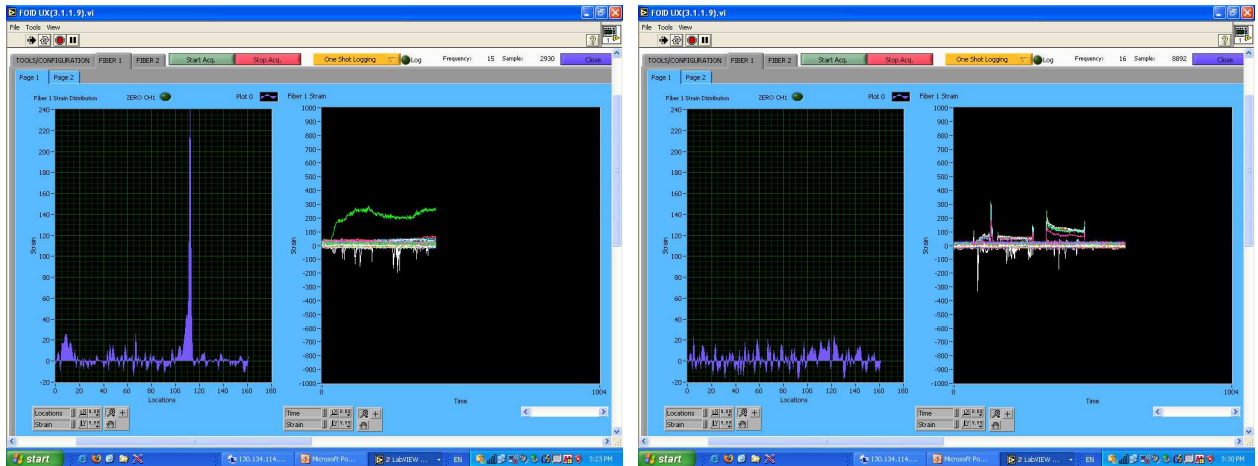
Figure 5.9. Views of the strain versus position along the fibre (left-hand panels), and the strain as measured at all positions as a function of time (right-hand panels). The left screen shot shows a single fibre reacting to an applied pressure. The right screen dump shows several gratings reacting to applied pressure. Note the rapid reversion to the zero strain state on release of the applied pressure.
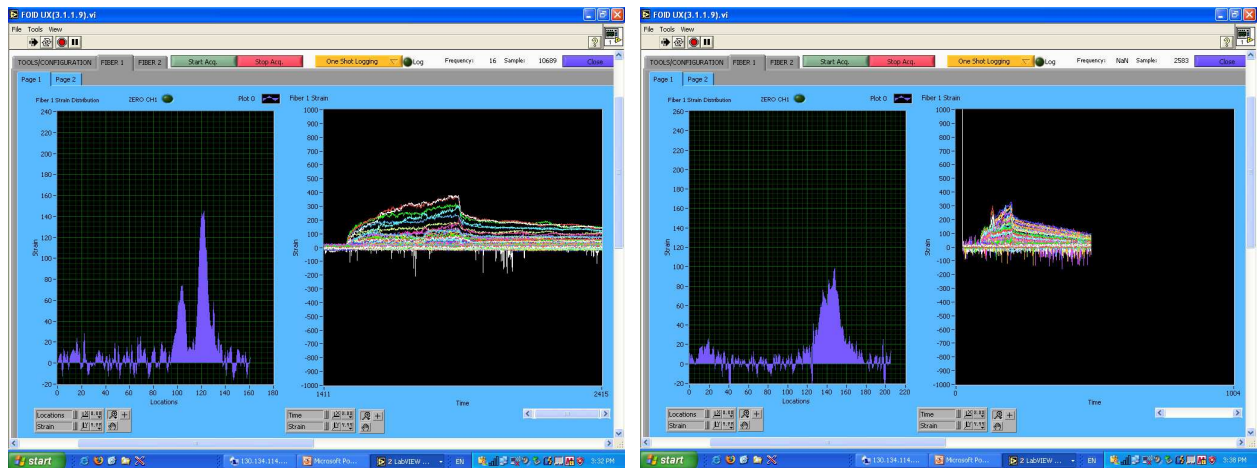
Figure 5.10. Left-hand screen dump shows the operation of the system in the 'Dryden' mode when a section of the DSS fibre is heated with a hot-air gun. Note the slow temperature rise, and similarly slow fall after the heat source is removed. The right-hand side shows a similar application and removal of heat, but this time measured using the 'Langley' method. Note that the horizontal axis in the strain versus position plot is now specific grating number rather than just position along the fibre.

As far as mounting a fibre in an insulating tile, the use of the robust draw-tower fibres that NASA has used facilitates a solution. Fibres that have been conventionally written – where each grating has to be written after fibre manufacture, requiring stripping the coating for the writing process and then re-coating, making the fibre inherently weak – would be much more difficult to mount in this environment. Draw-tower fibres may be bent into fairly tight radii, and while this does increase the losses and therefore reduces the signal-to-noise ratio of the measured signals, their physical strength remains an advantage.

6. Integration with CD architecture

This section outlines principles by which a TPS health monitoring system based on acoustic emission and thermal measurements can be integrated into the multi-agent system architecture of the existing CSIRO/NASA Concept Demonstrator (CD) (Batten *et al.*, 2006).

Development of these principles is not trivial. The fundamental architectural unit of the CD is a local sensing agent, which uses local sensors to obtain information about the state of the structure in its local region. On the other hand, one of the principal advantages of an optical fibre Bragg grating (FBG) sensor system is that a single fibre can contain many (up to several thousand) sensors, distributed over a large region of the structure, all of which can be interrogated at a single point that may be remote from the locations of the sensors. This allows large areas of structure to be sensed from a central location, and the need for only a single laser and data acquisition and analysis system reduces the overhead cost and weight, and system complexity. A major disadvantage of such networks is their vulnerability to fibre breakage. The single laser/data acquisition system also represents a single point of failure.

At first sight the use of a large-area, distributed fibre sensing system appears incompatible with a local sensing agent architecture. However, a novel FBG network architecture is proposed here that is consistent with the CD's local agent architecture, and which should result in a network with greatly enhanced robustness to fibre damage. It must be pointed out that this architecture has not yet been tested nor analysed in any detail. It is proposed for further evaluation and testing in the next phase of the project.

6.1 Overview of the CD architecture

The current development of the CD is described in Batten *et al.* (2006) and Hoschke *et al.* (2007) and references contained therein. Its purpose is to detect impacts on the external skin of the structure (a hexagonal prism) and to evaluate any resulting damage. The basic architecture of the CD is a square array of autonomous agents, in which each can communicate directly with its four nearest neighbours. This network of agents is embedded in the structure.

Each local agent has a group of piezoelectric sensors, bonded to the inner surface of the skin, whose primary role is to detect the elastic waves generated by impacts on the surface of the structure. The agent analyses the data from these sensors and decides whether it has suffered an impact, and the approximate location and severity of the impact. Communications within the network of agents can establish the spatial extent of a damaged region, the number of impact sites, and can dynamically form a minimum spanning tree connecting multiple impact sites by the shortest paths (see Figure 6.1). The algorithm that performs this last function is based on ant colony optimisation (ACO) (Prokopenko *et al.*, 2005, Dorigo and Di Caro, 1999, Dorigo and Stützle, 2004): it simulates, using information packets that are communicated around the network, the way in which ants forage for food and form shortest paths between food sources and their nests. The paths are marked by a 'pheromone' trail, left by ants to guide other ants.

The CD also contains an additional agent, in the form of a mobile robot that can move around on the surface of the structure, communicating with the agents embedded in the surface at its current location. The purpose of this robot is to act as a mobile damage inspector, for which it carries additional sensors (currently a video camera), and later a repair agent. It is envisaged to eventually be one of a swarm of small robots, but there is currently only one and it is relatively large.
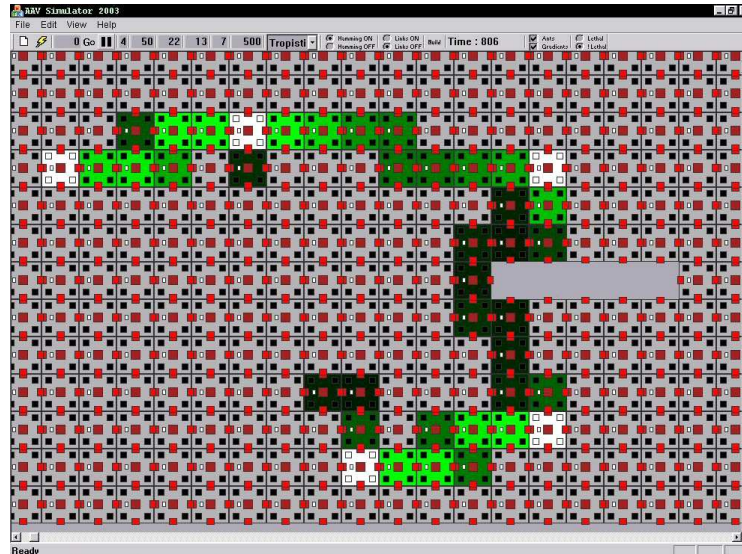

Figure 6.1: Computer simulation of a reconfigurable, self-organised impact network produced by the decentralised ACO algorithm. Individual agents (cells) are represented by the (~5 mm) grey squares that contain black (sensors), red (communications connectors) and brown (processor) components. White cells are those that have received a sub-critical impact. Green cells are those that have a pheromone level greater than a threshold value, with lighter shades indicating a higher concentration. The plain grey region represents agents that are not present or not functional for some reason, and the pheromone path skirts around this region. Abbott *et al.* (2003b) contains further details.

The robot communicates with the embedded agents using acoustic signals transmitted through the aluminium skin of the CD. It navigates according to information received from the embedded agents. In principle it could follow the minimum spanning tree formed by the ACO algorithm (Figure 6.1), to move from one impact site to another by the shortest path. In practice another local algorithm, based on the establishment of gradient fields, is used to guide the robot to damage sites (Batten *et al.* 2006, Hoschke *et al.* 2007), but the shortest path network produced by the distributed ACO algorithm provides an appealing conceptual picture of the robot guidance principle.

The important points to recognise here are, firstly, that the whole system of agents, including both embedded and mobile agents, operate by self-organisation (i.e. as a result of the interactions between them) with no central control, and, secondly, that each of the agents has information only about its immediate vicinity: none of the agents has a global view of the structure or its state. The robot (mobile agent) acts as a secondary inspector, in the sense that it travels to locations where an impact has been detected by the acoustic emission sensors, and obtains additional information about the level of damage that has occurred.

6.2 Proposed FBG network architecture

In the proposed architecture, the FBG network will play a role analogous to that of the mobile agent in the current system, i.e. that of a secondary inspector. When an impact has been detected by the acoustic emission sensors, thermal measurements will be carried out in the region near the impact site. In the present case, the additional information provided by the thermal measurements relates directly to the fitness-for-purpose of the TPS structure. Of course, in both cases, there is no reason why the secondary inspector cannot carry out a general scan of the structure without an impact having been detected, but this discussion will focus on the case of detected impacts.

The proposed FBG network architecture is a locally-switchable multi-sector model with a high degree of redundancy and reconfigurability to enhance its survivability in the presence of damage. It is a two-dimensional generalisation of the 1D networks proposed recently by Wei and Sun (2006, 2007). The basic sensing module on each tile, and which is controlled by a local agent, is a ring as shown schematically in Figure 6.2. The purpose of the ring is to provide multiple paths to each sensor, to enhance the survivability of the network in the event of damage to links or individual sensors. The actual layout of the fibre on each tile need not be circular, of course, but the nodes, which are electrically-controlled optical switches, connect this local ring to the network.
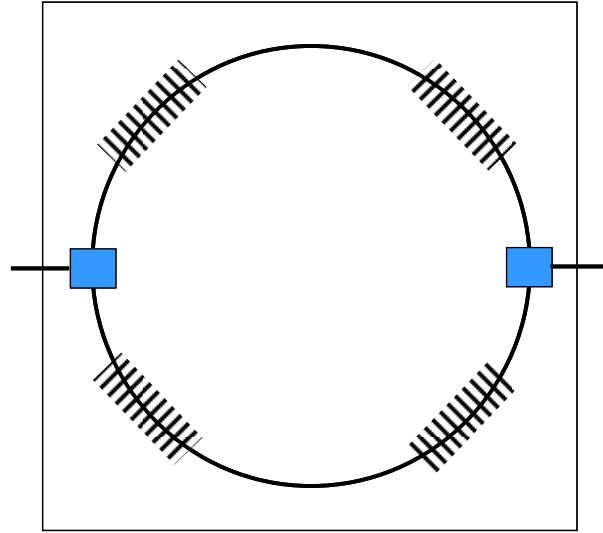

Figure 6.2: Schematic diagram of a ring FBG sensor module on a TPS tile. The outer square box represents the tile, the circular segments represent the optical fibre, and the small blue boxes are nodes, with short lengths of fibre to connect the ring element to the network. The Bragg grating sensors are represented by the cross-hatching on the fibre segments. The nodes are electrically-controlled optical switches that may direct light around the ring, or to or from connecting links in the network. The tile is shown as being square, and the fibre layout circular, with two Bragg grating elements per segment, but none of these are necessary constraints.

Each of the sensing modules such as that shown in Figure 6.2 is associated with a local agent. This agent controls the setting of the switches: the local agents therefore control the routes through which light propagates through the network.

Figure 6.3 shows six tiles connected to form a 3x2 array. The green node, a multi-way switch, directs laser light into the array at any one of a number of nodes, and back out again to the data acquisition system. In principle, a number of lasers and data acquisition systems could be provided for redundancy, and these could be switched into the array at various points to further reduce the vulnerability of the system to failure of these essential components.
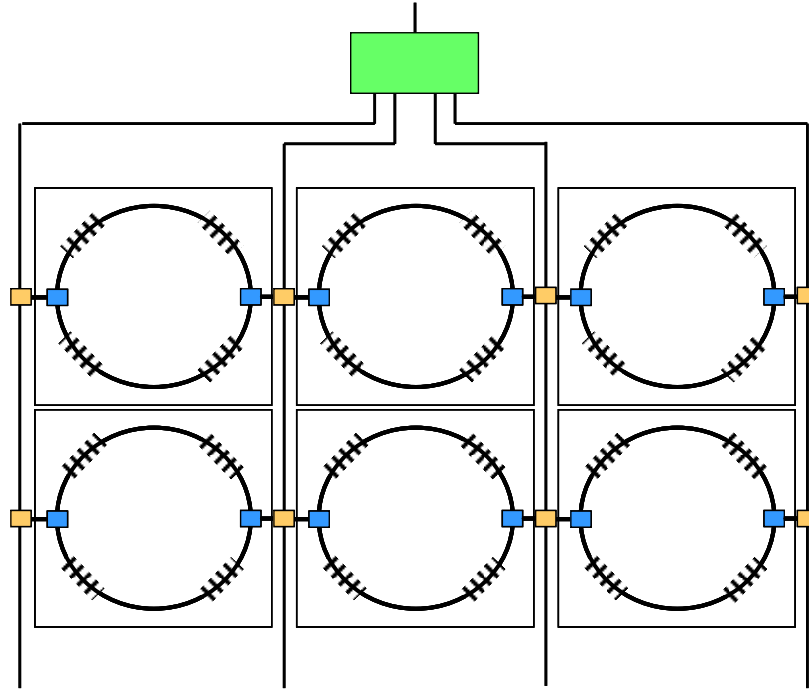

Figure 6.3: Six ring modules of the form shown in Figure 6.2, connected to form a 3x2 array. The green node, external to the network, represents a multi-way switch that can direct laser light into the array and back out to the data acquisition system. The orange nodes are 3-way optical switches that can direct light to either adjoining ring or along the connecting fibre.

The orange nodes in Figure 6.3 are the entrance nodes of Wei and Sun (2006). They are switches that direct light between the network links and the sensing modules. It is envisaged that these entrance nodes would also be controlled by the local agents, with a local algorithm to be developed to determine their states.

It can be seen from Figure 6.3 that light can be directed along many different routes to get to any particular tile or sensing module in the network, and that the route is determined by the switching of the blue and orange nodes, which in turn are controlled by the embedded local agents of the system. Thus, the operation of this secondary inspector is controlled by the local agents, as is the case for the mobile agent in the current CD (Batten *et al.*, 2006).

A more densely interconnected version of this network, with greater redundancy of links, can also be envisaged. Linking fibres could cross the array horizontally, and connect into additional nodes in each ring module.

This architecture requires further investigation and evaluation to prove its utility. However, it provides a secondary inspection protocol that is closely analogous to that provided by the existing mobile agent. In the latter case the agent itself moves around the structure using a 'roadmap' defined using a self-organising algorithm by the agents embedded in the structure. In the former case it is the light that interrogates the sensors that is guided around the structure by the agents.

Within this operating protocol there is no immediate need for fusion of the acoustic emission and thermal data, since the information obtained from the primary (acoustic emission) and secondary (thermal) sensors are used separately. Later in the program, if further characterisation of the damage is required, there may be some advantage in utilising information obtained from the two sets of sensors, but the immediate concern is evaluating the fitness-for-purpose, and this will be achieved from the thermal data.

6.3 Sensor layouts

This project provided the stimulus for the initiation of a fundamental study of the design of optimal sensor layouts from an information-theoretic perspective. This work is still in its early stages, but a brief outline of the approach will be given here.

There have been many approaches to the determination of optimal sensor layouts, both for structural health monitoring (SHM) and for more general sensing problems. Traditional engineering approaches (e.g. Staszewski *et al*., 2000, Lee and Staszewski, 2007, and references cited therein) are based on physical models of the damage and its effect on a specific sensor type. This is essentially the approach we will take in the short term for the design of a TPS test piece, but it is somewhat limited to the use of specific sensors in known situations, and determination of the optimality or otherwise of a layout is difficult and relies on task-specific criteria. The use of a Bayesian statistical approach to selecting sensor locations was introduced by Cameron and Durrant-Whyte (1990). Trendafilova *et al*. (2000) used the concept of average mutual information between sensors to determine the optimal distance between measurement points. Guestrin *et al*. (2005) also employed a mutual information criterion, for the case where the uncertainty of a measurement can be described by a Gaussian model.

In contrast with traditional engineered sensing systems, biological systems are not built out of separately-designed parts attached together at a later stage - they evolve symbiotically. Each component co-evolves with other components to produce a dynamic system in which components can be used for multiple purposes and can take on multiple roles, thus increasing robustness and adaptability to unknown situations (Miller *et al*., 2000). Typically, evolutionary design may employ genetic algorithms in evolving optimal strategies that satisfy given fitness functions, by exploring large and complicated search-space landscapes. However, evolutionary design may be approached in two ways: via task-specific objectives (e.g. Staszewski *et al*., 2000) or via generic intrinsic selection criteria (Prokopenko *et al*. 2006). The latter method, information-driven evolutionary design, essentially focuses on information transfer within specific channels.

Polani and coworkers (e.g. Klyubin *et al*., 2004, Nehaniv *et al*., 2005) have been developing an approach to sensory evolution in which they have found that pushing the information flow to the information-theoretic limit (i.e. maximization of information

transfer) provides a mechanism for optimising organism-specific meaningful information, and can ultimately be responsible for adaptively reshaping the system. They consider the benefits and costs of particular sources of information, and introduce a fitness measure that contains weighted terms for redundancy and novelty (Olsson *et al.*, 2004) to study the trade-off between similarity of information (redundancy) and novelty of information between groups of sensors. Such a trade-off is likely to be highly relevant in the SHM environment.

The aim of our work is to extend the evolutionary approach to optimal sensor layout of Polani's group, in the context of damage monitoring, to incorporate Bayesian inference of diagnosis (and ultimately prognosis) from sensor data, and to consider cases in which damage information is obtained either directly or indirectly from sensor information. A paper outlining the approach to this is in preparation. This work is being carried out in collaboration with Dr Mikhail Prokopenko (CSIRO ICT Centre) and Mr George Mathews (University of Sydney and CMSE).

7. Test-piece design

While much of the information required to design a test-piece for integration onto the CSIRO/NASA Concept Demonstrator has been obtained in the work reported here, it is equally clear that there are a number of significant questions that must be answered before the required specifications can be finalised. Furthermore, the answers to these questions require discussion and input from NASA, so we at CSIRO are not yet in a position to complete the test-piece design.

The major questions that require resolution are as follows.

1. *What ceramic foam material should be used for the primary thermal protection function?*
   Extensive acoustic measurements have been carried out on two commercial ceramic foam materials that could be used as substitutes for the actual shuttle tile material that has proved to be very difficult to obtain. The Cotronics 310 material was essentially elastically isotropic, but the samples we obtained contained both large voids up to tens of millimetres in size (Section 2.2) and hard, glassy inclusions, making the material highly inhomogeneous. Consequently, acoustic transmission through this material is spatially variable, and depends on the particular propagation path.

   The Zircar Ceramics ZAL-45 foam was apparently far more homogeneous than the Cotronics, but it was also highly anisotropic, exhibiting strong anisotropy in both the propagation velocities and attenuations. This anisotropy would produce significant complexities for estimation of the locations of impacts in a test-piece.

   Rather than use a material that is likely to introduce greater complexities into system operation than the 'real' materials, it would be preferable to use a material with either comparable or reduced complexity. Thus, unless the ceramic foams used in practical thermal protection systems have significantly anisotropic elastic properties, it would seem preferable for the test-piece to utilise an isotropic, relatively homogeneous material.

   No systematic measurements of thermal properties of these materials were undertaken, but it is likely that thermal propagation will be similarly influenced by the material structure.

   Jointly with NASA, we would like to identify and obtain an appropriate ceramic foam material.

2. *How should the primary TPS material be attached to the substrate, and what substrate should be used?*
   It was noted in Sections 3 and 5 that for sensors in the vicinity of the metallic substrate both the elastic and thermal propagation are strongly influenced by the presence of the metal layer. The thermal measurements were most seriously affected by the highly conducting aluminium substrate: both the sensitivity and spatial resolution of damage detection by thermal measurements will be

compromised by proximity (and not necessarily direct contact) of the thermal sensors to the substrate. Acoustic propagation measurements are also influenced by bonding of the relatively stiff aluminium to the ceramic foam, but in this case it is an advantageous influence.

We at CSIRO have no knowledge of the structural variations of thermal protection systems that might be considered for future vehicles, nor are we aware of whether TPS designs are likely to be influenced by health monitoring considerations, but there are (at least) three approaches to mitigating the thermal measurement issues identified.

    a. Continue to bond the ceramic to a metallic substrate, but embed the thermal sensors within the ceramic tile. This could be done by embedding during material fabrication (i.e. prior to firing), by slicing and re-bonding the ceramic, or by use of a thick, composite bond layer. This would retain the acoustic benefits of the bonded structure.

    b. Mount the ceramic tiles on stand-offs from the substrate, i.e. use an air/vacuum insulating gap between the ceramic and substrate. This would lose the acoustic benefits of the bonded substrate, and may require the use of acoustic sensors at higher spatial density.

    c. Employ a non-metallic substrate, such as a ceramic, glass or composite material, to which the ceramic is bonded. This would overcome the problem produced by the high thermal conductivity of the metallic substrate, without removing the acoustic benefits of the stiff, low-attenuation aluminium.

Discussion of TPS design issues such as these with NASA personnel would be useful.

3. *How should the optical fibre Bragg grating (FBG) network be implemented?*
A broad proposal for the architecture of the FBG network was presented in Section 6. This proposal not only requires further detailed consideration with regard to both operation and implementation, but there is a need to discuss its implications with NASA personnel. The proposal needs further investigation and development before it could be included in a test-piece design.

In order to address these questions, it would be desirable to hold a face-to-face meeting/workshop between CSIRO and appropriate NASA staff, either in Sydney or at the NASA Dryden or Langley facilities, at the earliest opportunity.

8. Summary and conclusions

The principal objective of this work was to characterise materials and specify methods to a stage that would culminate in the design of a test-piece for use, with the CSIRO/NASA structural health monitoring concept demonstrator (CD), in subsequent phases of the project. While a considerable proportion of this work has been carried out, the ultimate aim of designing a test-piece has not been achieved, largely because the material measurements raised serious concerns about the use of those materials in a demonstration structure. Resolution of these concerns, summarised in Section 7, require discussion and consultation with NASA, and it is recommended that a CSIRO/NASA face-to-face meeting/workshop be convened at an early opportunity to resolve them.

Extensive measurements were made of the acoustic properties of two commercial ceramic foam materials, Cotronics 310 and Zircar Ceramics ZAL-45 foam, but neither was found to be particularly satisfactory for use as a 'model' demonstrator material. Measurements of acoustic velocities and attenuations were made in the frequency range 0.2 to 1.0 MHz, above which the attenuations were generally too high to make sensible measurements. The Cotronics material was found to be effectively isotropic, but strongly inhomogeneous due to the presence of large (up to tens of millimetres) voids, and hard, glassy inclusions. The Zircar foam did not contain such coarse inhomogeneities, but its elastic properties were highly anisotropic. Such anisotropy would severely complicate the use of impact-generated acoustic signals for location of the impact site.

Development of acoustic models of the materials and structures of interest was begun, based on guided wave calculations in infinite plates and on the modal resonance method. Further development of these models, particularly in the capability to model transient disturbances is required, and is under way. Development of a dynamic finite element model is planned to begin in the near future.

Thermal measurements were made using thermocouples, on ceramic tiles, and on tiles bonded to an aluminium substrate. Not surprisingly, it was shown that temperature measurements on the metallic substrate lost all spatial information carried by the heat flow through the ceramic. Information about the spatial extent of the damage can be obtained if the thermal sensors are well-insulated from the substrate, and some suggestions for doing this were made.

A thermal sensor system based on optical frequency domain reflectivity measurements in a fibre Bragg grating array, supplied by NASA Dryden FRC, was set up and demonstrated. It is now ready for incorporation into a test article. A novel scheme was presented for integration of a FBG thermal sensing network into the CSIRO/NASA CD architecture. This requires further evaluation, but it has the potential to provide a robust and efficient fibre sensing network.

9. Acknowledgements

10. References

Abbott, D., Ables, J., Batten, A., Carpenter, D. C., Collings, A. F., Doyle, B., Dunlop, J. B.,Edwards, Farmer, A. J., Gaffney, B., Hedley, M., Isaacs, P., Johnson, M. E., Joshi, B., Lewis, C. J., Poulton, G. T., Price, D. C., Prokopenko, M., Reda, T., Rees, D. E., Scott, D. A., Seneviratne, S., Valencia, P., Wang, P., Whitnall, D. F., Winter, J. (2003a) "Development and Evaluation of Sensor Concepts for Ageless Aerospace Vehicles. Report 3: Phase 1 Implementation of the Concept Demonstrator", CSIRO Telecommunications and Industrial Physics. Report No. TIPP 1628. January 2003.

Abbott, D., Batten, A., Carpenter, D. C., Dunlop, J. B., Edwards, G. C., Farmer, A. J., Gaffney, B., Hedley, M., Hoschke, N., Isaacs, P., Johnson, M. E., Lewis, C. J., Murdoch, A., Poulton, G. T., Price, D. C., Prokopenko, M., Rees, D. E., Scott, D. A., Seneviratne, S., Valencia, P., Wang, P., Whitnall, D. F. (2003b) "Development and Evaluation of Sensor Concepts for Ageless Aerospace Vehicles. Report 4: Phase 1 Implementation of the Concept Demonstrator", CSIRO Telecommunications and Industrial Physics. Report No. TIPP 1898. September 2003.

Abbott, D., Cunningham, S., Daniels, G., Doyle, B., Dunlop, J., Economou, D., Farmer, A., Farrant, D., Foley, C., Fox, B., Hedley, M., Herrmann, J., Jacka, C., James, G., Johnson, M., Martin, B., Poulton, G., Price, D., Reda, T., Rosolen, G., Scott, A., Valencia, P., Ward, D., Winter, J., Young, A. (2001) "Development and Evaluation of Sensor Concepts for Ageless Aerospace Vehicles, Report 1", CSIRO Telecommunications and Industrial Physics. Report No. TIPP 1516, 2001. Also published as NASA Technical Report no. NASA/CR-2002-211772, at http://techreports.larc.nasa.gov/ltrs/PDF/2002/cr/NASA-2002-cr211772.pdf

Abbott, D., Doyle, B., Dunlop, J., Farmer, A., Hedley, M., Herrmann, J., James, G., Johnson, M., Joshi, B., Poulton, G., Price, D., Prokopenko, M., Reda, T., Rees, D., Scott, A., Valencia, P., Ward, D., Winter J. (2002) "Development and Evaluation of Sensor Concepts for Ageless Aerospace Vehicles. Development of Concepts for an Intelligent Sensing System. Report 2", CSIRO Telecommunications and Industrial Physics. Report No. TIPP 1517. May 2002. Also published as NASA technical report NASA/CR-2002-211773, at http://techreports.larc.nasa.gov/ltrs/PDF/2002/cr/NASA-2002-cr211773.pdf

Arenberg, D. L. (1948) "Ultrasonic solid delay lines", *J. Acoust. Soc. Am.* <u>20</u>, 1, 1-26.

Alers, G. A. and Zimmerman, R. M. (1980) "Ultrasonic characterization of the thermal protection tiles for the Space Shuttle", *Ultrasonics Symposium*, pp. 894-897.

Banerjee, S., Mal, A.K., Prosser, W.H. (2004). "Analysis of Transient Lamb Waves Generated by Dynamic Surface Sources in Thin Composite Plates", *J. Acoust. Soc. Am.* <u>115</u>, 1905-1911.

Barfuss, H. and Brinkmeyer, E. (1989) "Modified optical frequency domain reflectometry with high spatial resolution for components of integrated systems", *J. Lightwave Technology* 7, 1, 3-10.

Batten, A., Dunlop, J. B., Edwards, G. C., Farmer, A. J., Gaffney, B., Hedley, M., Hoschke, N., Isaacs, P., Johnson, M. E., Lewis, C. J., Murdoch, A., Poulton, G. T., Price, D. C., Prokopenko, M., Sharp, I., Scott, D. A., Valencia, P., Wang, P., Whitnall D. F. (2004) "Development and Evaluation of Sensor Concepts for Ageless Aerospace Vehicles. Report 5: Phase 2 Implementation of the Concept Demonstrator", CSIRO Telecommunications and Industrial Physics. Report No. TIPP 2056. April 2004.

Batten, A., Edwards, G.C., Gerasimov, V., Hoschke, N., Isaacs, P., Lewis, C.J., Moore, R., Oppolzer, F., Price, D.C., Prokopenko, M., Scott, D.A., Wang, P. (2006) "Development and Evaluation of Sensor Concepts for Ageless Aerospace Vehicles. Report 6: Development and Demonstration of a Self-organizing Diagnostic System for Structural Health Monitoring", CSIRO Industrial Physics. Report No. CIP 2544.

Cameron, A. and Durrant-Whyte, H. (1990) "A Bayesian Approach to Optimal Sensor Placement", *Int. J. Robot. Res.* 9, 70-88.

Cheeke, J. D. N. (2002) *Fundamentals and Applications of Ultrasonic Waves*, CRC Press, Boca Raton, FL.

Cheng, J.-C. and Berthelot, Y. H. (1996) "Theory of laser-generated transient Lamb waves in orthotropic plates", *J. Phys. D: Appl. Phys.* 29, 1857-1867.

Childers, B. A., Brown, T. L., Moore, J. P. and Wood, K. H. (2001) "Recent developments in the application of optical frequency domain reflectometry to distributed Bragg grating sensing", in *Fiber Optic Sensor Technology and Applications 2001, Proc. SPIE v4578*, edited by M. A. Marcus and B. Culshaw, SPIE, Bellingham WA.

Dorigo M. and Di Caro G. (1999). "Ant Colony Optimization: A New Meta-Heuristic", *Proc. 1999 Congress on Evolutionary Computation*, Washington DC, USA. pp. 1470-7.

Dorigo, M. and Stützle, T. (2004) *Ant Colony Optimization*, (MIT Press, Cambridge, MA, USA).

Froggatt, M. (1996) "Distributed measurement of the complex modulation of a photoinduced Bragg grating in an optical fiber", *Applied Optics* 35, 25, 5162-5164.

Froggatt, M. and Moore, J. (1998a) "High-spatial-resolution distributed strain measurement in optical fiber with Rayleigh scatter", *Applied Optics* 37, 10, 1735-1740.

Froggatt, M. and Moore, J. (1998a) "Distributed measurement of static strain in an optical fiber with multiple Bragg gratings at nominally equal wavelengths", *Applied Optics* 37, 10, 1741-1746.

Gao, J., Yang, J., Cui, L.-J., Cheng, J.-C., Qian, M.-L. (2006). "Modeling Laser-Generated Guided Waves in Bonded Plates by the Finite Element Method", *Ultrasonics* 44, e985-e989.

Glombitza, U. and Brinkmeyer, E. (1993) "Coherent frequency-domain reflectometry for characterization of single-mode integrated-optical waveguides", *J. Lightwave Technology* 11, 8, 1377-1384.

Goldstein, H. (1950) *Classical Mechanics,* Addison-Wesley (Reading, MA, USA).

Guestrin, C., Krause, A. and Singh, A. P. (2005) "Near-Optimal Sensor Placements in Gaussian Processes", in *Proceedings of the 22nd International Conference on Machine Learning*, Bonn, Germany.

Hoschke, N., Lewis, C.J., Price, D.C., Scott, D.A., Gerasimov, V., Wang, P. (2007) "A Self-organizing Sensing System for Structural Health Monitoring of Aerospace Vehicles". in *Self-Organization: Applied Multi-Agent Systems* edited by M. Prokopenko (Springer-Verlag, Berlin) pp. 51-75.

Jen, C.-K., Ono, Y. and Kobayashi, M. (2006) "High temperature integrated ultrasonic shear wave probes", *Appl. Phys. Lett.* 89, 183506-1 - 183506-3.

Kinsler, L. E., Frey, A. R., Coppens, A. B and Sanders, J. V. (2000) *Fundamentals of Acoustics*, 4th edition, (John Wiley and Sons, New York, NY, USA).

Klyubin, A. S., Polani, D. and Nehaniv, C. L. (2004) "Organization of the Information Flow in the Perception-Action Loop of Evolved Agents" in *2004 NASA/DoD Conference on Evolvable Hardware*, Seattle, WA (IEEE Computer Society), pp. 177-80.

Kuhr, S. J., Reibel, L., Sathish, S. and Jata, K. V. (2006) "Acoustic characterization and impact sensing for ceramic thermal protection systems (TPS)", *Review of Progress in QNDE*, edited by D. O. Thompson and D. E. Chimenti, 25, 1748-1755.

Lee, B. C. and Staszewski, W. J. (2007) "Sensor location studies for damage detection with Lamb waves", *Smart Mater. Struct.* 16, 399-408.

Levy, M. (2001) "Introduction to fundamentals of elastic constants", in *Handbook of Elastic Properties of Solids, Liquids, and Gases, Volume 2*, edited by M. Levy and L. Furr (Academic Press, San Diego, CA, USA).

Mason, W. P. (1958) *Physical Acoustics and the Properties of Solids* (D. van Nostrand Company, Princeton, NJ, USA).

Meirovitch, L. (1967) *Analytical Methods in Vibrations* (Macmillan, New York, NY, USA).

Miller, J. F., Job, D. and Vassilev, V. K. (2000) "Principles in the Evolutionary Design of Digital Circuits – Part I", *Journal of Genetic Programming and Evolvable Machines* 1, 7-35.

NASA Ames information sheet (2007) "Thermal Protection Materials Development":
http://128.102.216.35/factsheets/view.php?id=78/

NASA Dryden (2006) Patent Application DRC 006 "Method for reducing the refresh rate of fiber Bragg grating sensors", NASA Dryden Flight Research Center, Edwards Air Force Base, CA, USA.

Nehaniv, C. L., Polani, D., Olsson, L. and Klyubin, A. S. (2005) "Evolutionary Information-Theoretic Foundations of Sensory Ecology: Channels of Organism-Specific Meaningful Information", *University of Hertfordshire Computer Science Technical Report* 430, August 2005.

Ogilvy, J.A. (1995). "A Model for the Ultrasonic Inspection of Composite Plates", *Ultrasonics* 33, 85-93.

Olsson, L., Nehaniv, C. L. and Polani, D. (2004) "Information Trade-Offs and the Evolution of Sensory Layouts", in *Proceedings of the 9th International Conference on Artificial Life (ALife IX)*, Boston, MA, USA.

Pao, Y.-H. and Gajewski, R. R. (1977) "The Generalized Ray Theory and Transient Responses of Layered Elastic Solids", in *Physical Acoustics* edited by W. P. Mason and R. N. Thurston, Vol XIII (Academic Press, New York, NY, USA), pp. 183-265.

Papadakis, E. P. (1990) "The measurement of ultrasonic attenuation", in *Ultrasonic Measurement Methods* edited by R. N. Thurston and A. D. Pierce, *Physical Acoustics, vol. XIX* (Academic Press, San Diego, CA, USA).

Papadakis, E. P. and Bernstein, H. (1963) "Elastic moduli of pyrolytic graphite", *J. Acoust. Soc. Am.* 35, 4, 521-524.

Pavlakovic, B., Lowe, M.J.S., Alleyne, D.N. and Cawley, P. (1997) "Disperse: a general purpose program for creating dispersion curves", *Review of Progress in QNDE*, edited by D. O. Thompson and D. E. Chimenti, 16, 185-192 (Plenum Press, New York, NY, USA). See also: http://www.imperial.ac.uk/ndt/public/productservice/disperse.htm

Pouet, B. F. and Rasolofosaon, N. J. P. (1993) "Measurement of broadband intrinsic ultrasonic attenuation and dispersion in solids with laser techniques", *J. Acoust. Soc. Am.* 93, 3, 1286-1292.

Price, D.C., Martin, B.J., Scott, D.A. (1999). "Ultrasonic Guided Waves for Inspection of Bonded Panels", *Acoustics Australia* 27, 95-101.

Prokopenko, M., Wang, P., Foreman, M., Valencia, P., Price, D.C., Poulton, G.T. (2005) "On Connectivity of Reconfigurable Impact Networks in Ageless Aerospace Vehicles", *Robotics and Autonomous Systems* 53, 36-58.

Prokopenko, M., Gerasimov, V. and Tanev, I. (2006) "Evolving spatiotemporal coordination in a modular robotic system", in *From Animals to Animats: Proceedings of*

the 9th International Conference on the Simulation of Adaptive Behaviour (SAB 2006) Rome, Italy, edited by S. Nolfi, G. Baldassarre, R. Calabretta, J. C. T. Hallam, D. Marocco, J.-A. Meyer, O. Miglino and D. Parisi. Lecture Notes in Computer Science 4095, 558-69.

Prosser, W.H., Hamstad, M.A., Gary, J., O'Gallagher, A. (1999). "Finite Element and Plate Theory Modeling of Acoustic Emission Waveforms", *J. Nondestr. Eval.* 18, 83-90.

Prosser, W.H., Allison, S.G., Woodard, S.E., Wincheski, R.A., Cooper, E.G., Price, D.C., Hedley, M., Prokopenko, M., Scott, D.A., Tessler, A., Spangler, J.L. (2004). "Structural Health Management for Future Aerospace Vehicles", *Proceedings of the 2nd Australasian Workshop on Structural Health Monitoring*, Melbourne, Australia, December 2004. (ISBN 0-9756992-0-2).

Scott, D. A. and Price, D. C. (2003) "Experimental observation of linear and non-linear guided wave propagation in rolled aluminium sheet", in *Review of Progress in QNDE*, edited by D. O. Thompson and D. E. Chimenti, 22, 1559-1566.

Staszewski, W. J., Worden, K., Wardle, R. and Tomlinson, G. R. (2000). "Fail-safe sensor distributions for impact detection in composite materials", *Smart Mater. Struct.* 9, 298-303.

Thompson, R. B. and Alers, G. A. (1974) "Ultrasonic inspection of low impedance, high loss materials", *Ultrasonics Symposium*, pp. 621-624.

Trendafilova, I., Heylen, W. and Van Brussel, H. (2001) Measurement point selection in damage detection using the mutual information concept", *Smart Mater. Struct.* 10, 528-33.

Visscher, W.M., Migliori, A., Bell, T.M., Reinert, R.A. (1991). "On the Normal Modes of Free Vibration of Inhomogeneous and Anisotropic Elastic Objects", *J. Acoust. Soc. Am.* 90, 2154-2162.

Wei, P.and Sun, X. (2006). A Novel FBG Sensor Network with High Survivability, *Proc. SPIE, 6387*, pp. 63870B-1-9.

Wei, P.and Sun, X. (2007). Smart Sensor Networks is Enhanced by New Models. SPEI Newsroom. http://spie.org/x15064.xml

Appendix A

Calculation of transit times through ceramic foam and along aluminium sheet.

Approximate the geometry of the ceramic foam and tile as shown in Figure A1. An impact occurs on the surface of the ceramic foam at co-ordinates *(x, d)*. A longitudinal wave travels at a speed v_f in a direction such that it impinges on the aluminium sheet at the angle θ as shown, at a point *(x', 0)*. The wave then travels at speed v_a along the aluminium sheet to the transducer at *(0,0)*.
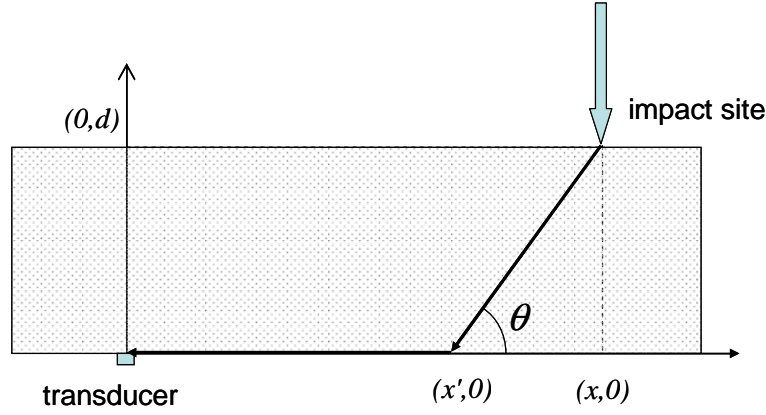

Figure A1. Approximate geometry of waves travelling through ceramic foam and along aluminium sheet.

The time taken to travel along any of these paths is given by

$$t = \frac{x'}{v_a} + \frac{l}{v_f},$$

where *l* is the distance between *(x, d)* and *(x', 0)*. Clearly

$$l = \frac{x - x'}{\cos \theta} \quad \text{and} \quad l = \frac{d}{\sin \theta},$$

$$\therefore \quad x' = x - l \cos \theta = x - \frac{d \cos \theta}{\sin \theta}.$$

So,

$$t = \frac{x}{v_a} - \frac{d}{v_a} \frac{1}{\tan \theta} + \frac{d}{v_f \sin \theta}$$

$$\therefore \quad \frac{\partial t}{\partial \theta} = \frac{-d}{v_a} \frac{\partial}{\partial \theta} \frac{1}{\tan \theta} + \frac{d}{v_f} \frac{\partial}{\partial \theta} \frac{1}{\sin \theta}.$$

For a minimum transit time

$$\frac{\partial t}{\partial \theta} = 0.$$

Therefore

$$\frac{d}{v_a}\left(1+\frac{\cos^2\theta}{\sin^2\theta}\right) - \frac{d}{v_f}\frac{\cos\theta}{\sin^2\theta} = 0.$$

Multiply throughout by $v_a v_f \sin^2\theta$ and simplify to give

$$\cos\theta = \frac{v_f}{v_a}.$$

Therefore the fastest route for the sound to take is that for which the angle at which the sound impinges on the aluminium sheet is given by $\cos^{-1} v_f / v_a$, which for the present materials is about 58.8°, giving x-x' =16.3 mm if the foam thickness is 27 mm. For x greater than 16.3 mm the minimum transit time is approximately

$$t_{\min} = \frac{x-16.3}{5.4} + \frac{31.58}{2.9},$$

using 2.9 mm/µs for the wave speed in the foam, 5.4 mm/µs for the wave speed in aluminium, and 27 mm as the thickness of the foam. The values at 20, 30, 40 and 50 mm are indicated by the arrows in Figure 3.17 (left). If x is less than 16.3 mm, then the fastest route is through the foam along a line joining the impact site with the transducer's position. For values of lateral displacement of 0 mm and 10 mm the arrows in Figure 3.17 (left) indicate these direct-path transit times.

Appendix B:

Project reports and publications

This appendix lists the research output of the project group and collaborators since the beginning of the work in November 2001.

1. *Development and Evaluation of Sensor Concepts for Ageless Aerospace Vehicles, Report 1*
    D. Abbott, S. Cunningham, G. Daniels, B. Doyle, J. Dunlop, D. Economou, A. Farmer, D. Farrant, C. Foley, B. Fox, M. Hedley, J. Herrmann, C. Jacka, G. James, M. Johnson, B. Martin, G. Poulton, D. Price, T. Reda, G. Rosolen, A. Scott, P. Valencia, D. Ward, J. Winter, A. Young
    CSIRO Telecommunications and Industrial Physics. Report No.
    TIPP 1516, 2001. Also published as NASA Technical Report no. NASA/CR-2002-211772, at http://techreports.larc.nasa.gov/ltrs/PDF/2002/cr/NASA-2002-cr211772.pdf

2. *Development and Evaluation of Sensor Concepts for Ageless Aerospace Vehicles. Development of Concepts for an Intelligent Sensing System. Report 2*
    D. Abbott, B. Doyle, J. Dunlop, A. Farmer, M. Hedley, J. Herrmann, G. James, M. Johnson, B. Joshi, G. Poulton, D. Price, M. Prokopenko, T. Reda, D. Rees, A. Scott, P. Valencia, D. Ward, J. Winter
    CSIRO Telecommunications and Industrial Physics. Report No.
    TIPP 1517. May 2002. Also published as NASA technical report NASA/CR-2002-211773, at http://techreports.larc.nasa.gov/ltrs/PDF/2002/cr/NASA-2002-cr211773.pdf

3. *Concepts for an Integrated Vehicle Health Monitoring System*
    D. Abbott, B. Doyle, J.B. Dunlop, A.J. Farmer, M. Hedley, J. Herrmann, G.C. James, M.E. Johnson, B. Joshi, G.T. Poulton, D.C. Price, M. Prokopenko, T. Reda, D.E. Rees, D.A. Scott, P. Valencia, D. Ward and J.G. Winter
    Review of Progress in Quantitative Nondestructive Evaluation, Vol. 22, pp.1606-14 (eds. D.O. Thompson and D.E. Chimenti), American Institute of Physics Conference Proceedings Vol. 657, (2003).

4. *Experimental Observation of Linear and Non-Linear Guided Wave Propagation in Rolled Aluminum Sheets*
    D.A. Scott and D.C. Price
    Review of Progress in Quantitative Nondestructive Evaluation, Vol. 22, pp.1559-66 (eds. D.O. Thompson and D.E. Chimenti), American Institute of Physics Conference Proceedings Vol. 657, (2003).

5. *Theoretical Aspects of Linear and Non-Linear Guided Wave Propagation in Rolled Aluminum Sheets*
    D.C. Price and D.A. Scott
    Review of Progress in Quantitative Nondestructive Evaluation, Vol. 22, pp.1567-

74 (eds. D.O. Thompson and D.E. Chimenti), American Institute of Physics Conference Proceedings Vol. 657, (2003).

6. *Development and Evaluation of Sensor Concepts for Ageless Aerospace Vehicles. Report 3: Design of the Concept Demonstrator*
D. Abbott, J. Ables, A. Batten, D. C. Carpenter, A. F. Collings, B. Doyle, J. B. Dunlop, G. C. Edwards, A. J. Farmer, B. Gaffney, M. Hedley, P. Isaacs, M. E. Johnson, B. Joshi, C. J. Lewis, G. T. Poulton, D. C. Price, M. Prokopenko, T. Reda, D. E. Rees, D. A. Scott, S. Seneviratne, P. Valencia, P. Wang, D. F. Whitnall, J. Winter
CSIRO Telecommunications and Industrial Physics. Report No.
TIPP 1628. January 2003.

7. *Smart Sensor Network for Space Vehicle Monitoring*
M. Hedley, M.E. Johnson, C.J. Lewis, D.A. Carpenter, H. Lovatt, D.C. Price
Proceedings of the International Signal Processing Conference (Dallas, Tx.), March 2003.

8. *Self-reconfigurable Sensor Networks in Ageless Aerospace Vehicles*
P. Wang, P. Valencia, M. Prokopenko, D.C. Price, G.T. Poulton
Proceedings of the 11th International Conference on Advanced Robotics (ICAR-03), Portugal, July 2003, pp.1098-1103.

9. *Self-organizing Impact Boundaries in Ageless Aerospace Vehicles*
H. Lovatt, G.T. Poulton, D.C. Price, M. Prokopenko, P. Valencia, P. Wang
Proceedings of the 2nd International Conference on Autonomous Agents and Multi-Agent Systems (AAMAS-2003), Melbourne, July 2003, pp.249-56 (ACM Press, NY).

10. *Phase Transitions in Self-organising Sensor Networks*
M. Foreman, M. Prokopenko, P. Wang
Proceedings of the 7th European Conference on Artificial Life (ECAL-03), pp. 781-791. Dortmund, Germany, September 2003.

11. *An Integrated Health Monitoring System for an Ageless Aerospace Vehicle*
D.C. Price, D.A. Scott, G.C. Edwards, A. Batten, A.J. Farmer, M. Hedley, M.E. Johnson, C.J. Lewis, G.T. Poulton, M. Prokopenko, P. Valencia, P. Wang
In "Structural Health Monitoring 2003", Proceedings of the 4th International Workshop on Structural Health Monitoring, Stanford, CA, September 2003 (ed. F-K. Chang) DEStech Publications, 2003, pp.310-18. (ISBN: 1-932078-20-7).

12. *Development and Evaluation of Sensor Concepts for Ageless Aerospace Vehicles. Report 4: Phase 1 Implementation of the Concept Demonstrator*
D. Abbott, A. Batten, D. C. Carpenter, J. B. Dunlop, G. C. Edwards, A. J. Farmer, B. Gaffney, M. Hedley, N. Hoschke, P. Isaacs, M. E. Johnson, C. J. Lewis, A. Murdoch, G. T. Poulton, D. C. Price, M. Prokopenko, D. E. Rees, D. A. Scott, S. Seneviratne, P. Valencia, P. Wang, D. F. Whitnall
CSIRO Telecommunications and Industrial Physics. Report No.
TIPP 1898. Sept. 2003.

13. *Evolvable Recovery Membranes in Self-Monitoring Aerospace Vehicles*
    P. Wang, M. Prokopenko
    In Proceedings of the 8th International Conference on Simulation of Adaptive
    Behaviour (SAB-2004), Los Angeles, USA, July 2004, pp.509-18.

14. *On Connectivity of Reconfigurable Impact Networks in Ageless Aerospace
    Vehicles*
    Mikhail Prokopenko, Peter Wang, Mark Foreman, Philip Valencia, Don Price,
    Geoff Poulton
    Robotics and Autonomous Systems 53, 36-58 (2005).

15. *Self-organizing Hierarchies in Sensor and Communication Networks*
    Mikhail Prokopenko, Peter Wang, Don Price, Philip Valencia, Mark Foreman,
    Anthony Farmer
    Artificial Life (Special Issue on Dynamic Hierarchies) 11, 407-26 (2005).

16. *On Self-referential Shape Replication in Robust Aerospace Vehicles*
    M. Prokopenko, P. Wang
    Proceedings of the 9th International Conference on the Simulation and Synthesis
    of Living Systems (ALIFE9), Boston, USA, September 2004, pp.27-32.

17. *Testbed for Structural Health Monitoring Network*
    M. Hedley, M. E. Johnson, C. J. Lewis, D. C. Price
    Proc. Global Signal Processing Conference, Santa Clara, California, USA, Sept.
    2004. ICT Centre Publication 04/1856.

18. *Communication Protocols for a Structural Health Monitoring Network*
    M. Hedley
    Proc. IEEE Conf. on Mobile Ad-hoc and Sensor Systems (MASS-2004), Fort
    Lauderdale, Florida, USA, October 2004.

19. *Development and Evaluation of Sensor Concepts for Ageless Aerospace Vehicles.
    Report 5: Phase 2 Implementation of the Concept Demonstrator*
    A. Batten, J. B. Dunlop, G. C. Edwards, A. J. Farmer, B. Gaffney, M. Hedley, N.
    Hoschke, P. Isaacs, M. E. Johnson, C. J. Lewis, A. Murdoch, G. T. Poulton, D. C.
    Price, M. Prokopenko, I. Sharp, D. A. Scott, P. Valencia, P. Wang, D. F. Whitnall
    CSIRO Telecommunications and Industrial Physics. Report No.
    TIPP 2056. April 2004.

20. *Intelligent Health Monitoring for Aerospace Vehicles. Report 1. Stage 1: Project
    Scope and Feasibility Demonstration*
    I.S. Cole, D.C. Price, T. Muster, M. Hedley, R. Drogemuller, G. Trinidad, S.
    Egan, F. Boulaire, M. Prokopenko
    CMIT, CTIP, CICT Centre Report to the Boeing Company. Report
    No. CMIT-2004-157, April 2004.

21. *An Intelligent Sensor System for Detection and Evaluation of Particle Impact Damage*
D.A. Scott, A. Batten, G.C. Edwards, A.J. Farmer, M. Hedley, N. Hoschke, P. Isaacs, M. Johnson, A. Murdoch, C. Lewis, D.C. Price, M. Prokopenko, P. Valencia, P. Wang
Review of Progress in Quantitative Nondestructive Evaluation, Vol. 24, pp.1825-32 (eds. D.O. Thompson and D.E. Chimenti), American Institute of Physics Conference Proceedings Vol. 760, (2005).

22. *Sensor Network for Structural Health Monitoring*
M. Hedley, N. Hoschke, M. Johnson, C. Lewis, A. Murdoch, D. Price, M. Prokopenko, A. Scott, P. Wang, A. Farmer
Proceedings of the 2004 Intelligent Sensors, Sensor Networks and Information Processing Conference (December 2004), pp.361-6 (2004). (ISBN: 0-7803-8894-1).

23. *Structural Health Management for Future Aerospace Vehicles*
W.H. Prosser, S.G. Allison, S.E. Woodard, R.A. Wincheski, E.G. Cooper, D.C. Price, M. Hedley, M. Prokopenko, D.A. Scott, A. Tessler, J.L. Spangler
Proceedings of the 2nd Australasian Workshop on Structural Health Monitoring (2AWSHM), Melbourne, Aust., December 2004 (ISBN 0-9756992-0-2).

24. *Detection, Evaluation and Diagnosis of Impact Damage in a Complex Multi-Agent Structural Health Management System*
D.C. Price, A. Batten, G.C. Edwards, A.J.D. Farmer, V. Gerasimov, M. Hedley, N. Hoschke, M.E. Johnson, C.J. Lewis, A. Murdoch, M. Prokopenko, D.A. Scott, P. Valencia, P. Wang
Proceedings of the 2nd Australasian Workshop on Structural Health Monitoring (2AWSHM), Melbourne, Aust., December 2004 (ISBN 0-9756992-0-2).

25. *Intelligent Health Monitoring for Aerospace Vehicles. Stage 2A Report*
I.S. Cole, P. Corrigan, D.C. Price, T. Muster, W. Ganther, M. Hedley, R. Drogemuller, D. Paterson, S. Egan, F. Boulaire
CMIT, CIP Report to the Boeing Company. Report No. CMIT-2004-523, December 2004. (75 pages).

26. *Development of a System for Corrosion Diagnostics and Prognostics*
Angela Trego, Don Price, Mark Hedley, Penny Corrigan, Ivan Cole, Tim Muster
Proceedings of 1st World Congress on Corrosion in the Military: Cost Reduction Strategies. (Sorrento, Italy, 6-8 June 2005).

27. *Complexity Metrics for Self-monitoring Impact Sensing Networks*
M. Prokopenko, P. Wang, D. Price
Proceedings of the 2005 NASA/DoD Conference on Evolvable Hardware, pp. 239-246. (July 2005) (ISBN: 0-7695-2399-4).

28. *On Convergence of Dynamic Cluster Formation in Multi-Agent Networks*
M. Prokopenko, P. Mahendra, P. Wang

Proceedings of the 8th European Conference on Artificial Life (ECAL-2005) (Canterbury, UK) Sept. 2005.

29. *On Decentralised Clustering in Self-monitoring Networks*
Piraveenan Mahendra rajah, Mikhail Prokopenko, Peter Wang, Don Price
Proceedings of the Fourth International Joint Conference on Autonomous Agents and Multiagent Systems, pp. 1175-6 (2005) (ACM Press, N.Y.) (ISBN: 1-59593-093-0).

30. *Towards Adaptive Clustering in Self-monitoring Multi-agent Networks*
Piraveenan Mahendra rajah, Mikhail Prokopenko, Peter Wang, Don Price
Proceedings of the 9th International Conference on Knowledge Based and Intelligent Information and Engineering Systems (KES-2005) (Melbourne, Aust., Sept. 2005).

31. *On Self-organising Diagnostics in Impact Sensing Networks*
M. Prokopenko, P. Wang, D.A. Scott, V. Gerasimov, N. Hoschke, D.C. Price
Proceedings of the 9th International Conference on Knowledge Based and Intelligent Information and Engineering Systems (KES-2005) (Melbourne, Aust., Sept. 2005).

32. *Establishing a Physical Basis for the In-situ Monitoring of Airframe Corrosion using Intelligent Sensor Networks*
T. Muster, I. Cole, W. Ganther, D. Paterson, P. Corrigan, D. Price
Proceedings of the 2005 Tri-Service Corrosion Conference (Florida, USA, November 2005).

33. *Intelligent Health Monitoring for Aerospace Vehicles. Stage 2B Report*
I.S. Cole, F. Boulaire, P. Corrigan, R. Drogemuller, S. Egan, W. Ganther, T. Muster, D. Paterson, D.C. Price, M. Hedley, B. Hinton, S. Galea
CMIT, CIP, DSTO Report to the Boeing Company. Report No. CMIT-2005-520, December 2005. (137 pages).

34. *Self-Organising Impact Sensing Networks in Robust Aerospace Vehicles*
Mikhail Prokopenko, Geoff Poulton, Don Price, Peter Wang, Philip Valencia, Nigel Hoschke, Tony Farmer, Mark Hedley, Chris Lewis, Andrew Scott
In "Advances in Applied Artificial Intelligence", ed. John Fulcher (Idea Group, Hershey, PA, USA, 2006) pp.186-233.

35. *A Self-Organising Sensing System for Structural Health Management*
N. Hoschke, C.J. Lewis, D.C. Price, D.A. Scott, G.C. Edwards, A. Batten
Proceedings of the 10th International Conference on Knowledge-Based and Intelligent Information and Engineering Systems (KES-2006) (Bournemouth, UK, Oct. 2006).

36. *Development and Evaluation of Sensor Concepts for Ageless Aerospace Vehicles, Report 6. Development and Demonstration of a Self-Organizing Diagnostic System for Structural Health Monitoring*
A. Batten, G. Edwards, V. Gerasimov, N. Hoschke, P. Isaacs, C. Lewis, R.

Moore, F. Oppolzer, D. Price, M. Prokopenko, A. Scott and P. Wang
CSIRO Industrial Physics. Report No. CIP 2544, October 2006.

37. *A Self-organizing Sensing System for Structural Health Monitoring of Aerospace Vehicles*
N. Hoschke, C. J. Lewis, D. C. Price, D. A. Scott, V. Gerasimov and P. Wang, in 'Advances in Applied Self-Organizing Systems', Ed. M. Prokopenko, (Springer-Verlag, London, UK, 2007) pp. 51-75.

1. REPORT DATE *(DD-MM-YYYY)*	2. REPORT TYPE	3. DATES COVERED *(From - To)*
01-12-2007	Contractor Report	

4. TITLE AND SUBTITLE	5a. CONTRACT NUMBER
Health Monitoring of Thermal Protection Systems - Preliminary Measurements and Design Specifications	
	5b. GRANT NUMBER
	5c. PROGRAM ELEMENT NUMBER

6. AUTHOR(S)	5d. PROJECT NUMBER
Scott, D. A.; and Price, D. C.	NNL07AA04P
	5e. TASK NUMBER
	5f. WORK UNIT NUMBER
	939904.05.07

7. PERFORMING ORGANIZATION NAME(S) AND ADDRESS(ES)	8. PERFORMING ORGANIZATION REPORT NUMBER
NASA Langley Research Center Hampton, VA 23681-2199	CIP 2687

9. SPONSORING/MONITORING AGENCY NAME(S) AND ADDRESS(ES)	10. SPONSOR/MONITOR'S ACRONYM(S)
National Aeronautics and Space Administration Washington, DC 20546-0001	NASA
	11. SPONSOR/MONITOR'S REPORT NUMBER(S)
	NASA/CR-2007-215092

12. DISTRIBUTION/AVAILABILITY STATEMENT
Unclassified - Unlimited
Subject Category 38
Availability: NASA CASI (301) 621-0390

13. SUPPLEMENTARY NOTES
Report 1
Langley Technical Monitor: Edward R. Generazio
An electronic version can be found at http://ntrs.nasa.gov

14. ABSTRACT

The work reported here is the first stage of a project that aims to develop a health monitoring system for Thermal Protection Systems (TPS) that enables a vehicle to safely re-enter the Earth's atmosphere. The TPS health monitoring system is to be integrated into an existing acoustic emissions-based Concept Demonstrator, developed by CSIRO, which has been previously demonstrated for evaluating impact damage of aerospace systems.

15. SUBJECT TERMS
Health Monitoring; NDE; NDI; NDT; Nondestructive; Thermal Protection System

16. SECURITY CLASSIFICATION OF:			17. LIMITATION OF ABSTRACT	18. NUMBER OF PAGES	19a. NAME OF RESPONSIBLE PERSON
a. REPORT	b. ABSTRACT	c. THIS PAGE			STI Help Desk (email: help@sti.nasa.gov)
					19b. TELEPHONE NUMBER *(Include area code)*
U	U	U	UU	91	(301) 621-0390